

Enhancing the Dispatchability of Wind Energy Using Inertial Storage and Hybrid Systems

Final Report

Submitted by
Department of Electrical Engineering
University of Minnesota
December, 2006

Project Report Summary

The goal of the project was to investigate the use of inertial storage as a means of making wind generation dispatchable. Due to the fluctuation of wind power, a wind system currently generates a constantly varying output power. If the wind system were to be made dispatchable, it would be able to produce a constant output power for a set period of time. Preferably this period of time would be for an entire day, similar to other types of generation. Inertial storage is not able to provide this capability by itself, so a hybrid wind system is also considered. This hybrid wind system consists of wind generation, inertial storage, and moderately fast response fuel-based generation, such as gas turbines.

The inertial storage in this project is a flywheel battery. A flywheel battery stores energy in the form of a rotating wheel. The rotating wheel in modern flywheels is typically made from high strength to weight ratio materials, such as carbon fiber. To decrease the idle loss (or self-discharge) of the flywheel battery magnetic bearings are utilized. Since the outer rim of the flywheel rotates at a high velocity, the flywheel's enclosure maintains a vacuum or is filled with a gas, such as hydrogen, to reduce windage loss and further decrease idle loss. For a 100 kWh flywheel the enclosure is about 65 inches in diameter and 84 inches in height.

To transfer energy in and out of the rotating wheel a motor/generator is necessary. This machine acts as a motor when the flywheel battery is charged, and as a generator when it is discharged. The motor/generator is coupled to the utility through power electronics that allow its speed to be variable.

The low windage loss conditions inside the enclosure are a problem for the motor/generator. This type of environment only allows for minimal heat transfer from the motor/generator's rotor. While it is possible to use a coupling system to locate the motor/generator externally to the enclosure, this results in a substantial increase in complexity and cost. Therefore, the design of a motor/generator with low rotor loss and high temperature capability is an enabling technology for flywheel batteries. The design of such a machine is the main focus of this project.

The synchronous reluctance machine was investigated in this project as a possible solution for the motor/generator. This machine technology is of special interest since it has substantially lower rotor loss than other machine technologies such as induction or switched reluctance machines. The rotor of the machine is composed of only steel allowing for a much higher rotor operating temperature than other technologies such as permanent magnet machines. Additional advantages over permanent magnet machines include low rotational loss (results in low idle loss), low cost, and greater ruggedness (due to lack of permanent magnets).

The first synchronous reluctance rotor investigated in this project was an axially laminated rotor. This rotor was initially attractive due to its potential for very high performance. However, results of small-scale fabrication and testing showed that there are numerous problems and limitations with the fabrication of this rotor. In addition, further simulations showed that for a full-scale machine the fabrication limitations result in excessive rotor loss.

Due to the information gained from investigating the axially laminated rotor, a conventionally laminated rotor was designed and analyzed. This type of rotor results in a machine with suitable performance, and the low rotor loss required in the low windage loss conditions found inside the enclosure. Additionally, this rotor is easier to fabricate and is less costly than the axially

laminated rotor. Thus, a synchronous reluctance machine utilizing a conventionally laminated rotor provides a viable solution for locating the motor/generator inside the enclosure of the flywheel battery.

Besides the investigation and development of the flywheel components, the possible wind and non-wind application of the flywheel battery are also examined. To determine the feasibility of any of these applications, the sizing and economics of the flywheel battery were examined.

The original goal of the project was to determine if through the use of inertial storage a hybrid wind system could be made dispatchable for 24 hour time periods. This is possible if gas turbines and flywheel batteries are combined with wind generation. However, the economics of such a system currently are not good. Due to the current leniency wind system is granted in its generation output, it is difficult to justify the additional cost of the flywheel batteries and gas turbines. The current high cost of fuel for gas turbines also further hurts the economics of this system. Future changes to the way wind generation is handled in a power system may change the situation, but currently the wind hybrid system is not the best application for flywheel batteries.

An alternative to the wind hybrid system is to use the flywheel batteries as an energy buffer or for frequency regulation of a wind system. As an energy buffer the flywheel battery maintains a constant power from the wind farm for short set periods of time (minutes to possibly an hour). This constant power is forecast ahead of time to allow other generation on the power system to make adjustments accordingly. As frequency regulation the flywheel battery handles short-term changes in the output generation of the wind farm while other slower power generation adjusts to the long-term changes. The frequency regulation is currently handled by gas turbines, but it has been found in this project that flywheel batteries are a lower cost solution for frequency regulation.

Flywheel batteries acting as an energy buffer or as frequency regulation are both economically viable applications. Since these functions would normally be provided by gas turbines, both solutions also reduce emissions. Additionally, the flywheel batteries in these applications can supply reactive power, provide voltage support, and improve the stability of the power system. Most importantly, both of these solutions provide a means to significantly increase the percentage of power generated from wind in a power system.

The flywheel battery is also currently a possible solution for other utility applications such as frequency regulation (for load variations in this case), spinning reserve, and peak power buffering. In all three of these applications the flywheel battery is a profitable solution. For both frequency regulation and spinning reserve applications, emissions are also substantially lower due to a reduction in the use of gas turbines. The ability of the flywheel batteries in these applications to also supply reactive power, provide voltage support, and improve dynamic stability will also improve the reliability of the power system.

If in the future, the cost of flywheel energy capacity is reduced, it will enable the use of flywheel batteries to more effectively utilize existing transmission lines. This will result in the ability to deliver more power to customers utilizing existing transmission lines, and prevent the need to install new transmission. For this application to be practical, significant advancements in composite technology, along with a substantial decrease in composite material and fabrication costs, are necessary (indeed a possibility, given the advancements in the nanotechnology). Overall the flywheel battery appears to be a promising solution to numerous utility applications.

Contents

1	Introduction.....	5
2	Flywheel Battery Description	5
3	Composite Wheel.....	6
4	Enclosure.....	7
5	Magnetic Bearings	8
5.1	Flywheel Orientation	8
5.2	Magnetic Bearing Designs.....	8
5.3	Emergency Touchdown Bearings.....	10
6	Motor/Generator Selection.....	10
7	Synchronous Reluctance Machine.....	13
8	Initial Design of Full-scale Motor/Generator	17
9	Small-scale Design and Fabrication.....	20
10	Inverter and Test Setup Design.....	26
10.1	Inverters	26
10.2	FPGA Control and Interface Board	28
10.3	dSPACE Controller.....	30
10.4	Additional Sensors.....	30
10.5	SIMULINK Controller for Test Setup.....	31
11	Test Results.....	33
11.1	Initial Testing	33
11.2	Back-to-back Tests.....	34
11.3	Results of Back-to-back Testing.....	35
11.4	Rotor Loss.....	42
11.5	Conclusions From Test Results	42
12	Iron Loss Simulations	42
13	Thermal Simulations.....	48
14	Redesign of the Full-scale Motor/Generator.....	49
14.1	Base Case Thermal Analysis	51
14.2	Axially Laminated Rotor	55
14.3	Conventionally Laminated Rotor.....	56
14.4	New Motor/Generator Design.....	58

14.5	Conclusion of Four-pole Design.....	62
14.6	Motor/Generator Changes Based on Economic Analysis.....	62
15	Control of the Synchronous Reluctance Machine	63
16	Economics of Possible Flywheel Applications.....	70
16.1	Flywheel Economics for Non-wind Applications.....	70
16.1.1	Spinning Reserve	70
16.1.2	Frequency Regulation	72
16.1.3	Peak Power Buffer	75
16.1.4	Pollution Credit.....	77
16.1.5	Transmission Credit and Load Leveling Credit.....	77
16.2	Flywheel Economics for Non-wind Applications.....	78
16.2.1	Hybrid Wind System: Power and Energy Sizing.....	78
16.2.2	Economics of Hybrid Wind System	84
16.2.3	Energy Buffer for Wind Systems: Power and Energy Sizing.....	85
16.2.4	Economics of Energy Buffer for Wind Systems.....	92
17	Conclusion	93
	References.....	93

Appendix A Agenda of 4 Workshops Organized

Appendix B Description of the Highly Simplified Matrix Converter Control

1 Introduction

The goal of this project was to enhance the dispatchability of wind energy through the use of inertial storage. Due to the fluctuation of wind power, a wind system is currently not able to generate constant power. The goal of an inertial storage system is to level out these fluctuations to produce constant power for set time periods. The ultimate goal is to produce constant power generation for an entire day, as other types of generation are capable of producing. While constant generation for this length of time period is not practical with inertial storage, producing constant generation for smaller time periods is a possibility.

A flywheel battery is an effective method of inertial storage. It stores energy in the form of a rotating wheel. Energy is transferred to and from the wheel through a machine that acts as both a motor and a generator. The power from the motor/generator is transferred through power electronics to the transmission grid. Figure 1-1 is a simple diagram of a flywheel battery for use in a wind system. To increase power or energy storage capability, multiple flywheels can be connected to the grid.

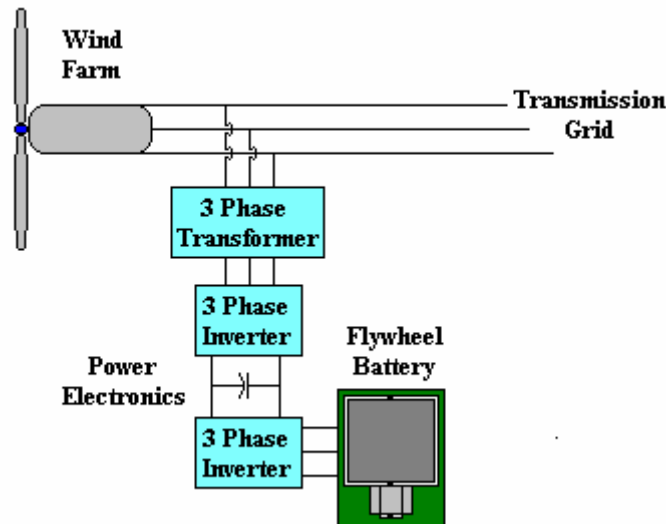


Figure 2-1: Basic Flywheel Battery Components

The flywheel battery designed for wind applications is also applicable to additional non-wind applications. These applications include spinning reserve, frequency regulation, peak power buffers, and energy storage for FACTS devices. For these applications the flywheel batteries are also able to supply reactive power and improve stability. In the future the flywheel may also allow for better utilization of transmission lines, thus preventing the need for installing new transmission.

In flywheel batteries, it is desirable for the motor/generator to operate in an enclosure that either maintains a vacuum or is filled with a low windage loss gas such as hydrogen. In either of these cases, the heat transferred from the rotor is minimal. Therefore, the motor/generator's rotor must have low loss and be capable of withstanding high temperatures. The majority of the work on this project was on design of a motor/generator with these properties.

2 Flywheel Battery Description

Modern flywheel batteries consist of the following components: wheel, enclosure, bearings, motor/generator, power electronics, and controls. Figure 2-1 illustrates the basic flywheel components. The wheel is composed of high strength materials and stores the energy of the flywheel. The enclosure provides protection in case of a wheel failure, and in most flywheel batteries either maintains a vacuum or contains a low windage loss gas. In flywheel batteries, the bearings are important due to the high continuous rotation speed and the large mass of the wheel. The motor/generator transfers power in and out of the flywheel. The power electronics and controls are used to control the motor/generator and magnetic bearings.

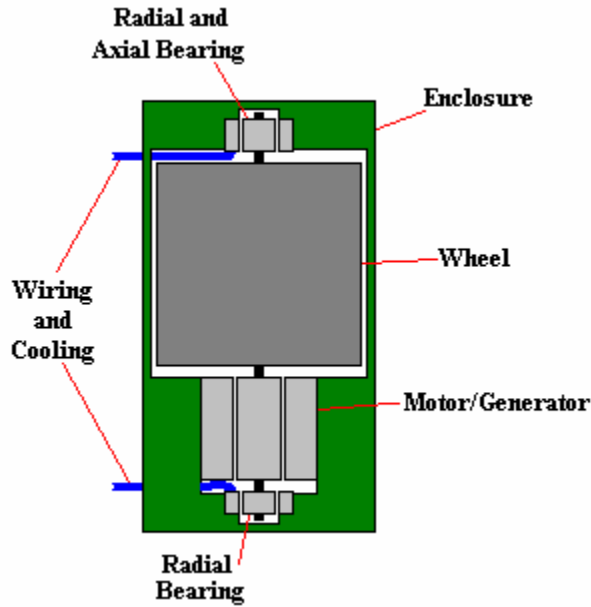


Figure 2-1: Basic Flywheel Battery Components

To decrease the flywheel battery's bearing loss due to the large weight and high rotation speeds, the rotating components are typically levitated by magnetic bearings. To decrease the weight the magnetic bearings have to levitate the wheel is typically composed of composite materials such as carbon fiber.

To decrease the flywheel battery's windage loss, due to the high speed of the outer rim of the wheel, the wheel is located in a vacuum or low windage loss gas. The motor/generator is located in the same enclosure as the wheel or a coupling system needs to be added that allows for the machine to be located outside the enclosure. Locating the motor/generator in the enclosure results in minimal heat transfer from the rotor, but it is advantageous due to the high cost and complexity of a coupling system. The majority of the report deals with the development of a motor/generator that is able to operate in the same enclosure as the wheel.

3 Composite Wheel

The wheel is the energy storage component of the flywheel battery. The energy stored in a basic cylindrical wheel is determined by the relationship

$$E = I\omega^2 \quad (3-1),$$

where inertia is

$$I = \frac{1}{2}mr^2 \quad (3-2),$$

m is mass, r is radius, and ω is the rotation speed. It is common for the wheel to operate between its maximum rotation speed and half of this speed. Due to the squared relationship of rotation speed to energy, this recovers 75% of the wheels energy.

While different wheel shapes have been proposed a basic cylinder made of concentric rings is representative of many of them. The maximum stress on each ring is

$$\sigma_{stress} = \frac{\rho\omega^2}{4(1-\mu)} ((3-2\mu)r_{out}^2 + (1-2\mu)r_{in}^2) \quad (3-3),$$

where r is radius, ρ is density, and μ is Poisson's ratio. For composite fiber rings these equations are oversimplified, but it provides a ballpark result.

Due to the dependence of energy storage on both mass and speed, it is inevitable that high bearing loss will occur. If materials with high strength to weight ratios are used, this loss can be reduced. Composite materials, such as carbon fiber, have the desired properties and result in a lightweight wheel that operate at high rotation speed or have a large radius.

University of Texas, at Austin, has designed a composite wheel for flywheels, which is able to store 100kWhrs with a maximum rotation speed of 15,000 rpm [1]. This wheel is composed of carbon fiber rings that are prestressed over each other. The weight of the wheel and enclosure is 8600 kg and the volume is 3.82 m³ [2] (65 inch diameter and 84 inch height). This wheel is the basis for the initial speed range of the flywheel battery.

4 Enclosure

The wheel for the flywheel battery can be located in air, a vacuum, or a low windage gas, such as hydrogen. For large energy storage wheels the outer surface of the wheel moves at high velocity. The windage loss increases by a cubic with both the radius and rotation speed of the wheel. Thus, if the wheel is located in air, this will result in large windage loss.

If the rotor is instead located in a vacuum, the loss can be decreased to close to zero. This is easily done by creating a vacuum inside the enclosure using a vacuum pump and then tightly sealing the enclosure. A vacuum pump can also be permanently attached to the system allowing for lower performance and less costly seals.

Filling the enclosure with hydrogen is another option. While this increases the windage loss, the loss is much lower than for air. The main reason for considering hydrogen is that it increases the heat transfer from the motor/generator's rotor. For higher performance the pressure of the hydrogen can be decreased to lower windage loss at low motor/generator loads, and increased at high loads to increase the rotor heat transfer.

Besides maintaining a vacuum or containing low windage gas, the enclosure must also safely contain the wheel in the case of a failure. During a failure the enclosure should safely dissipate the stored energy in the wheel without damaging anything external to the flywheel. If a failure is sensed flooding the enclosure with air will dissipate a portion of the stored energy.

The wall of the enclosure still needs to absorb the remaining energy. One of the benefits though of using a carbon fiber wheel is that during a failure it tends to shred into debris, which also uses some of the stored energy. A unique enclosure described in [3] takes this concept and extends it

to the enclosure. In this design the enclosure is made of an outer wall of high strength steel, and an inner layer of carbon fiber. This inner wall is not fixed, but can rotate. This causes more energy dissipation due to the shredding and rotation of the inner wall. This type of enclosure needs less material to absorb the stored energy and thus reduces the cost of the enclosure.

5 Magnetic Bearings

The bearings in a flywheel are usually either mechanical or magnetic. Mechanical bearings are simple and have a low initial cost, but due to the large mass and rotation speed of the flywheel, they have large friction loss. In addition, the large mass and rotation speed shorten the lifetime of the bearings, and they require replacement numerous times during the lifetime of the flywheel battery. The combined costs of bearing replacement and lost energy make the long-term costs of mechanical bearings high. The possible vacuum or hydrogen atmosphere, to reduce windage loss, may also present a problem since mechanical bearings need lubrication, and either environment will complicate this requirement. Therefore, mechanical bearings do not seem suitable for the full-scale flywheel battery.

Magnetic bearings solve the problems associated with mechanical bearings. Since magnetic bearings do not physically touch, they have low loss, do not wear out, and do not require lubrication. Magnetic bearing can produce axial force, radial force, and a combination of both. Bearing setups typically consist of multiple radial force bearings and one axial force bearing.

5.1 Flywheel Orientation

The orientation of the flywheel is chosen based on the force and response needed from the radial and axial bearings. The largest bearing forces need to counteract the gravity acting on the mass of the wheel. If the wheel spins parallel to gravity the radial bearings must produce large forces, while the axial bearing must produce large forces if the wheel spins perpendicular to gravity. The perpendicular orientation is chosen since it is easier to produce and control one large axial bearing force rather than multiple large radial bearing forces. If the radial bearings maximum force is reduced, their response can also be increased to deal with rotor dynamics issues.

While only one axial bearing is needed in flywheel battery, the number of radial bearing will be two or three. One of the radial bearings is located on the side of the wheel the motor/generator is not connected to. For shorter motor/generators a second radial bearing is needed either between the wheel and the motor/generator or on the other side of the motor/generator. For longer motor/generators the extra length of the machine requires the use of a radial bearing both between the motor/generator and the wheel and on the other side of the motor/generator.

5.2 Magnetic Bearing Designs

The two categories of magnetic bearings are passive and active and numerous examples of both types of designs can be found in literature. Passive bearings have no external force control and are composed of permanent magnets. Active magnetic bearings have external control usually in the form of position sensors and power electronics. Current induces the magnetic fields in active bearings, but permanent magnets can be included to reduce loss.

A passive axial magnetic bearing design in [4] uses permanent magnets in a Halbach configuration as in Figure 5-1. The Halbach configuration produces greater force in a smaller

volume. This passive bearing example is representative of the majority of passive bearings. While this system requires no external power source to maintain its operation and thus has very low loss, the cost of this type of bearing is very high for the size forces needed in the full-scale flywheel.

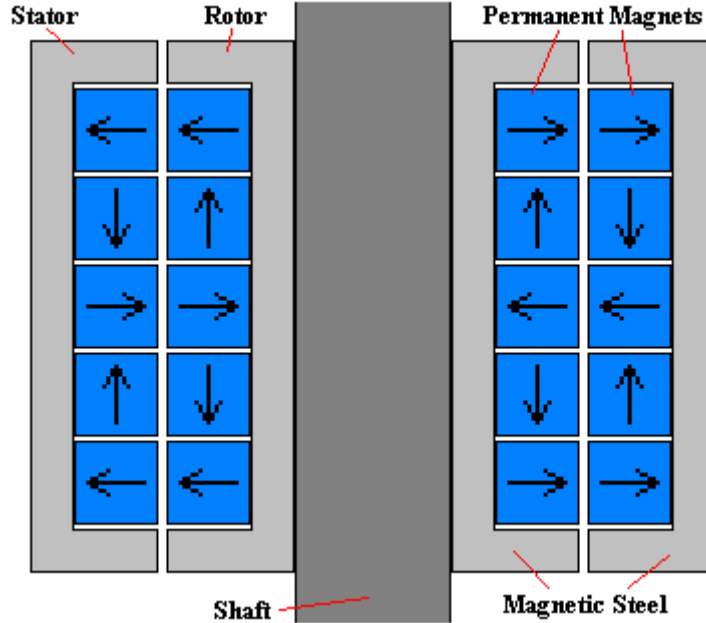


Figure 5-1: Halbach Passive Axial Magnetic Bearing

Figure 5-2 is an active bearing design presented in [5] that acts as an active bearing with both axial and radial forces. The permanent magnet reduces the current needed in the bearing and thus decreases the bearing losses. Figure 5-3 is an active radial bearing from [5] which works similar to the combination bearing in Figure 5-2. Other possible active magnetic bearings can be found in [6] and [7]. All of these active bearings are common in that permanent magnets are used to reduce the amount of flux produced by bearing windings to generate force and thus reduce the bearing loss.

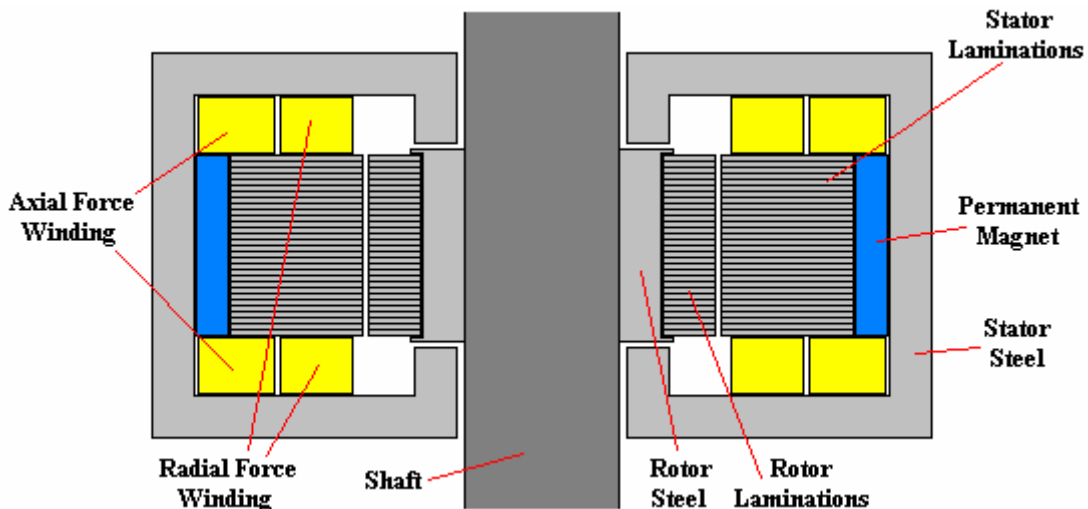


Figure 5-2: Active Combo Radial and Axial Bearing

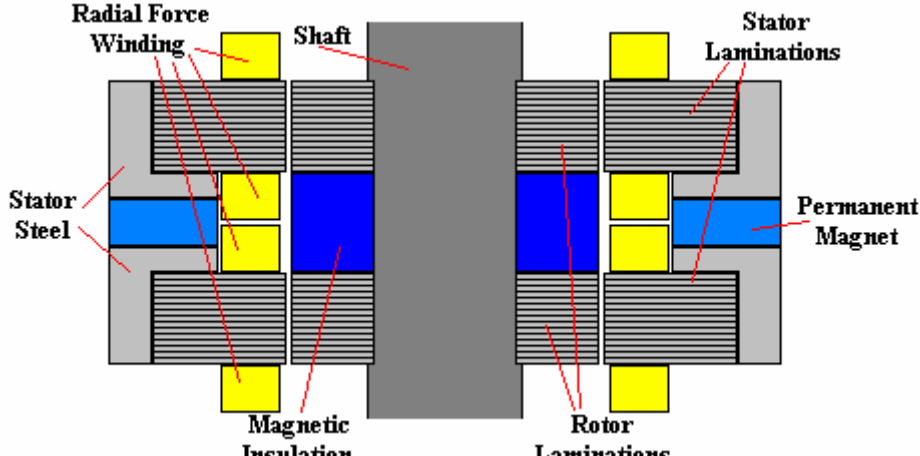


Figure 5-3: Active Radial Bearing

The full-scale flywheel will use active magnet bearing due to their lower cost. A combination axial and radial bearing needs to be used with either one or two other radial bearings. The commercialization of magnetic bearing is ongoing by numerous companies such as SKF, AVCON Inc., and Waukesha Bearings to name just a few. Purchasing bearing from such companies will result in a reliable and relatively low cost bearing system.

5.3 Emergency Touchdown Bearings

Since the magnetic bearings can only produce a limited amount of force, and the active magnetic bearings rely on an external power source, a magnetic bearing failure is a possibility. For this reason backup or touchdown bearings are included in the flywheel battery. These bearings have extra space so that they do not touch in normal operation, but in the case of a magnetic bearing failure they come into contact and act as a mechanical bearing.

6 Motor/Generator Selection

The main selection criterion for the motor/generator is interfacing with the wheel located in the vacuum enclosure. There are two reasonable methods for locating the machine outside the vacuum enclosure, but they both result in added complexity that increases cost and decreases reliability.

One possibility for locating the machine outside the vacuum is to use a magnetic coupling. This solution increases the cost by using a large amount of high cost permanent magnets, and expensive material that is able to maintain a vacuum with minimal thickness. The coupling also needs a very small gap between itself and the enclosure. This will require high performance and costly magnetic bearings.

A second solution [2] for locating the machine outside the vacuum is to use a ferro-fluidic seal. This solution diminishes the integrity of the vacuum and requires a vacuum pump to be attached to the enclosure at all times. The ability of this solution to operate at high rotation speeds ($>7,000\text{rpm}$) is also questionable.

If the motor/generator is instead located in the vacuum enclosure the system becomes very simple. The rotating member becomes a simple combination of a rotor, a wheel, a shaft, and

magnetic bearings. Since the only seals will be for the electrical wires and liquid cooling, the vacuum enclosure is also simplified.

The challenge for locating the motor/generator in the vacuum enclosure is that heat generated from loss can exit the rotor only through radiation. This means the loss in the rotor needs to be low. In addition, since radiation increases with the cubic of temperature difference between radiating surfaces, the rotor needs to be able to operate at high temperatures to increase the amount of heat transfer through radiation.

The requirement for low rotor loss eliminates the inverter driven induction machine, switched reluctance machine, and synchronous machine. The synchronous reluctance machine (SYNREL) and sinusoidal permanent magnet machine (PMAC) both ideally have a flux frequency of zero in the rotor and thus no rotor loss. While this ideal case obviously does not occur, the rotor loss can still be designed to be low.

For a thorough comparison of the SYNREL and PMAC machines for use in a flywheel battery five parameter are evaluated: the weight of the rotor, the machine efficiency, the cost of the machine and inverter system, the amount of rotor loss, and the maximum operating temperature of the rotor.

The weight of the rotor is important due to its contribution to the total weight the magnetic bearings need to levitate. The PMAC rotor will typically be lighter than the SYNREL. This weight difference is partially due to the higher torque per amp that is achievable in the PMAC, which correlates into a shorter length rotor for a given outer diameter. In the case of an axially laminated SYNREL machine the difference is also due to the heavier weight of the nonmagnetic layers compared to the permanent magnets of the PMAC. The conventionally laminated SYNREL does not have these heavier nonmagnetic layers, but the lower L_d/L_q ratio of this machine results in a longer rotor than the axial case. While the PMAC is clearly lighter, the difference is small compared to the wheel weight. For this reason motor/generator weight is not a large factor unless the flywheel requires very low energy storage and high power.

The efficiency of the machine is considered for both heavy load and low to no-load conditions. The heavy load case is important due to the large amount of power that can be lost at high load. The low to no-load condition is equally important for flywheel battery applications, since it affects idling loss. For many applications, there are long periods in which the flywheel is transferring little to no power to the grid. During these idling times, the motor/generator needs to use little power, or it will quickly discharge the flywheel battery's stored energy.

Due to the supplied flux from the permanent magnets, the PMAC has a higher torque per amp than the SYNREL machine. This results in the PMAC having less copper loss and thus a higher efficiency at high loads. The SYNREL machine can use more copper to reduce this difference, but this will add extra cost to the machine.

The supplied magnetic flux in the PMAC also causes a constant iron loss that increases with speed. The SYNREL has iron loss only if current is applied to the machine. This means the SYNREL has a higher efficiency at low to no-load conditions. Some papers suggest lowering the PMAC iron loss with an ironless stator and a Halbach permanent magnet array, but the Halbach array significantly increases the machine cost. In addition, the lack of machine inductance results in the need for special inverter schemes to control machine current. These schemes result in increased inverter loss that lowers the total drive system efficiency at higher

loads. This combined with the increased cost of the inverter and machine make it a less attractive option.

In the end, the most efficient machine depends on the application. If the machine is constantly charging and discharging at maximum power, the PMAC will be more efficient. If there are significant periods where the flywheel idles and holds its charge, the SYNREL is better. Most flywheel battery applications are between these two extremes, and it is difficult to determine which machine will result in the highest average efficiency.

The cost of the motor/generator includes the cost of the entire drive system including the inverter. The PMAC has a higher maximum power factor than the SYNREL machine and therefore can utilize a smaller and thus less costly inverter. The SYNREL machine's rotor is made of low cost sheet steel, while the PMAC uses costly rare earth permanent magnets. While the cost of power electronics has been and is expected to continue to decrease, [8] gives an expected price of \$85/kg for permanent magnets and predicts the cost will not decrease in the near future. Due to the extremely high cost of permanent magnets and the expected decreases in power electronics cost, the SYNREL is less costly now and probably will continue to be in the future.

Ideally, the rotor loss in both the PMAC and SYNREL should be zero. This of course is not the case in reality. Harmonics in the rotor will be induced due to several sources: the non-ideal shape of either the permanent magnets or the reluctance paths in the rotor, the slotting of the stator, and the non-ideal stator winding. In a non-salient PMAC, the permanent magnets typically have higher resistance than magnetic steel. The magnetic steel is also located at a significant distance from the stator resulting in reduced harmonics in the magnetic steel. These two properties result in the PMAC having lower rotor loss than the SYNREL.

While the rotor loss in a non-salient PMAC is lower than the SYNREL, this is not necessarily the case for a salient PMAC machine. In the case of a flywheel battery, the salient construction is more likely to be used since it's the only way to achieve high constant power over a large speed range. The only way to accomplish saliency is to locate some of the magnetic steel closer to the stator. This results in increased harmonics and thus increases rotor loss. Due to the need for saliency in the PMAC, the difference in rotor loss between the PMAC and the SYNREL will not be large.

So far, there does not appear to be a clear deciding factor between the SYNREL and the PMAC for most applications. However, the maximum operating temperature of the rotor will clearly show the SYNREL as being superior for flywheel applications. The amount of power radiated from the rotor surface is defined by the expression

$$P_{rad} = 5.7 \times 10^{-8} E_r A_r (T_r^4 - T_s^4) \quad (6-1),$$

where P_{rad} is the radiated power in W, E_r is the emissivity of the rotor, A_r is the rotors surface area in m^2 , T_r is the rotors temperature in K, and T_s is the stator temperature in K. From this expression, it can be concluded that a far greater amount of heat can be transferred from the rotor if it can operate at a high temperature.

For the PMAC machines, the maximum temperature is determined by the maximum operating temperature of the permanent magnets. Neodymium-iron-boron or samarium cobalt magnets are needed to achieve the performance so far assumed for the PMAC. These magnets have maximum operating temperatures of 150°C and 200°C respectively. However, actually

operating at these temperatures is not practical since the magnets are more susceptible to demagnetization from the motor current at high temperatures. Therefore, more practical rotor temperature limits are 100°C for neodymium-iron-boron magnets and 150°C for the samarium cobalt magnets.

Even operating at these lower temperatures, the possibility of permanent demagnetization is still a major problem for two reasons. Firstly, field weakening of the magnets is needed to achieve constant maximum power over a large speed range. Field weakening causes the magnets to operate close to their permanent demagnetization point. Therefore, inverter errors resulting in surged currents are more likely to cause permanent demagnetization. Secondly, while the motor/generator controls will limit current depending on rotor temperature, any errors in the control will cause permanent damage to the motor even if it occurs only briefly.

The SYNREL rotor, unlike the PMAC, is easily able to operate at temperatures as high as 250 °C with no problem. Since there are no magnets in the rotor, demagnetization is not a problem. While controls should be used to regulate the rotor temperature, any occasional short-term overtemperature conditions will not result in permanent damage to the machine. Due to the lack of demagnetization and ability to withstand occasional overcurrent and overtemperature, the SYNREL is considerably more rugged in a vacuum.

Due to the small differences between the PMAC and SYNREL with respect to rotor weight, efficiency, cost, and rotor loss, the main deciding factor in motor/generator selection is the temperature ability of the machine's rotor. For the temperature criteria, the SYNREL has a clear advantage due to both a higher operating temperature, and an ability to withstand occasional overcurrent and overtemperature.

7 Synchronous Reluctance Machine

The synchronous reluctance machine consists of a sinusoidally-distributed wound stator and a rotor with significantly different reluctance paths separated by 90 electrical degrees. The three phase stator winding is ideally sinusoidally-distributed and thus has a phase mmf of:

$$\begin{aligned}\vec{F}_a(t) &= N_{sp} i_a(t) \angle 0^\circ \\ \vec{F}_b(t) &= N_{sp} i_b(t) \angle 120^\circ \quad (7-1), \\ \vec{F}_c(t) &= N_{sp} i_c(t) \angle 240^\circ\end{aligned}$$

where N_{sp} is the number of turns per-phase per-pole [9]. The resulting stator mmf is

$$\vec{F}_s(t) = \vec{F}_a(t) + \vec{F}_b(t) + \vec{F}_c(t) = \hat{F}_s \angle \theta_{F_s} \quad (7-2).$$

In practice, the ideal sinusoidally-distributed winding is not practical, so distributed windings are used instead. However, the above equations apply to the fundamental component.

The rotor in the SYNREL needs to have a small reluctance in its direct axis and a large reluctance in its quadrature axis. These axes are spaced 90 electrical degrees from each other, and the reluctance should change gradually between the axes. The inductance is

$$L = \frac{N^2}{\mathfrak{R}} \quad (7-3),$$

where N is the number of turns and \mathfrak{R} is the reluctance of the machine. The direct inductance, L_d , of the machine is therefore large, while the quadrature inductance, L_q , of the machine is small. The ratio of L_d/L_q largely determines the performance of the machine.

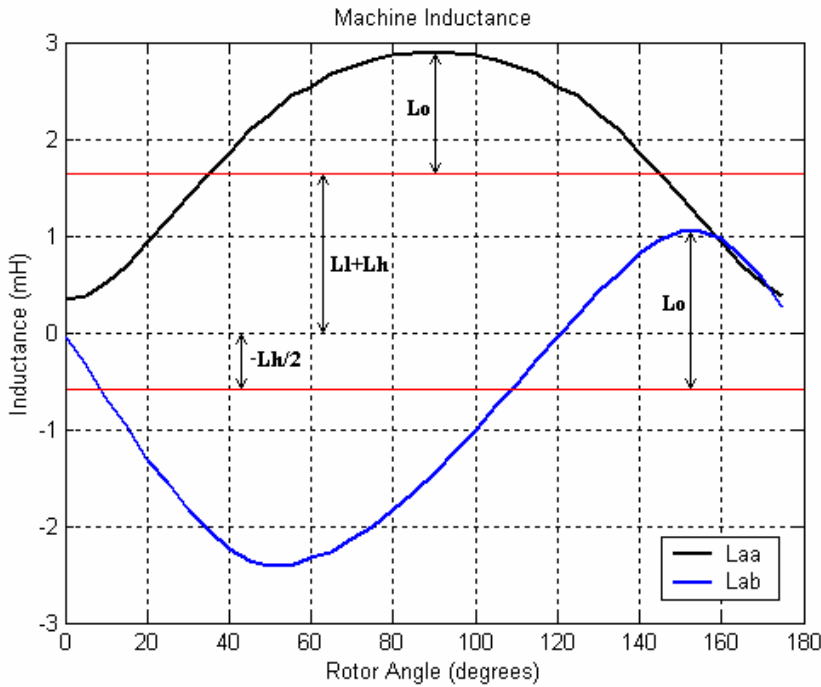


Figure 7-1: Self and Mutual Inductance Simulation Output

The values of the machine L_d and L_q inductances are derived from the machines self and mutual inductances. Figure 7-1 shows how both the self and mutual inductance are close to sinusoidal. The amplitudes and the offsets of these sinusoidal inductances at certain positions can be used to find L_h , L_o , and L_ℓ

$$\begin{aligned} L_h &= -(L_{ab60^\circ} + L_{ac30^\circ}) \\ L_{o1} &= \frac{1}{2}(L_{aa90^\circ} - L_{aa0^\circ}) \\ L_{o2} &= \frac{1}{2}(L_{ac30^\circ} - L_{ab60^\circ}) \\ L_\ell &= \frac{1}{2}(L_{aa0^\circ} + L_{aa90^\circ}) - L_h \end{aligned} \quad (7-4)$$

While L_{o1} and L_{o2} should in theory have the same value averaging them tends to give more accurate values for L_o . L_h , L_o , and L_ℓ are used to derive the self and mutual inductance of the machine using the following equations:

$$\begin{aligned} L_{aa} &= L_\ell + L_h + L_o \cos(2\theta r) \\ L_{bb} &= L_\ell + L_h + L_o \cos(2\theta r + 120) \\ L_{aa} &= L_\ell + L_h + L_o \cos(2\theta r - 120) \\ L_{ab} &= -\frac{L_h}{2} + L_o \cos(2\theta r - 120) \\ L_{bc} &= -\frac{L_h}{2} + L_o \cos(2\theta r) \\ L_{ac} &= -\frac{L_h}{2} + L_o \cos(2\theta r + 120) \end{aligned} \quad (7-5)$$

L_h , L_o , and L_ℓ along with an additional term L_{end} to account for end turn leakage inductance are also used to directly derive the L_d and L_q inductances of the machine.

$$\begin{aligned} L_d - L_q &= L_{dm} - L_{qm} = L_{de} - L_{qe} \\ L_{leak} &= L_\ell + L_{end} \\ L_{dm} &= \frac{3}{2}(L_h + L_o) \\ L_{qm} &= \frac{3}{2}(L_h - L_o) \\ L_{de} &= L_{leak} + L_{dm} \\ L_{qe} &= L_{leak} + L_{qm} \end{aligned} \quad (7-6)$$

In the above equations, new L_d and L_q notations are introduced. They represent the magnetic (L_{dm} , L_{qm}) and electrical inductances (L_{de} , L_{qe}). Both of these can be used for the torque expression, but the electrical inductances L_{de} and L_{qe} should be used in the voltage expressions.

Knowing the above inductances, the torque of the machine using the park transformation is:

$$\begin{vmatrix} i_d \\ i_q \end{vmatrix} = \frac{2}{3} \begin{vmatrix} \cos(-\theta_r) & \cos(-\theta_r + 120) & \cos(-\theta_r - 120) \\ \sin(-\theta_r) & \sin(-\theta_r + 120) & \sin(-\theta_r - 120) \end{vmatrix} \begin{vmatrix} i_a \\ i_b \\ i_c \end{vmatrix} \quad (7-7)$$

$$T = \frac{3}{2} \left(\frac{P}{2} \right) (L_d - L_q) i_d i_q = \frac{3}{2} \left(\frac{P}{2} \right) L_d \left(1 - \frac{L_q}{L_d} \right) i_d i_q \quad (7-8),$$

where P is the number of poles in the machine, i_d is the direct axis current, and i_q is the quadrature axis current. A large difference in L_d and L_q thus produces more torque per amp.

The voltage expressions of the SYNREL are:

$$\begin{aligned} V_d &= R_s i_d - \omega_e L_{qe} i_q \\ V_q &= R_s i_q + \omega_e L_{de} i_d \\ V_s &= \sqrt{V_d^2 + V_q^2} \end{aligned} \quad (7-9),$$

where R_s is the stator winding resistance and

$$\omega_e = \omega_m \left(\frac{P}{2} \right) \quad (7-10),$$

where ω_m is the rotation speed of the motor and P is number of poles. By using the voltage expressions and multiplying the torque expression by the rotational speed, the maximum power factor of the machine is

$$PF = \frac{\frac{L_d}{L_q} - 1}{\frac{L_d}{L_q} + 1} \quad (7-11).$$

Thus the maximum power factor also increases with the L_d/L_q ratio.

The simplest rotor for a two and a four pole machine are shown in Figure 7-2. These rotors use conventionally stamped laminations and are similar to a switched reluctance machine's rotor. This type of rotor typically has L_d/L_q ratios between two to three or lower [10].

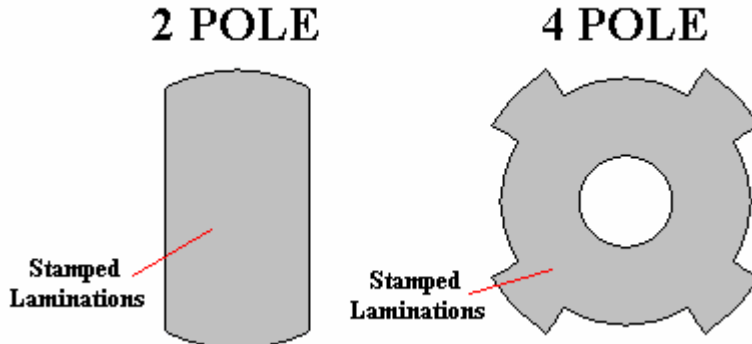


Figure 7-2: Simple Rotor

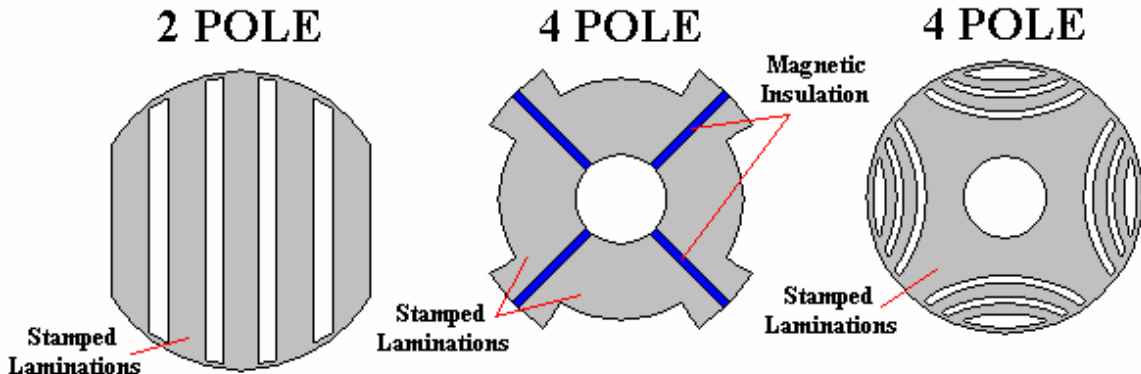


Figure 7-3: Improved Laminated Rotor

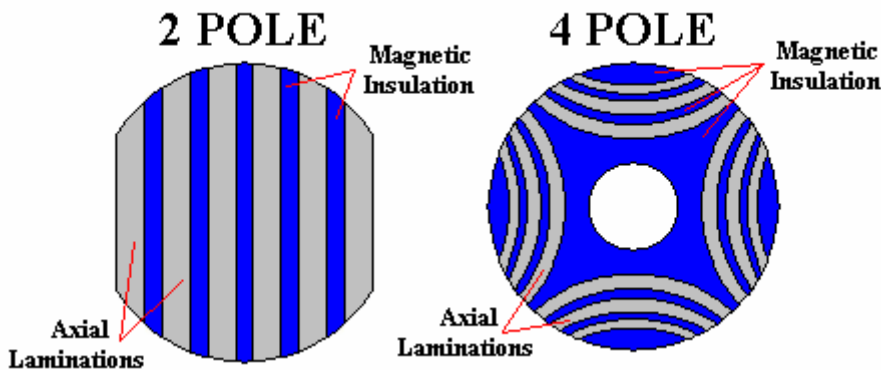


Figure 7-4: Axially Laminated Rotor

Some possible improvements to the conventionally laminated rotor are shown in Figure 7-3. In both the rotors, the two pole on the left and the four pole on the right, magnetic layers are connected by bridges on the periphery of the rotor. In many cases, additional structural bridges will be added internally to the rotor structure as explained in Sections 14.3 and 14.4. If the thickness of the bridges can be made significantly small, L_d/L_q ratios approaching eight can be

achieved. This is challenging though, due to structural stress from the high rotation speeds in flywheel applications.

To achieve even greater values of L_d/L_q ratio the bridges between magnet layers need to be omitted. The axially laminated rotors in Figure 7-4 completely eliminate the bridges and are able to achieve ratios larger than eight [10]. The high ratio makes the axially laminated rotor attractive due to high torque per amp and high maximum power factor.

8 Initial Design of Full-scale Motor/Generator

The initial motor/generator is designed under the assumption that it replaces the induction machine described in [2]. For this design, the normal operating speed of the machine will be from 7,500 rpm to 15,000 rpm. The maximum output power of the machine over this speed range should also always be greater than 2 MW.

The main goals of the analysis were low cost and high efficiency. The parameters varied during the design were the gap between the stator and rotor, the number of stator slots, the number of magnetic layers, and the rotor magnetic layer material. One important point is that this initial design did not include calculations on rotor loss, due to an inability to find them at the time. Section 14 will describe how rotor loss vastly changes the results of this initial design.

Machine length	41.5 inches
Stator diameter	19 inches
Rotor diameter	9.35 inches
Poles	2
Slots per-phase per-pole	7
Turns per-slot	1
Magnetic Layers Total	13

Table 8-1: Initial Full-scale Dimensions

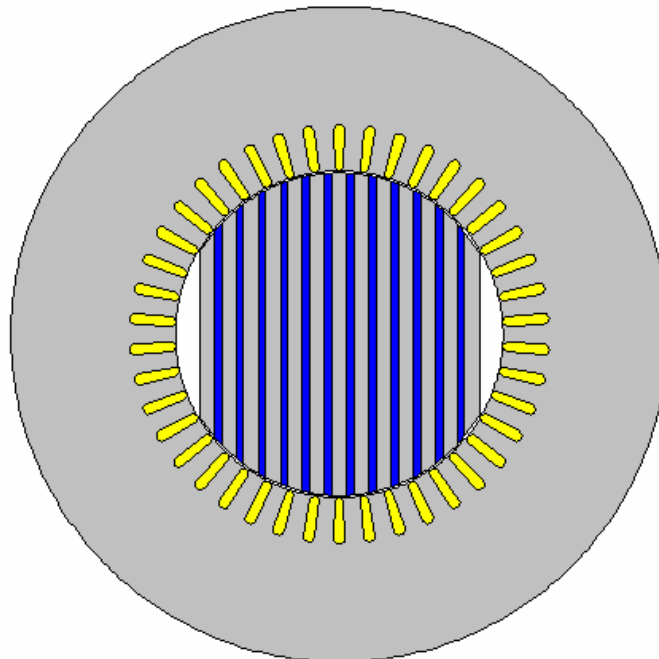


Figure 8-1: Initial Full-scale Cross-section

The dimensions of the initial full-scale machine with an axially laminated rotor are shown in Table 8-1 and Figure 8-1. Figure 8-2 and Figure 8-3 show the initial simulations for full-load power and efficiency respectively. The machine uses an inverter with a dc-bus voltage of 2.8 kV and a maximum current of 850 A RMS.

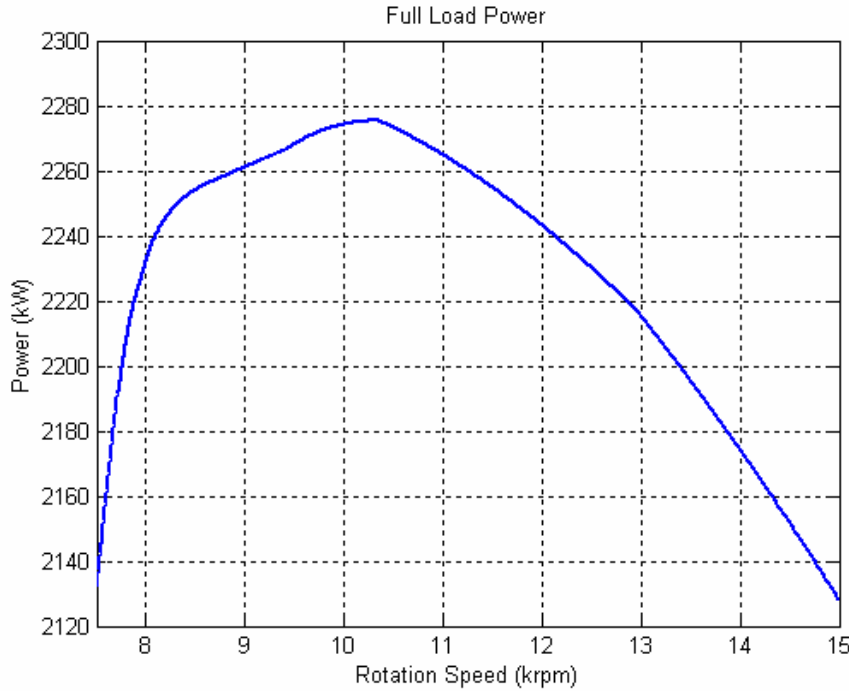


Figure 8-2: Simulation of Initial Full-scale Full-load Power

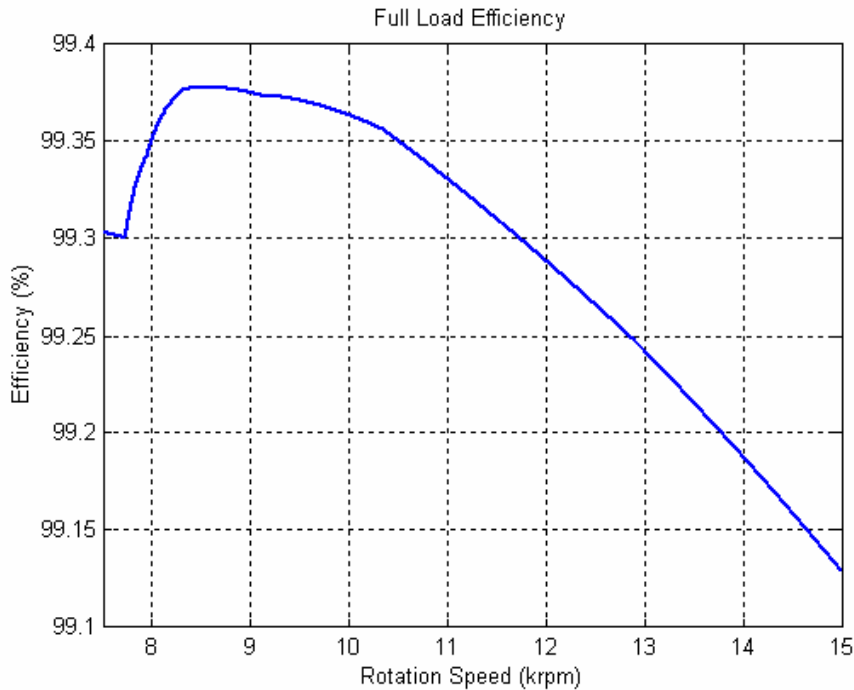


Figure 8-3: Simulation of Initial Full-scale Efficiency at Full-load Power

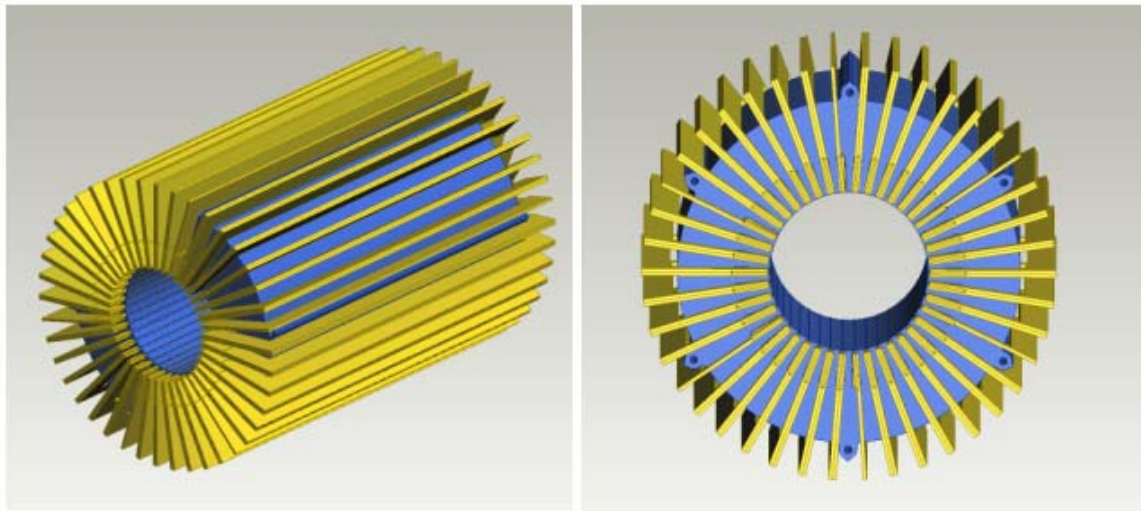


Figure 8-4: Possible Stator Using Ring Wound Configuration

The stator in the design is composed of 29 gauge M-15 silicon steel laminations. The stator windings are designed as copper bus bars. Figure 8-4 shows a possible stator with a winding using a ring-wound configuration. Due to the length of the machine, this winding is undesirable. A standard concentric winding configuration is preferred where the winding loops on the same end of the machine from positive to negative side of the phase and vice-versa. However, fabrication of the standard concentric winding in bus bar form for a two-pole machine is challenging.

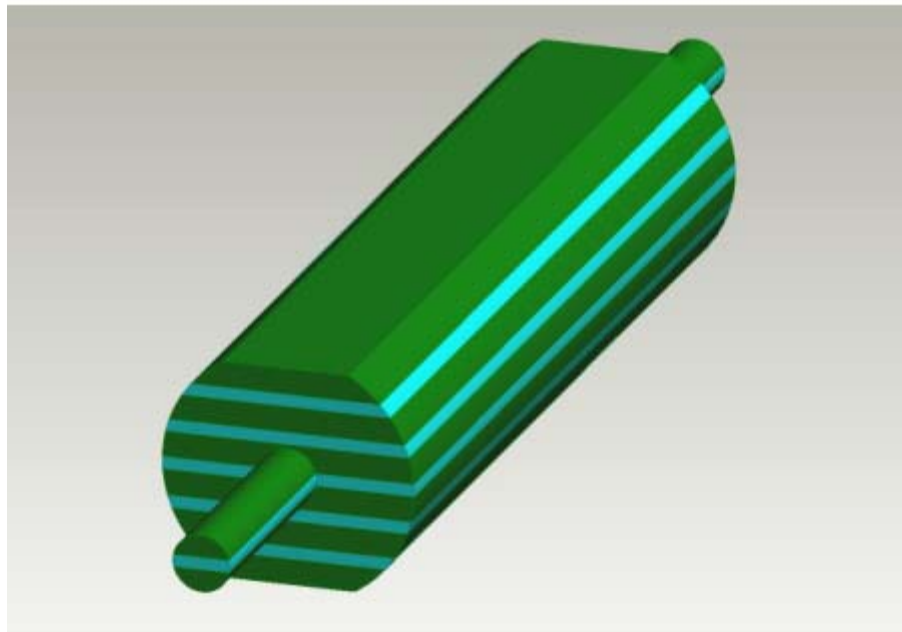


Figure 8-5: Axially Laminated Rotor

The machine's rotor is composed of alternating layers of magnetic steel and nonmagnetic steel as in Figure 8-5. While the simulation results show that silicon steel is the desired material for the rotor's magnetic layers, there is currently a lack of anyone supplying thick enough sheets. In addition, there are difficulties using silicon steel due to the high temperature of the brazing process. For these reasons, carbon steel is used for the magnetic layers. The carbon steel chosen

is Al-4130 due to its resistance ($22.3 \mu\text{ohm}\cdot\text{cm}$) and yield strength ($161,000 \text{ lb/in}^2$). The nonmagnetic layer material is Nitronic 50, which has high resistance ($110 \mu\text{ohm}\cdot\text{cm}$) and yield strength ($149,000 \text{ lb/in}^2$).

To construct the rotor, the magnetic and nonmagnetic layers are brazed together. The braze chosen is a Metglas® nickel base brazing foil. This braze has a high strength of $58,000 \text{ lb/in}^2$, but more importantly a higher resistance than most brazes. One disadvantage of this braze though is that it must be brought to temperatures greater than 1000°C . This high temperature is a problem for silicon steel, and is one of the reasons for using carbon steel.

The outer diameter of the rotor is determined by the strength of the rotor. Since the L_d/L_q ratio is roughly proportional to the circumference of the rotor divided by the air gap, it is desirable to use the largest rotor diameter possible for a given maximum rotation speed. Finite element stress analysis was done on a rotor with an outer diameter of 9.35 inches. At 15,000 rpm, a suitable safety factor is achieved considering the maximum braze stress [11].

9 Small-scale Design and Fabrication

The initial full-scale design is the basis for a scaled down machine for use in laboratory testing. For cost and safety reasons this small-scale design has a rating of only 10 kW, which results in a scale down factor of 200. Due to the large scaling, a compromise is needed between matching the parameters of flux density, current density, rotation speed, stator slotting, and voltage-to-current ratio.

Firstly, for safety reasons the dc-bus voltage of the system is set to 200V. Since its not a huge factor in changing the other scaling parameters, the voltage to current ratio is kept similar with a rating of 60.7 A RMS.

One of the main testing goals is to determine the iron loss in the rotor. This goal means similar types of harmonics should be generated in the rotor of the scaled prototype. To accomplish this, both the rotation speed and number of stator slots need to remain the same; otherwise the harmonic frequencies will be considerably different. The second reason for similar harmonics is to achieve similar flux density magnitudes. Due to the large magnitude of the scale down factor, this cannot be done perfectly but is designed to be as close as possible.

The result of matching the rotor harmonics is that the current density in the slots has to be much larger. The reason for this is to get a similar full-load power versus speed characteristic, and therefore the number of turns in each slot has to be increased to two. The current density needs to be increased, due to the increase in turns per slot, and the matching of flux density in the stator teeth.

Machine length	7.4 inches
Stator diameter	4.8 inches
Rotor diameter	2.2 inches
Poles	2
Slots per-phase per-pole	7
Turns per-slot	2
Magnetic Layers Total	5

Table 9-1: Small-scale Dimensions

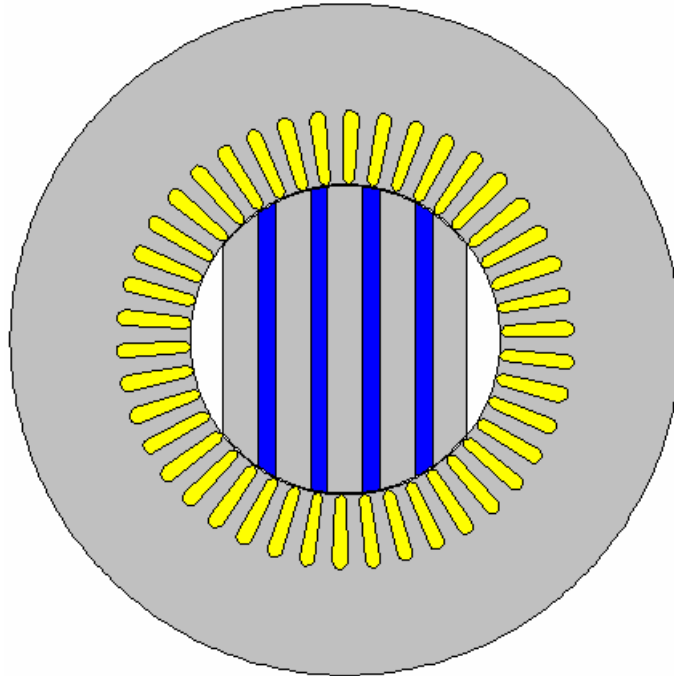


Figure 9-1: Small-scale Dimensions Cross-section

The small-scale design results in the dimensions and cross-section shown in Table 9-1 and Figure 9-1. Figure 9-2 and Figure 9-3 show the resulting simulation for full-load power and efficiency respectively. As can be seen, there are differences between the small-scale and the full-scale in both shape of the full-load power and efficiency curves. These differences are due to trying to maintain similar rotor harmonics and normal efficiency decreases due to the smaller size.

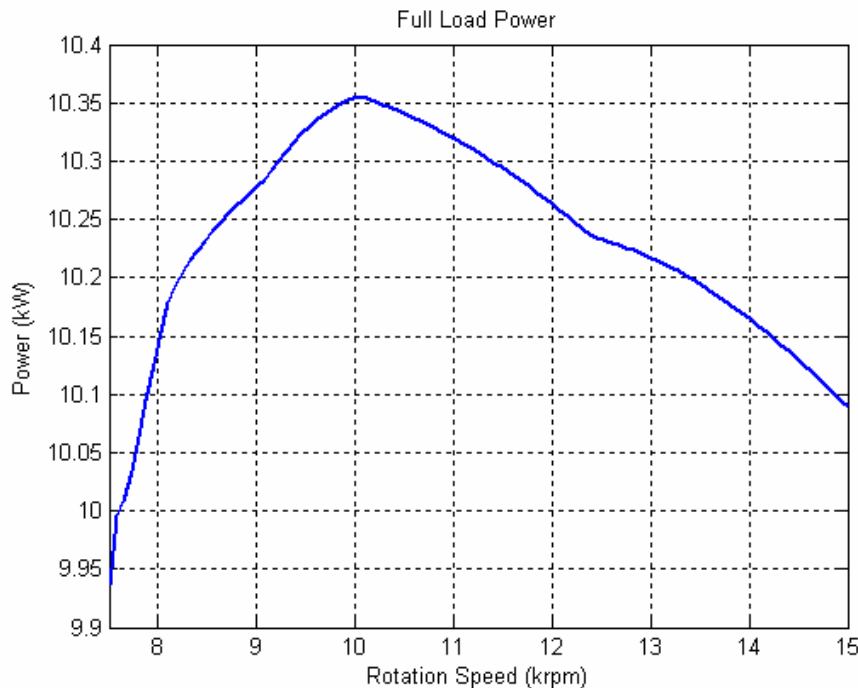


Figure 9-2: Simulation of Small-scale Full-load Power

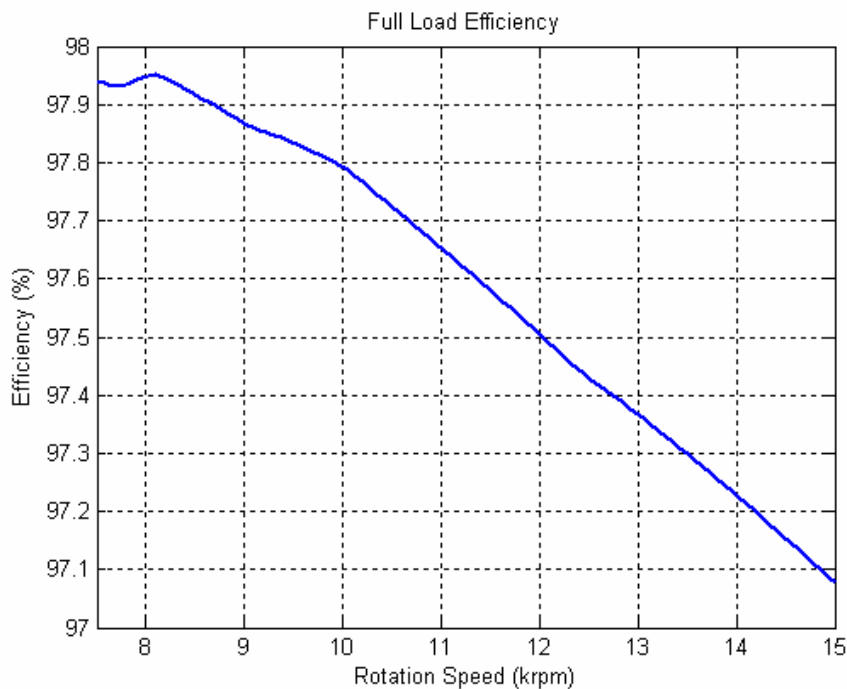


Figure 9-3: Simulation of Small-scale Efficiency at Full-load Power



Figure 9-4: Small-scale Prototype Rotor

The rotor in the small-scale machine is composed of magnetic layers of AI-4130 and nonmagnetic layers of Nitronic 60. While the magnetic layers are the same material as the full-scale, the AI-4130 steel is hot rolled instead of the cold rolled steel used in the simulation models. The use of hot rolled steel is more realistic though since cold rolled steel is typically not available in a thickness greater than approximately 0.125 inches. The sheets of magnetic and nonmagnetic layers are alternately stacked and brazed together. As described in Section 8, a nickel foil braze is used to increase the resistance of the rotor. After the layers are brazed together, the rotor is machined to the correct rotor and shaft diameters. The finished rotor is shown in Figure 9-4.

The small-scale stator is composed of 29 gauge M-15 silicon steel laminations. The preferred winding configuration is a standard concentric winding. However, the combination of two-poles and the small diameter make a concentric winding extremely difficult to fabricate. For this reason a ring wound configuration like that in Figure 8-4 is used instead.

The first attempted winding method used flat wires instead of bus bars, due to the two turns per slot. Figure 9-5 shows this first winding for the small-scale machine. The winding was done by hand and resulted in multiple shorts between the winding and the stator. In addition, the lower fill factor of the flat wire results in higher resistance than a bus bar winding.

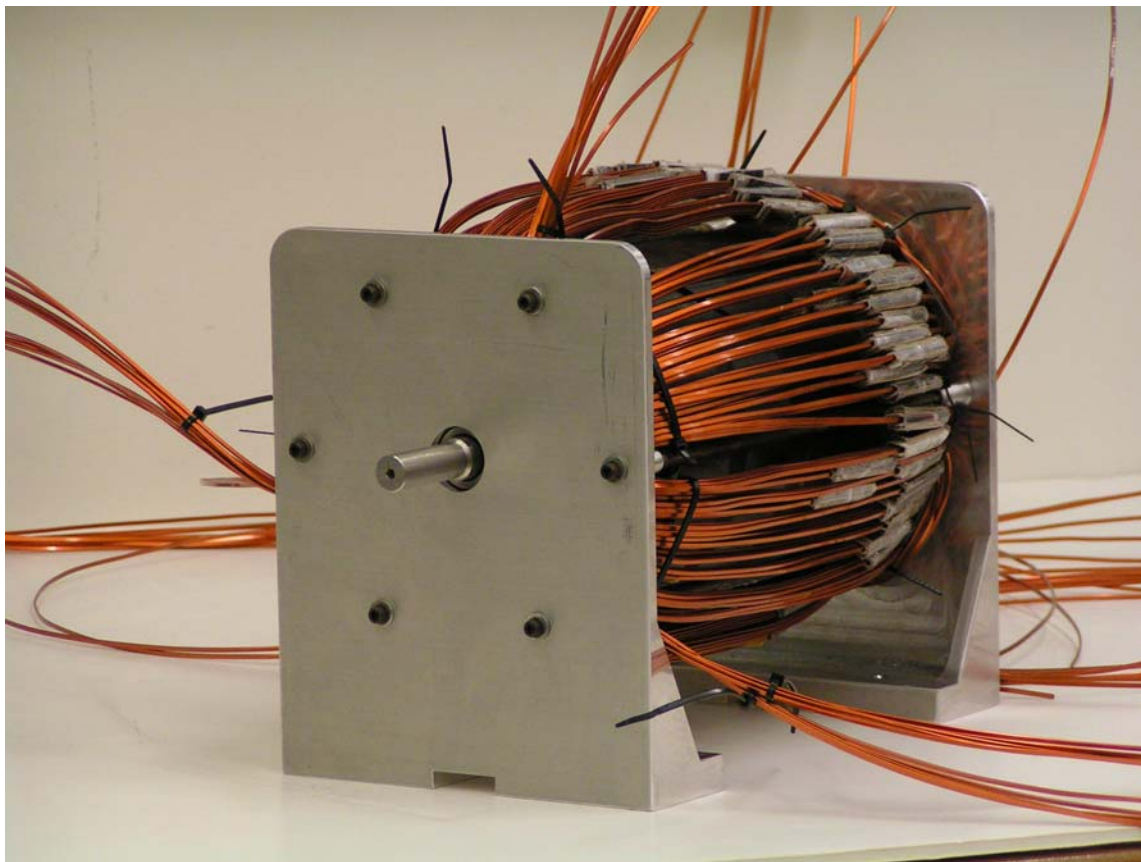


Figure 9-5: Initial Winding Attempt for Small-scale Prototype

To alleviate these problems it was desirable to develop a bus bar configuration that allows for two turns in each slot. Such a winding is possible by using a combination of two 'L' shaped bus bars and two 'C' shaped bus bars. Figure 9-6 shows two 'L' shaped bar and the two different 'C'

shaped bars. The smaller ‘C’ shaped bars provide the turn in each slot and are soldered to the small tab of the ‘L’ shaped bars. The larger ‘C’ shaped bars are soldered to the end of the ‘L’ shaped bars and connect one slot to the next.



Figure 9-6: ‘L’ and ‘C’ Shaped Bars for Rotor Winding

After all six individual phase portions are assembled, they are interconnected with the bars in Figure 9-7 that overlap the normal windings. Proper isolation from the stator and between bars is provided by using a combination of mylar slot liners and kapton tape. The final assembled machine is shown in Figure 9-8. The resulting winding has no stator shorts and a suitable slot fill factor.

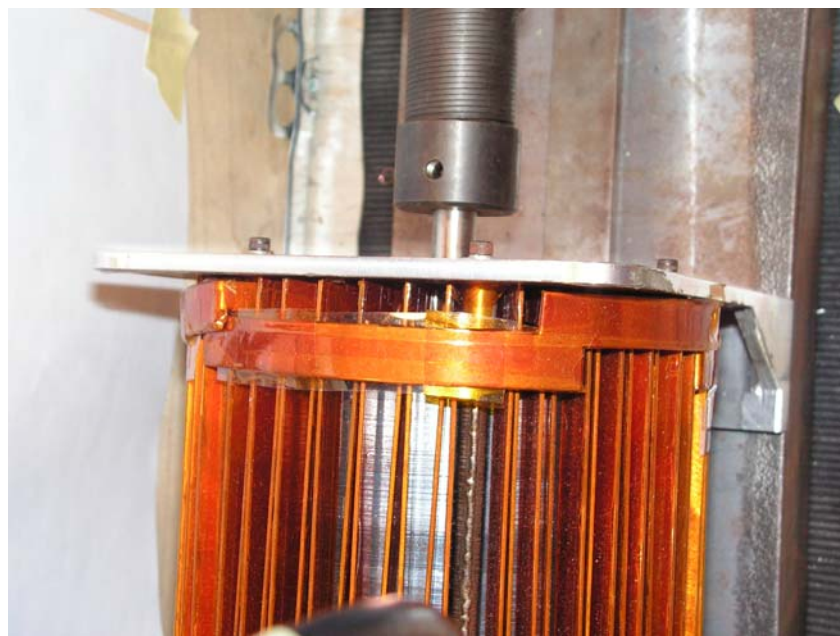


Figure 9-7: Phase Interconnect Bars

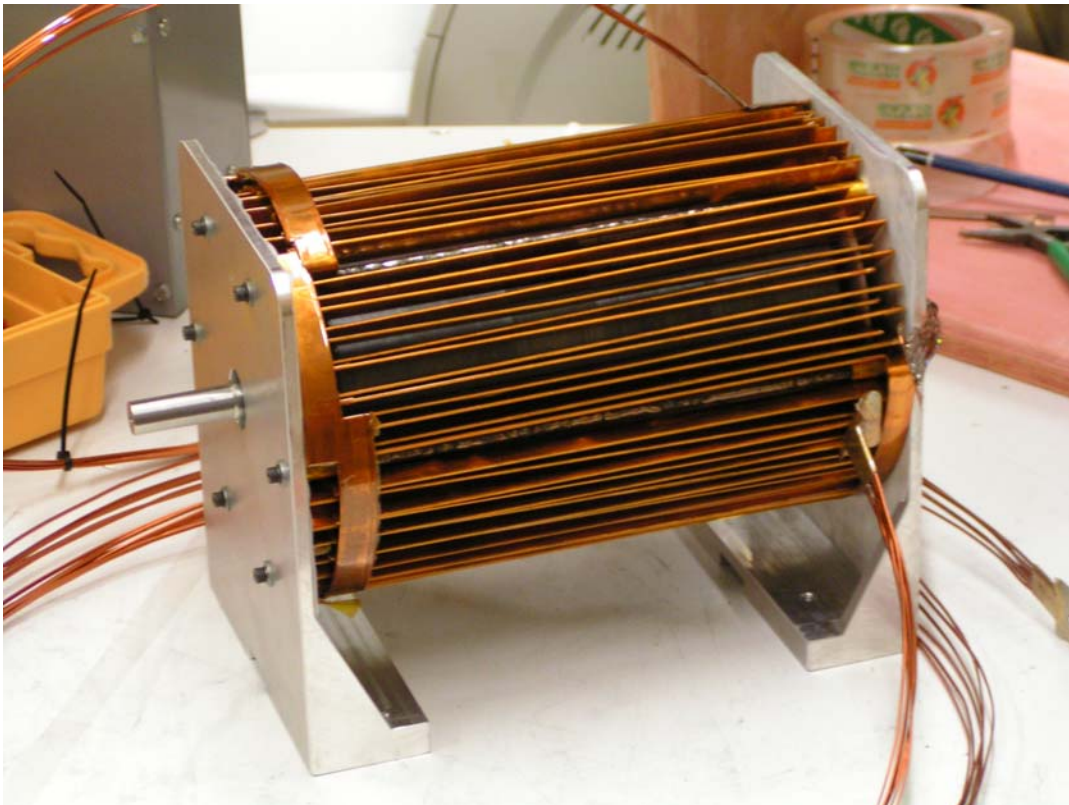


Figure 9-8: Final Small-scale Machine

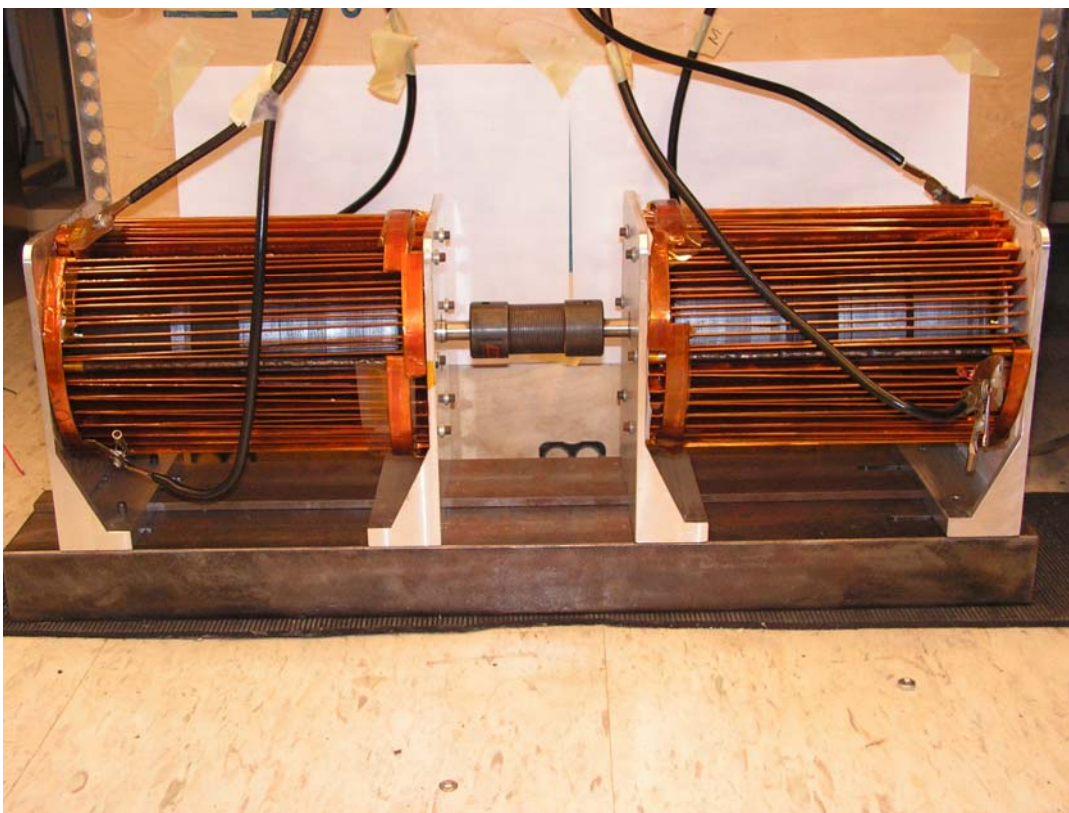


Figure 9-9: Coupled Small-scale Machines

End plates are fabricated to hold the stator and rotor together. These end plates are mounted on a rail that allows for alignment of two machines for back-to-back testing. An encoder is also added to each machine to allow for measurement of the machine's position and speed. As seen in Figure 9-9, two of these machines are fabricated, and their shafts are coupled together using a high-speed coupling.

10 Inverter and Test Setup Design

Machine testing is mainly done using a back-to-back setup. Figure 10-1 shows a simplified diagram of the setup. Two small-scale machines are placed on a common test bed and coupled together with a specialty high-speed coupling. The three phase legs of the two inverters are independently connected to the three phases of each machine. The two inverters dc-buses are then connected together along with an external dc power supply. This external power supply provides the power to accelerate the machine and supplements the power loss in the system.

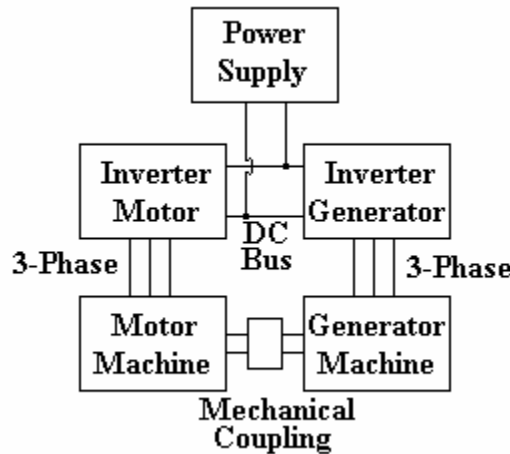


Figure 10-1: Simplified Back-to-back Test Setup

A control system interfaces with the inverters through pulse width modulation (pwm) inputs, fault logic, and current sensing. Additional sensors are also included in the test setup to allow for additional calculations and error checking. These sensors include a dc-bus voltage sensor, dc-bus current sensors, a rotor infrared thermal sensor, and two extra phase current sensors.

10.1 Inverters

The inverter receives pwm signals and outputs serial data corresponding to the phase currents of the machine. The second and third versions of the inverter also have fault protection to prevent current shoot-through or overcurrent conditions.

The three phase currents are sensed across accurately laid out copper traces. These traces act as sensing shunt resistors. The voltage drops across these shunt resistors are amplified by a high gain instrumentation amplifiers. The output voltage of each amplifier is then converted by an analog to digital converter into serial data. This type of current sensing is able to achieve high noise immunity since the analog paths are kept short, and the digital signals on the long lines are difficult to corrupt.

The first inverter shown in Figure 10-2 uses an IGBT module containing six IGBTs and six diodes. A combination of optocouplers and high current drivers turns on and off these switches according to the input pwm signals. This first design resulted in several motor faults that destroyed modules. To alleviate the problem a second version was made in which overcurrent fault circuitry is added, and the pwm dead-band generation is done on the inverter instead of on the FPGA board. These additions prevented the destruction of any more IGBT modules but resulted in constant tripping of the fault circuitry. The second inverter version was thus also unusable.

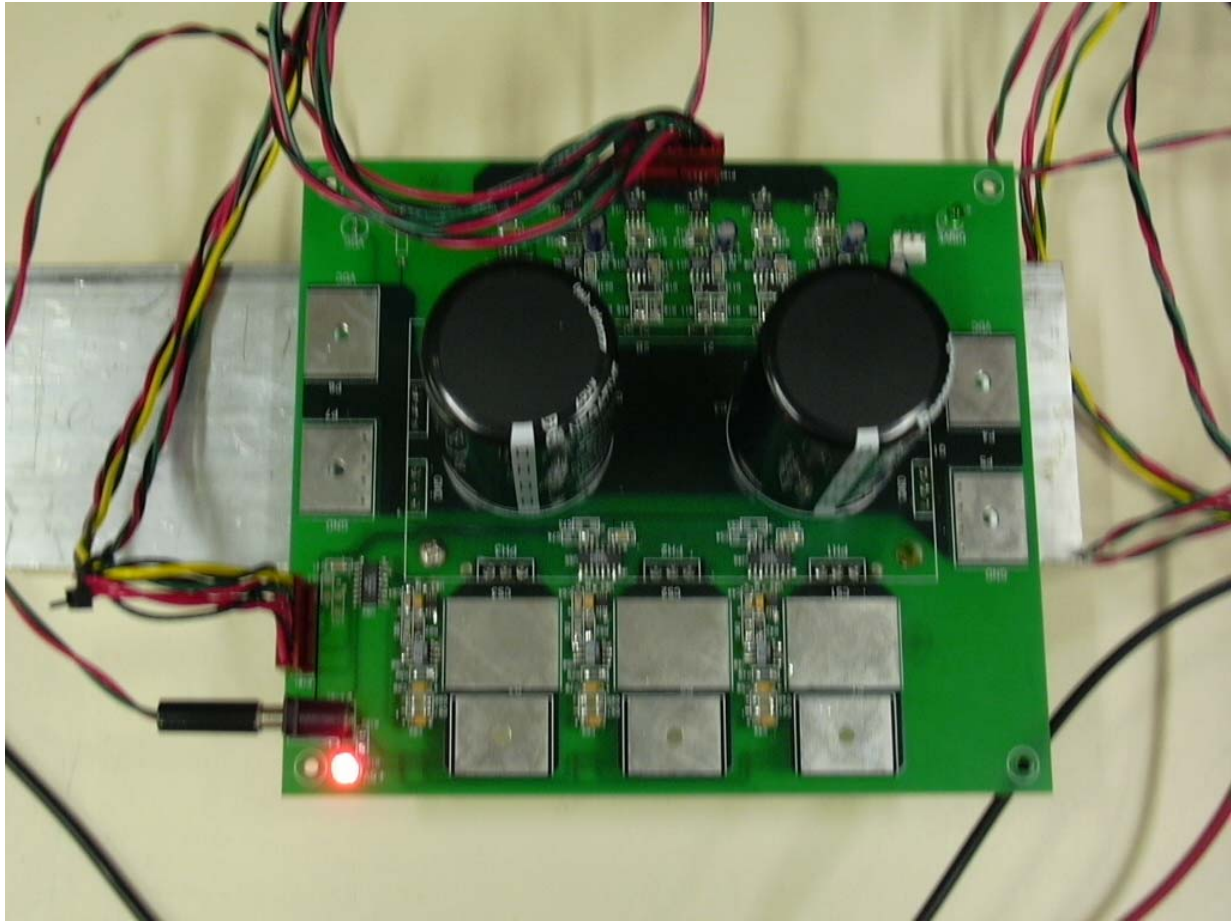


Figure 10-2: First Inverter for Small-scale Testing

The cause of the destroyed modules and constant fault tripping was from current shoot-through. Probing of the IGBT's drive circuitry shows that this is caused by excessive noise falsely turning on the IGBTs. This noise is generated by poor internal layout in the IGBT modules. The only way to reduce this noise is through the use of snubbers, but this increases the loss in the inverter. The use of an IGBT module also makes the layout of the snubbers difficult.

Instead of using snubbers a new inverter is designed and fabricated using single devices with only an IGBT and diode. This third version uses identical circuitry to the second version, but the layout is modified due to the individual devices. The final inverter is shown in Figure 10-3. This inverter is able to operate up to the full rated dc voltage of 200 V and up to the currents needed for motor testing. The schematic for the final inverter can be found in Appendix A.

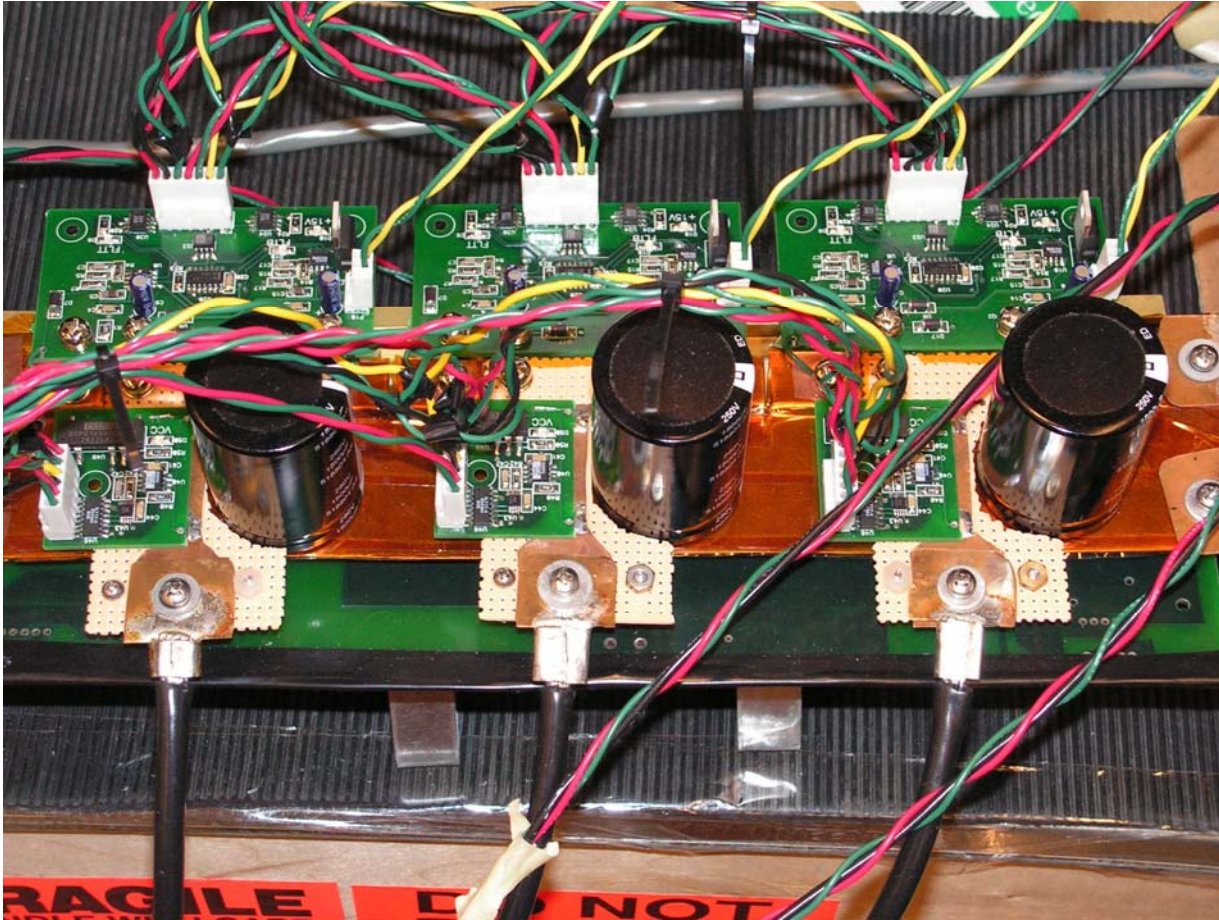


Figure 10-3: Final Inverter for Small-scale Testing

10.2 FPGA Control and Interface Board

A Field Programmable Gate Array (FPGA) Board is designed to allow for flexible control and interface with a dSPACE real-time digital signal processor (DSP) controller. For the test setup the FPGA board is designed to communicate with dSPACE, generate pwm signals, convert the serial data from the current sensors on the inverters, and provide an encoder interface. This one board interfaces with both inverters in the test setup.

The FPGA Board communicates with dSPACE through the use of a 16 bit bi-directional data bus and seven control lines. The dSPACE sends pwm duty cycles for the inverters to the FPGA through the bus, and the FPGA sends back the two machines phase currents, positions, and speeds. The FPGA generates pwm signals through the use of a 10 bit timer that produces a triangular digital waveform. This waveform is compared to the duty cycle values to produce the pwm outputs for the inverters. In addition, triggering of the inverter overcurrent fault protection disables these pwm outputs to prevent further inverter operation after a fault.

The inverter's phase current serial outputs are converted and stored in the FPGA's onboard RAM before being transferred to dSPACE for control purposes. Two identical serial logic blocks for each motor and a single serial timing block are used to shift in the serial data. Each block allows the serial data for all three motor phases to be clocked in simultaneously. This ability results in concurrent readings of phase current and high sampling rates. The serial timing block also takes

current readings at the peaks of the pwm timer's triangular waveform. Since the triangular peaks correspond to the least likely occurrence of IGBTs switching, this reduces the affects of noise generated by the IGBTs. Sampling in this manner results in a sampling frequency of 40 kHz, which is faster than the dSPACE controller can read the data.

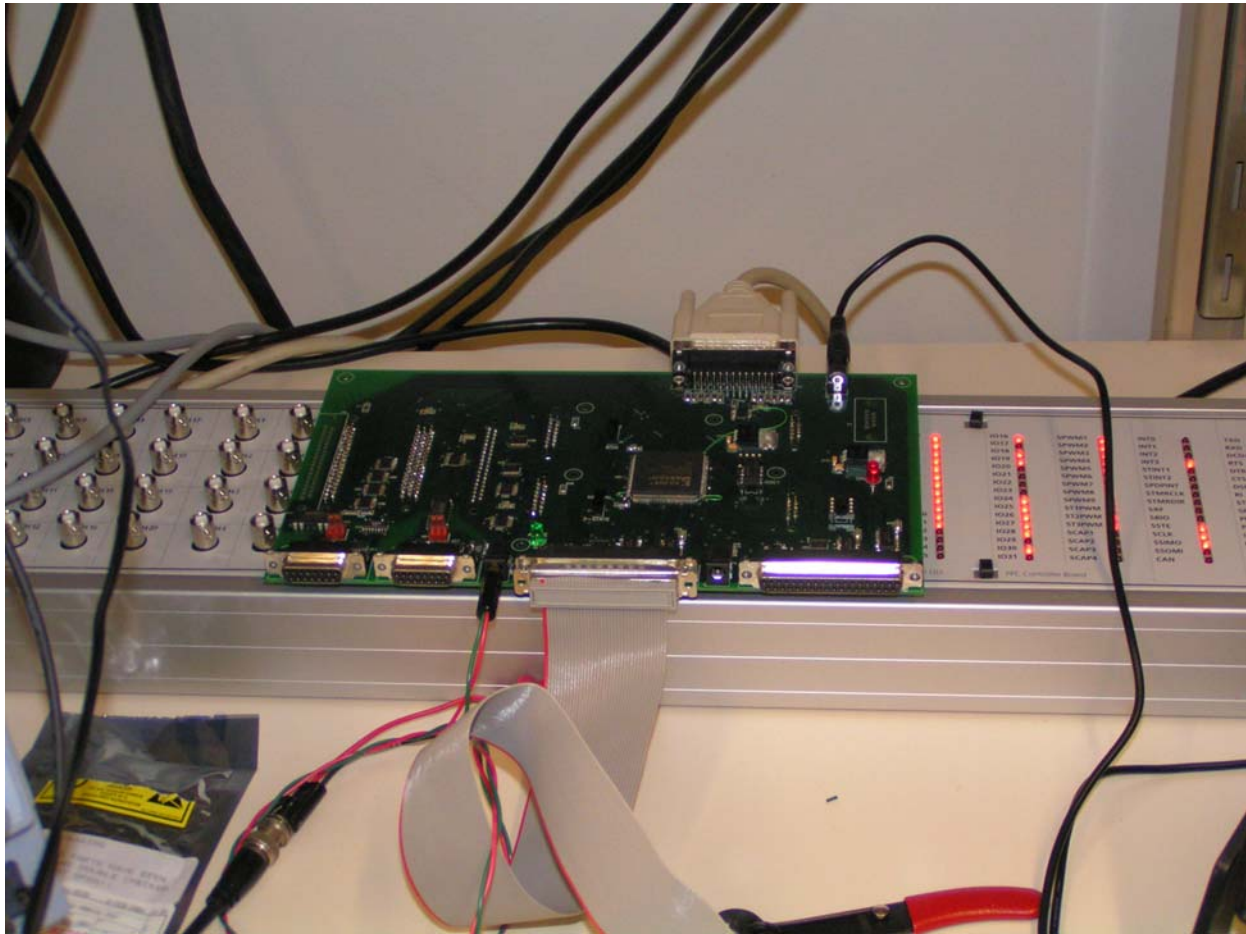


Figure 10-4: FPGA Interface Board and dSPACE Controller Box

The FPGA's encoder interface logic senses the position and speed of both machines. This interface first filters the three input encoder signals (zero phase, ninety phase, and index) to decrease errors from noise. The filtered signals increment or decrement a counter whenever the zero or ninety phase signals change from a zero to a one or vice versa. The counter is additionally cleared whenever the index signal goes high. The outputs of two sets of these counters correspond to each machine's position. These positions are stored in FPGA RAM until transferred to the dSPACE controller.

The speed sensing in the FPGA is done by two different methods. The first method tracks the number of zero and ninety phase pulses occurring during a set sample time. The second method counts the elapsed time between pulses. The first method results in greater accuracy at higher rotation speeds, but the lowest sensed speed is higher than in the first method.

Figure 10-4 shows the FPGA board connected to the dSPACE controller. The FPGA logic is found in Appendix B.

10.3 dSPACE Controller

The dSPACE controls the two machines and sends and receives the data to the FPGA board. The controller uses a combination of SIMULINK and C code generated using MATLAB. The SIMULINK model and C code are compiled by dSPACE into machine code that is downloaded to a DSP located in the dSPACE hardware. The dSPACE system works together with the FPGA board to implement the desired control. In addition, dSPACE ControlDesk allows for real-time control inputs to change the machines operating conditions and record measurements. An example of the ControlDesk input screen is shown in Figure 10-5.

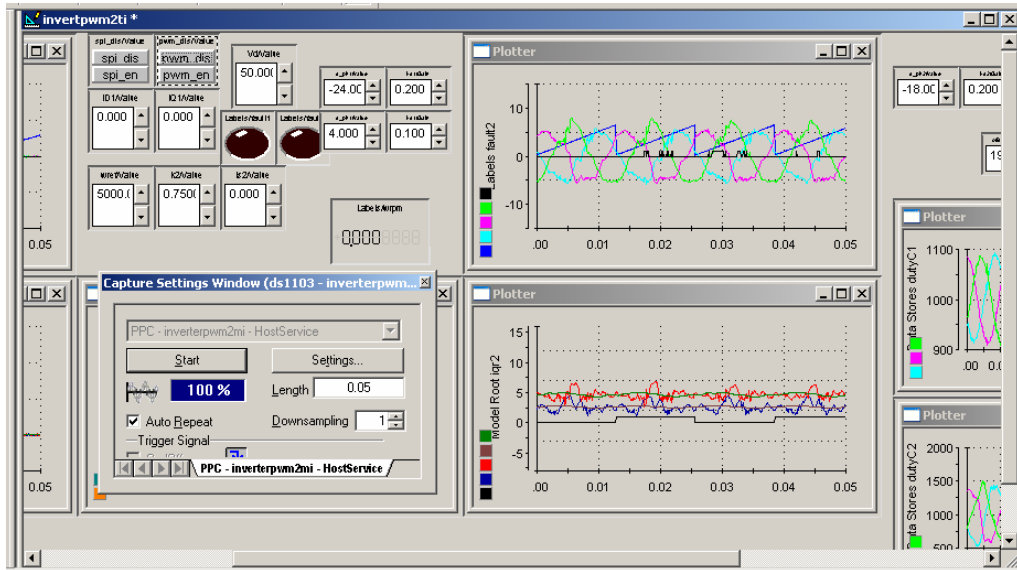


Figure 10-5: Example ControlDesk Input Screen

10.4 Additional Sensors

Besides inverter current and encoder measurements, additional sensors are included in the test setup. Sensors are included to read the dc-bus voltage, the dc current between the inverters, and the dc current between the inverter and the dc power supply. These three sensors allow for the calculation of the power flow in the dc-bus.

Two additional phase current sensors are included in the test setup. Unlike the inverter current sensors these sensors are Hall-effect based. The inverter phase sensors are shunt resistors and can heat up due to heavy loading. This heating will change the shunt resistance and will throw off the inverter's current readings. The Hall-effect based current sensors do not change with heavy loading. The inverter currents are periodically checked against these extra Hall-effect sensors to make sure the inverter shunts are not heating up.

An infrared thermal sensor is included in the test setup to measure the rotor temperature. This sensor consists of an optical sensor that is able to sense the heat of a surface. Since the sensor does not need to touch the measured surface, it is able to measure the rotor temperature while it rotates. This sensor is included in an attempt at deriving rotor loss from the rotor shaft temperature.

All of the additional sensors output a voltage that is directly input to dSPACE. The complete test setup includes the two small-scale machines, the two inverters, the dc power supply, the FPGA board, dSPACE, and the additional sensors as shown in Figure 10-6.

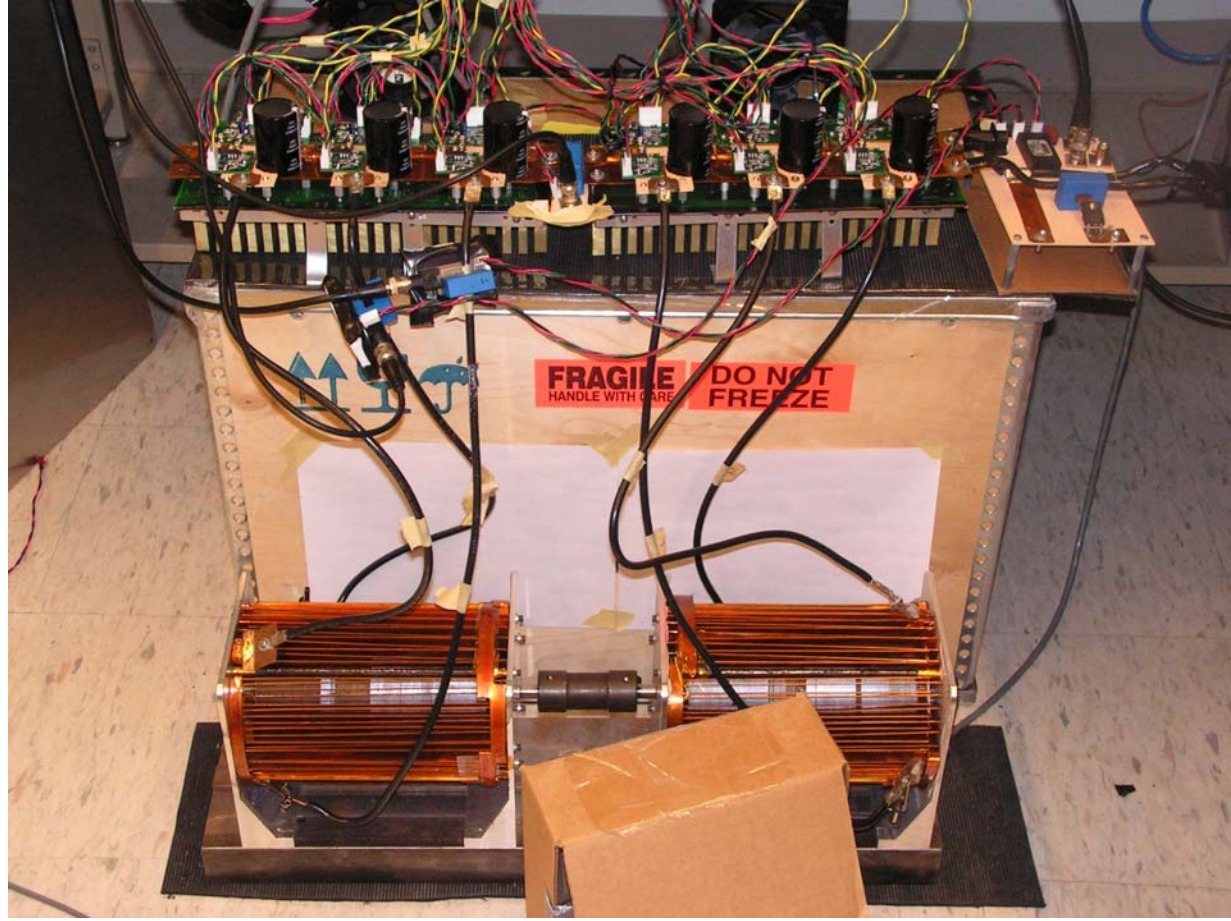


Figure 10-6: Back-to-back Setup Test Setup

10.5 SIMULINK Controller for Test Setup

dSPACE generates machine code from a SIMULINK model of the desired controller. Machine Code is also generated from C Code written in MATLAB for interfacing with the FPGA board. Figure 10-7 is the SIMULINK model of the first controller. The currents i_d and i_q for this controller are held at a constant ratio that can be changed in the Controldesk. This controller does speed control and is used for one of the machines in the test setup.

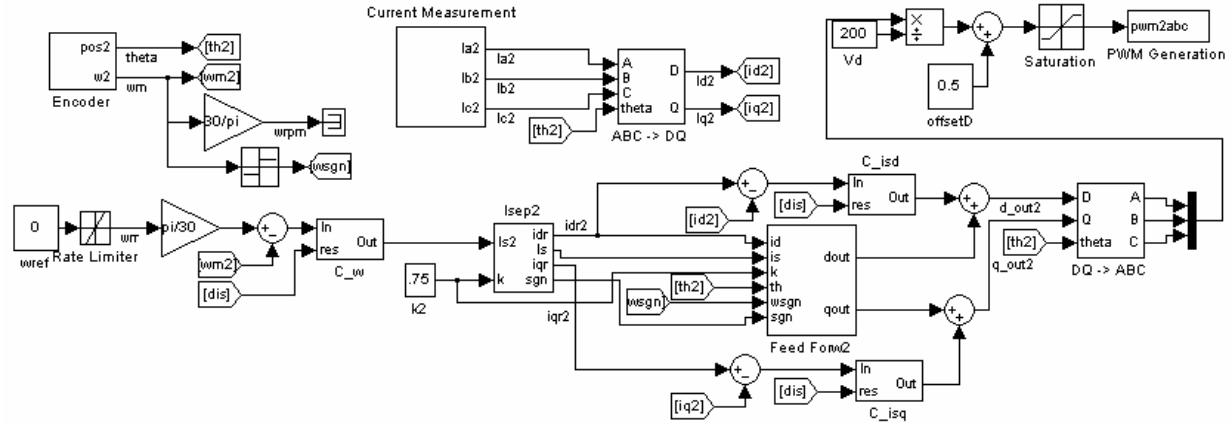


Figure 10-7: Speed Controller For Constant Speed Machine

The SIMULINK model in Figure 10-8 independently controls both the i_d and i_q currents. The independent control of i_d and i_q allows for current sweeping during testing to determine rotor performance under different current angles.

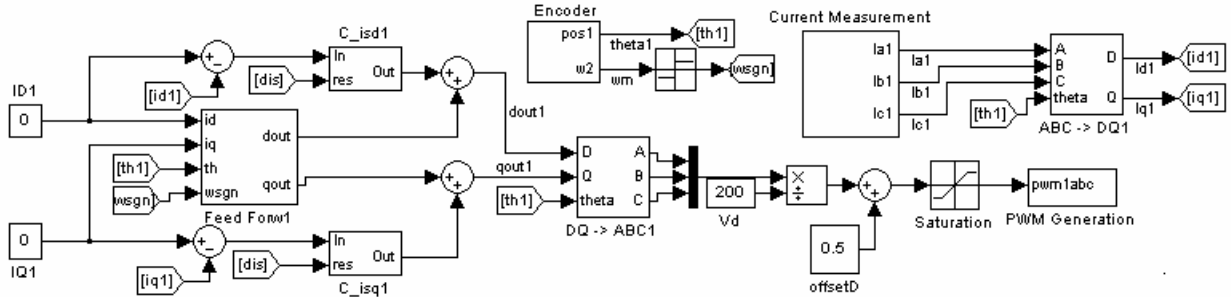


Figure 10-8: Independent i_d and i_q Current Controller for Machine Under Test

For both controllers feed-forward control is added to create a more sinusoidal waveform. The feed-forward controllers are done in two different ways for the two different controllers as seen in Figure 10-9 and Figure 10-10. The basic concept of both these feed-forward controllers are basically the same though.

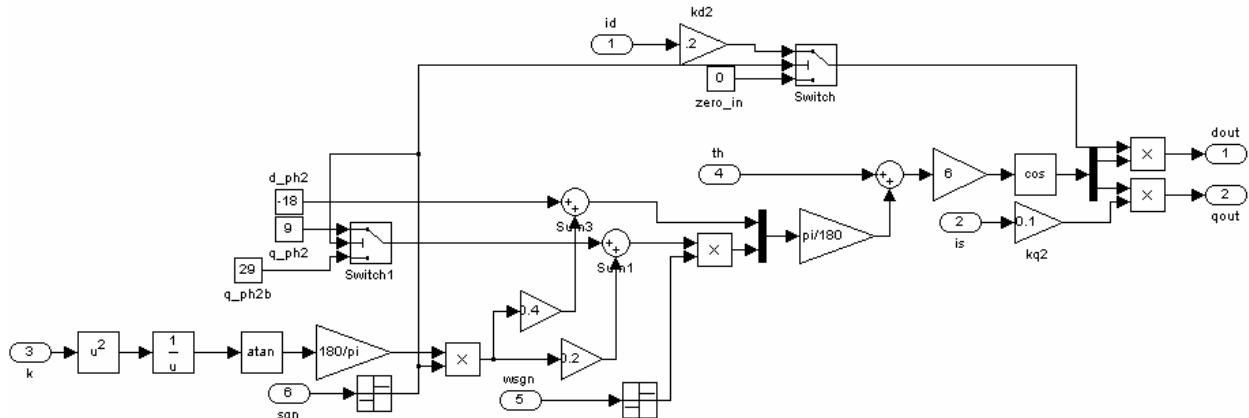


Figure 10-9: Feed-forward Control for Constant Speed Machine

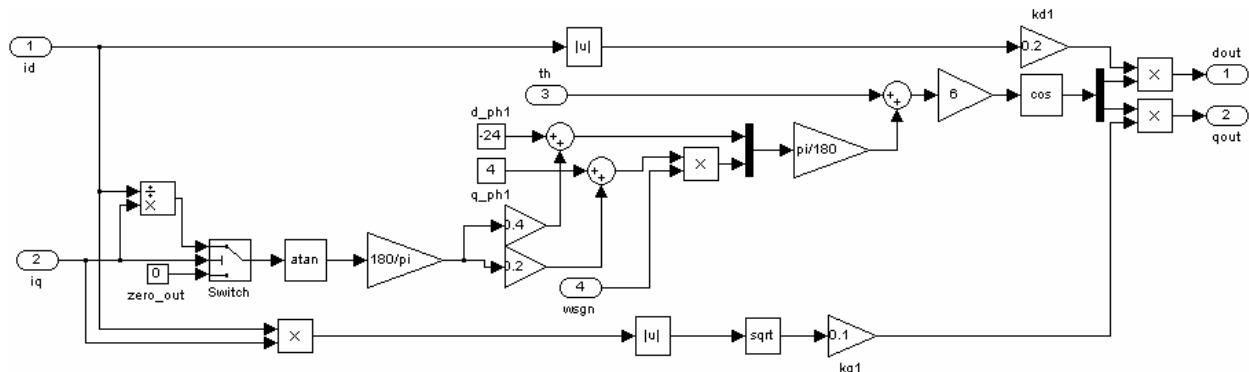


Figure 10-10: Feed-forward Control for Independent i_d and i_q Current Controller

For the feed-forward controller the motor position is input to create a control signal with a frequency six times the rotation frequency. This frequency is equivalent to a third order harmonic and is needed due to the harmonic created by the three phase winding. The d and q

axis currents of the machine determine the magnitude and phase shift of the control signals. The different ways the reference currents are generated determine how the feed-forward controllers produce its output terms. The dSPACE ControlDesk is also configured so that the magnitudes and phases of the feed-forward control can be scaled or even eliminated.

In the controller model, additional blocks are included to perform calibration of the sensors. Transforms for both dq to abc and abc to dq are also included in the models. The equations for these transforms are

$$\begin{vmatrix} x_d \\ x_q \end{vmatrix} = \frac{2}{3} \begin{vmatrix} \cos(-\theta_r) & \cos(-\theta_r + 120) & \cos(-\theta_r - 120) \\ \sin(-\theta_r) & \sin(-\theta_r + 120) & \sin(-\theta_r - 120) \end{vmatrix} \begin{vmatrix} x_a \\ x_b \\ x_c \end{vmatrix} \quad (10-1)$$

$$\begin{vmatrix} x_a \\ x_b \\ x_c \end{vmatrix} = \begin{vmatrix} \cos(-\theta_r) & \sin(-\theta_r) \\ \cos(-\theta_r + 120) & \sin(-\theta_r + 120) \\ \cos(-\theta_r - 120) & \sin(-\theta_r - 120) \end{vmatrix} \begin{vmatrix} x_d \\ x_q \end{vmatrix} \quad (10-2).$$

Appendix C includes the full control model and the broken down model blocks.

11 Test Results

The goal of the small-scale testing is to find the performance of the machine and determine how closely it matches simulations. The results of this testing are used to modify the simulations and change the full-scale machine design. Initial tests are done with the two small-scale machines held in a stationary position. The remainder of the testing is done with rotating machines in a back-to-back setup.

Tests using the back-to-back setup are done by utilizing one of the machines to maintain a constant speed. The other machine is the machine under test, and constant currents are applied to it. The constant speed machine acts as either a motor or a generator in response to what the machine under test does. This type of setup allows for the collection of data at constant speed and current on the machine under test. Data can also be collected from the constant speed machine, but at low torques this data is not as useful due to constant switching between motoring and generating operation.

11.1 Initial Testing

The first test finds the resistance of the machine phases. The resistance is found by applying a known current to two of the stator phases and measuring the winding voltage. Table 11-1 shows the resistances of the three phases for each machine and also the simulation values. The differences in phase resistances are most likely due to variability in the quality of solder joints between bus bars. The simulation calculations are fairly accurate, except the extra factor for solder joint resistance can be reduced.

	Machine 1	Machine 2	Simulation
PhaseA	21.24 mΩ	22.85 mΩ	25.20 mΩ
PhaseB	21.80 mΩ	23.16 mΩ	25.20 mΩ
PhaseC	21.89 mΩ	23.00 mΩ	25.20 mΩ

Table 11-1: Small-scale Phase Resistances

While the inductance testing is mainly done in the back-to-back setup, a standstill test is done initially. The inductance at standstill is difficult to measure since the rotor has a high reluctance at high frequencies. To get the inductance from standstill, the inverter is connected in series with several inductors and the machine. Different ac frequencies are applied and the voltage and current at the machine are measured. Measurements are taken with the stator current aligned with the rotor's d axis to find L_d and with the rotor's q axis to find L_q .

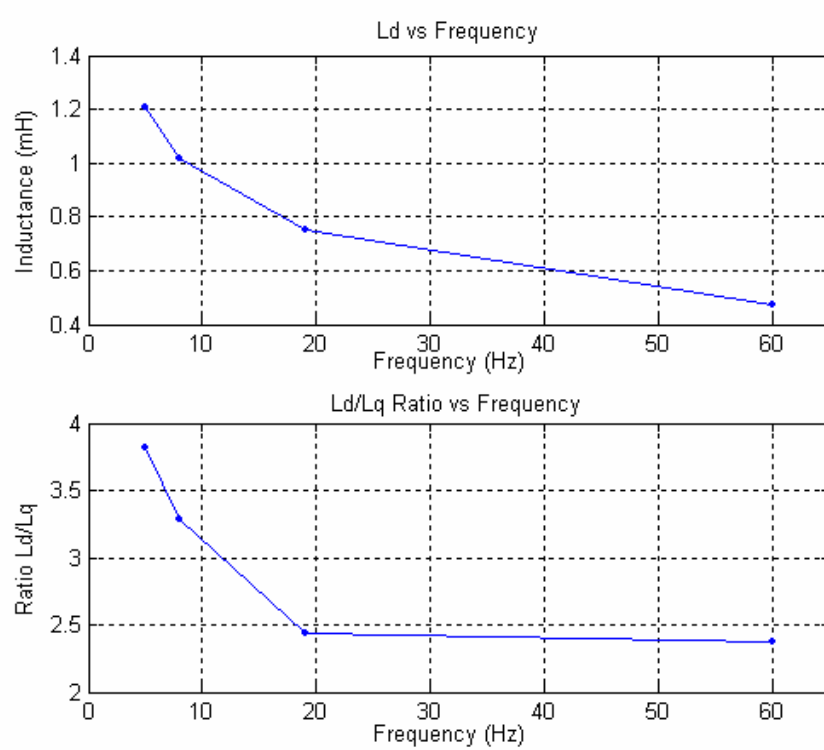


Figure 11-1: Initial Inductance Testing

In Figure 11-1 the inductance in the d axis and the L_d/L_q ratio increase significantly with lower frequency. Since the rotor's reluctance is lowest at dc, the increase in inductance is to be expected. Due to waveform distortion, harmonics, and noise, it becomes difficult to get accurate measurements at frequencies below 10 Hz. To get accurate results back-to-back testing is needed.

11.2 Back-to-back Tests

The remainder of laboratory testing is done using the back-to-back setup in Figure 10-6. To find the inductance in the direct and quadrature axes, the second machine maintains constant speed while direct (i_d) or quadrature (i_q) current is individually applied to the first machine. Measurements are taken when steady state conditions are reached. The model in Figure 11-2 shows that measuring the voltage V_q when i_d is applied to the machine allows for the calculation of the direct inductance, L_d . Similarly, applying a current i_q and measuring V_d will determine the quadrature inductance, L_q . Plots of these inductances versus current are shown in Figures 11-3 and 11-5.

It is also possible from these inductance tests to measure the combined stator and rotor loss. In Figure 11-2 resistors R_{m1} and R_{m2} model the iron loss in the machine [12]. While this is not a

highly accurate model of the iron loss, it gives a rough estimate. Figures 11-4 and 11-7 show the iron loss found during both inductance tests.

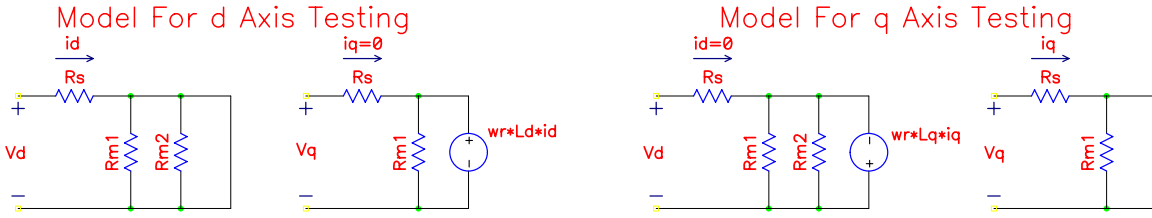


Figure 11-2: Simplified Model of Synchronous Reluctance Machine

The last set of tests find the loss in the motor for different i_d and i_q values. This is done by again using the second machine to maintain constant speed. A constant i_d current and i_q current are applied to the first machine and measurements are taken in steady state. This is done for various currents and operating speeds of 7,500 rpm, 9,000 rpm, and 10,500 rpm. The results are shown in Figures 11-9 through 11-14. There is no torque sensor in the setup due to the high rotation speed. Therefore, the loss for each machine cannot be decoupled, and the plots represent the combined loss of both machines.

11.3 Results of Back-to-back Testing

Figure 11-3 shows the direct inductance (L_d) difference between simulation and testing. Testing shows about a 10% decrease in inductance from simulation. This decrease is most likely due to the use of hot rolled steel instead of cold rolled. The variability of carbon content in AIS-4130 steel also may contribute to the lower value. Either of these two factors reduces the permeability and the saturation flux density of the steel and results in reduced inductance. However, the direct inductance of the machine is fairly consistent with the simulations.

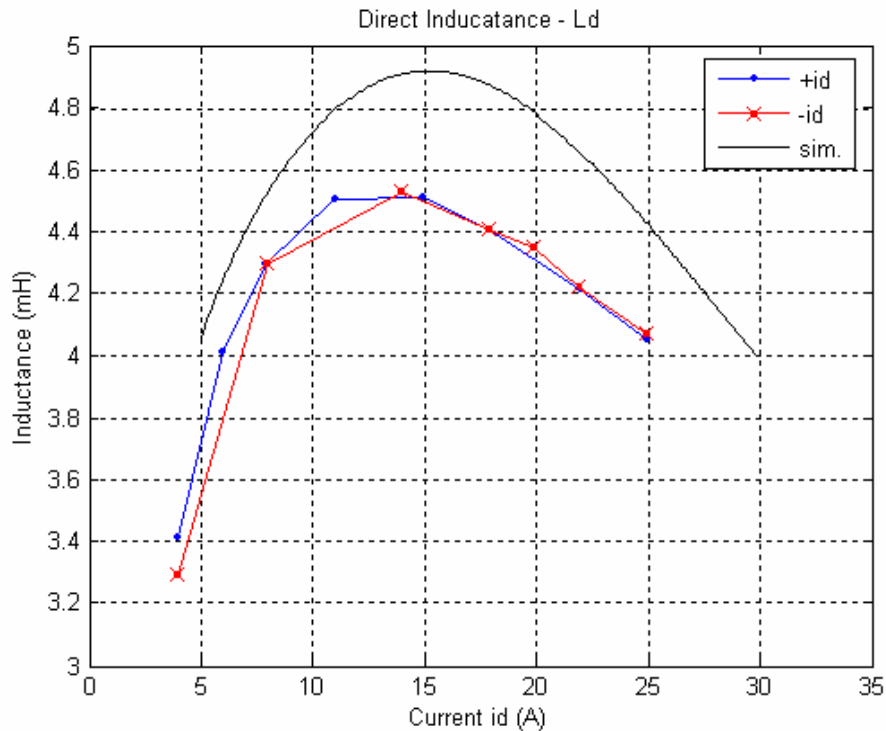


Figure 11-3: Test and Simulation Inductance for Machine in the Direct Axis

The iron loss for current applied in the direct axis is shown in Figure 11-4. At higher current, the simulations predict greater loss than the testing shows. The likely cause is the magnetic rotor steel is saturating at a lower flux density than in the simulation model. The iron loss may be higher at low currents due to the simulation coefficients that account for rotational loss being too low. Although, the more likely cause is the magnetic steel layers are retaining a residual magnetic field as will be described for the quadrature axis current tests.

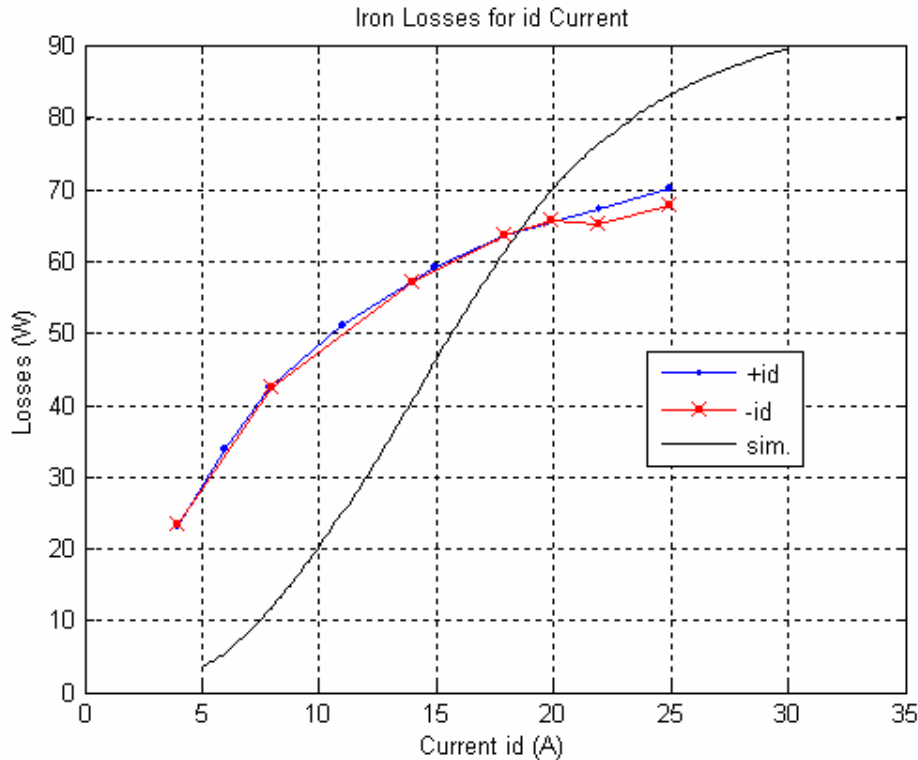


Figure 11-4: Test and Simulation Iron Loss for Machine in the Direct Axis

For the L_q inductance three different measuring methods plus the simulation value are shown in Figure 11-5. In the first method, the encoder is aligned exactly like it is for the direct inductance testing. Figure 11-6 shows that for this alignment the second machine's input power changes depending on the value of input current, i_q . The first machine is thus acting like a motor or generator depending on i_q current. The correct operation of the first machine is to contribute neither motoring nor generating power. Figure 11-6 shows how offsetting the encoder eliminates this motoring and generating. The reason this incorrect operation is occurring is the magnetic steel layers in the rotor are retaining a residual magnetic field similar to a permanent magnet. The machine thus acts like a permanent magnet machine when i_q current is applied and generating or motoring occurs.

To deal with the above problem L_q test are done with the encoder offset so that the input power to the second machine remains constant. This is done by shifting the encoder offset both clockwise (CW) and counter-clockwise (CCW). All three methods of measuring L_q result in 30-40% lower inductance values. It is possible the reason for this is the leakage inductance from the end turns is larger than the simulation value. Although, it appears more likely the residual magnetic field in the steel layers is the cause of the large discrepancy between testing and simulation.

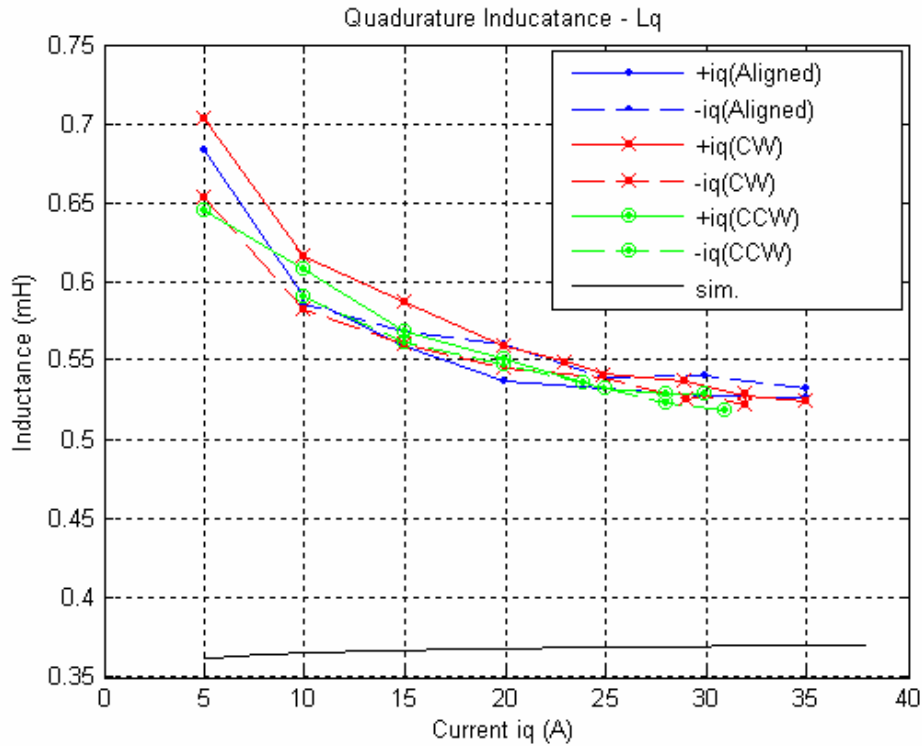


Figure 11-5: Test and Simulation Inductance for Machine in the Quadrature Axis

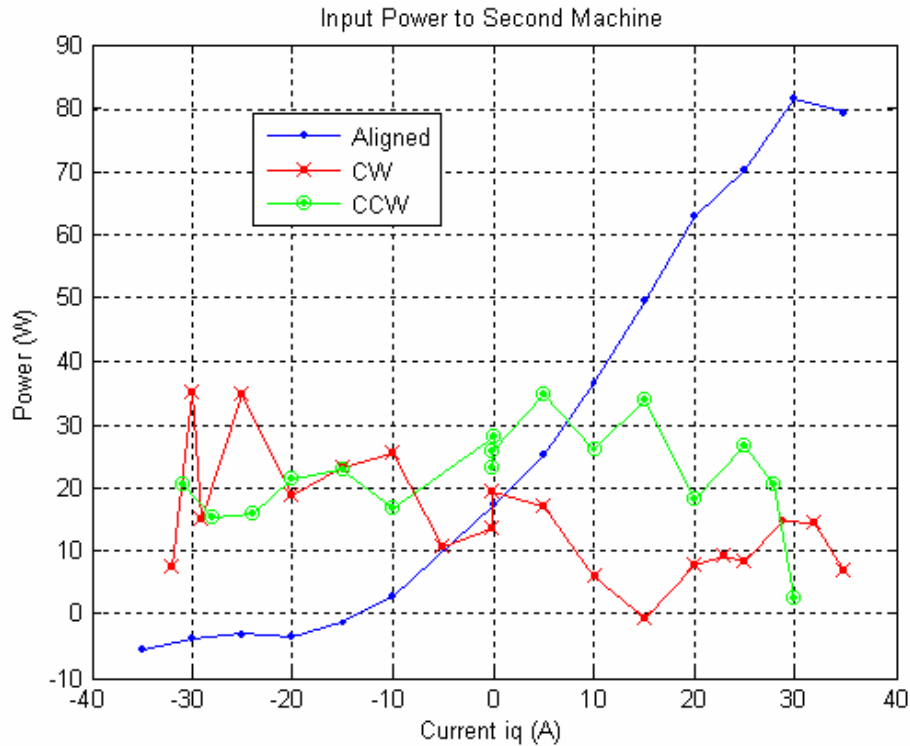


Figure 11-6: Input Power of Constant Speed Machine for Different Encoder Alignments

Further evidence of the residual magnetic field causing the discrepancy is found in the initial standstill inductance tests. In this test the magnetic field in the steel changes direction, and thus

the residual field cannot persist. If extrapolation of the standstill test is done to zero frequency, a value of about 0.34 mH is derived. This matches up fairly close to simulation and strongly indicates the residual magnetic field is causing the difference.

The residual magnet field also complicates the iron loss in the quadrature axis. The second machine's input power needs to be held constant to find the iron loss. This means only the shifted encoder values are used in Figure 11-7. The loss is considerably higher than what is predicted by simulation. The residual magnetic field is again causing the large difference.

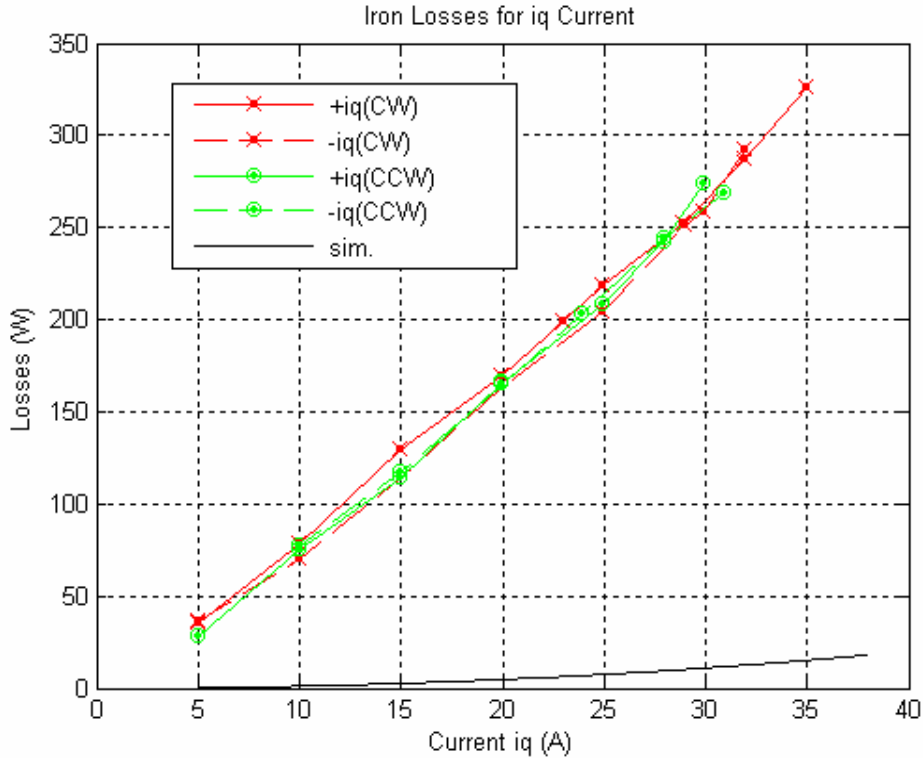


Figure 11-7: Test and Simulation Iron Loss for Machine in the Quaurature Axis

Figure 11-8 is a modified model of the small-scale machine. The model includes the residual magnetic field as the voltage source λ_{pm} (LAMpm). This voltage source increases the loss in the system. Its also complicates separating the iron loss in the model since the q axis test now has two voltage sources. More importantly, the residual flux varies greatly between tests depending on the angle and magnitude of previously applied currents.

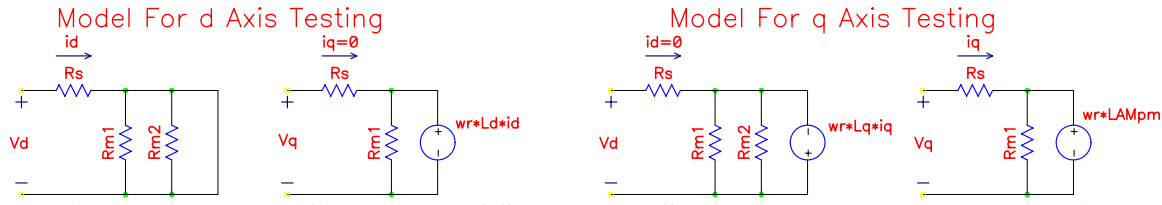


Figure 11-8: Modified Model of Small-scale Synchronous Reluctance Machine

Figures 11-9 to 11-14 show the loss of the combined machines and the input power of the first machine for various currents and rotation speeds. Plotted in dashed lines is the predicted loss and input power from simulations. The loss at low i_d is again much greater than in the simulations due to the residual magnet field. The loss is less at higher currents because of the

lower permeability of the rotor steel layers. The input power graphs further verify both of these conclusions since the power is higher at low i_d and lower at high i_d .

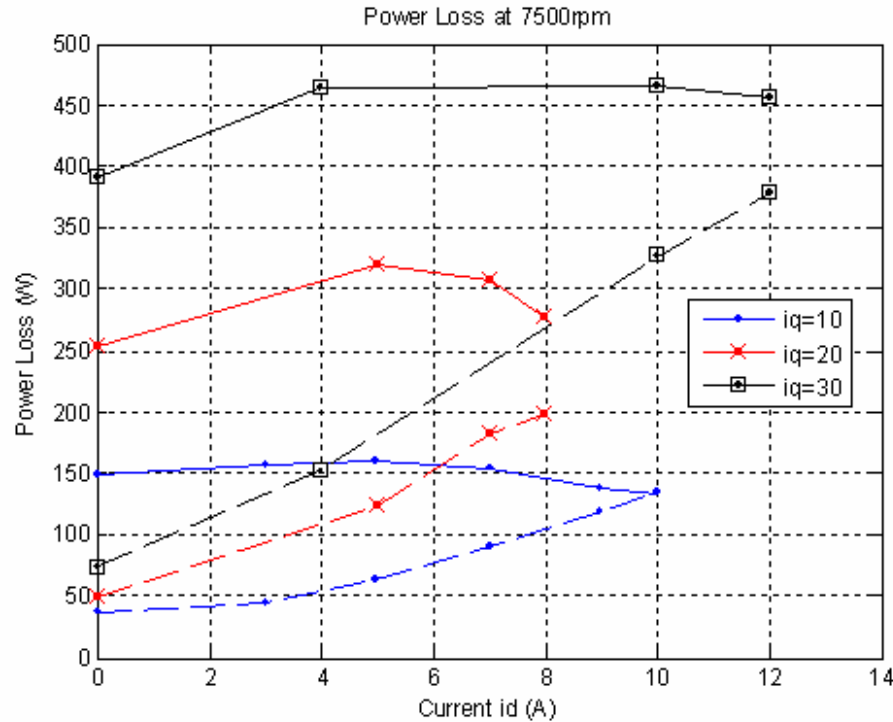


Figure 11-9: Test and Simulation Combined Power Loss for Both Machines at 7,500 rpm

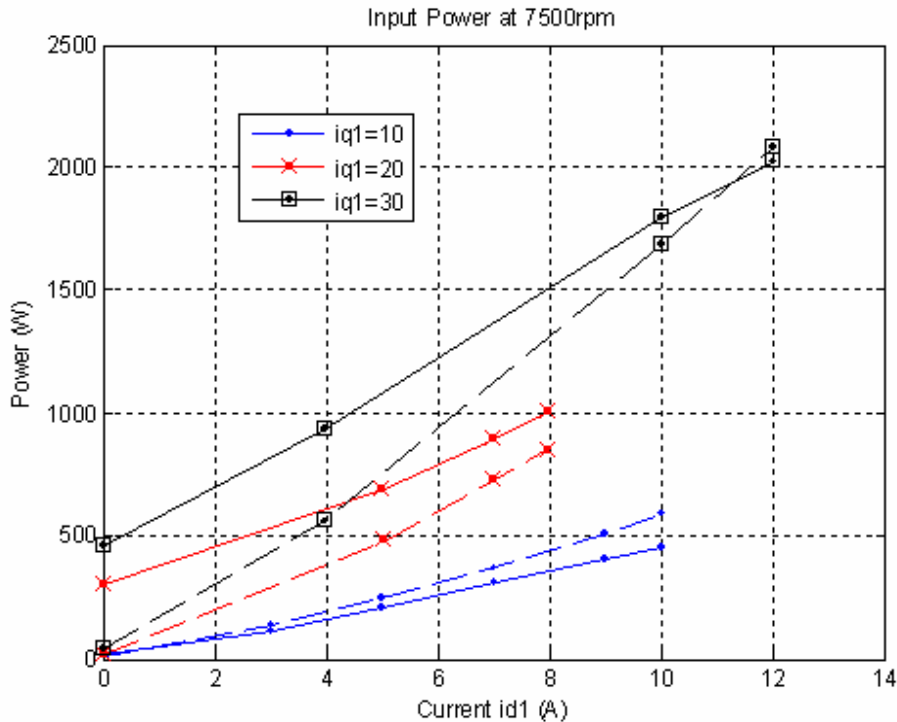


Figure 11-10: Test and Simulation Input Power for Constant Current Machine at 7,500 rpm

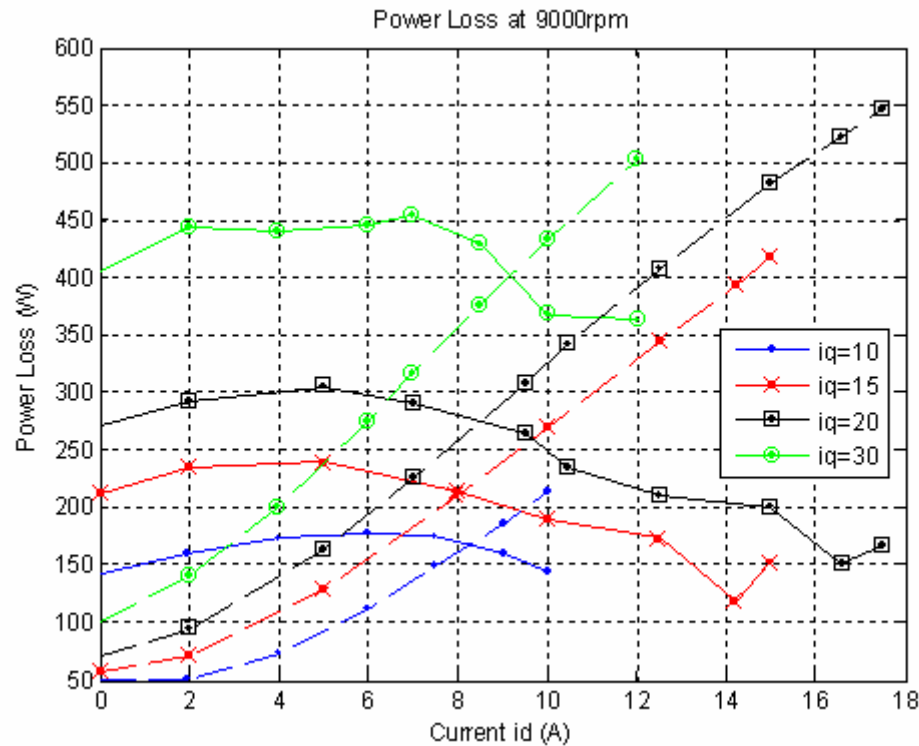


Figure 11-11: Test and Simulation Combined Power Loss for Both Machines at 9,000 rpm

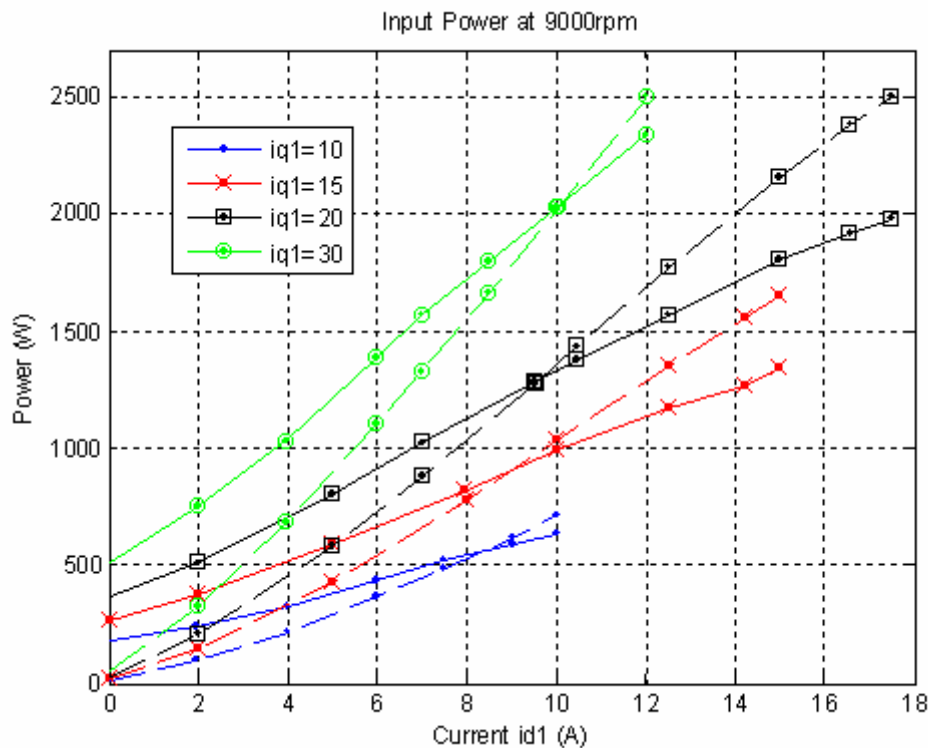


Figure 11-12: Test and Simulation Input Power for Constant Current Machine at 9,000 rpm

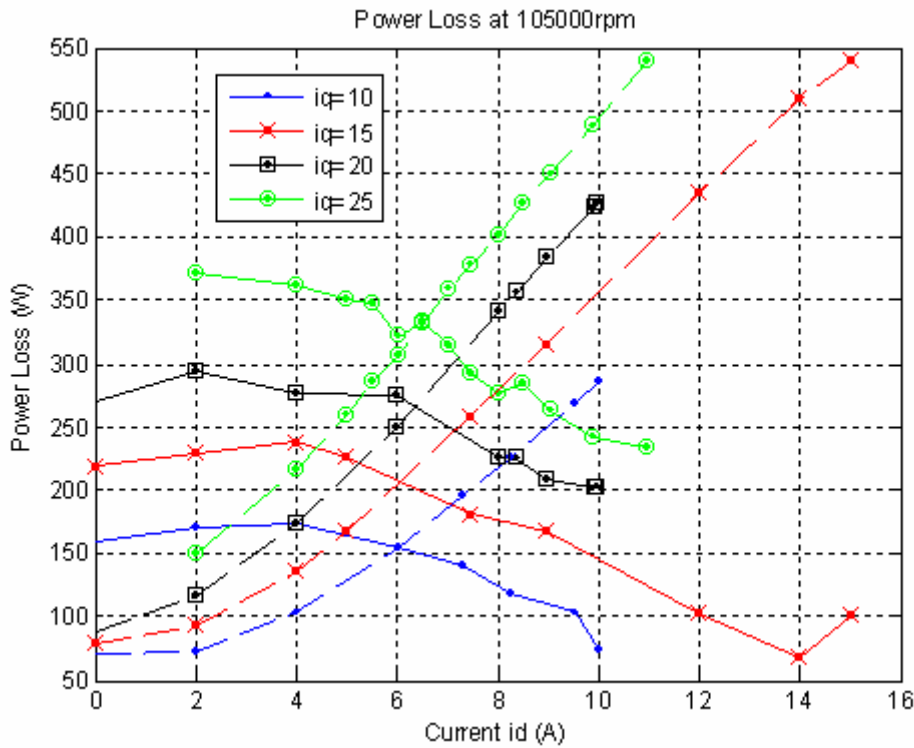


Figure 11-13: Test and Simulation Combined Power Loss for Both Machines at 10,500 rpm

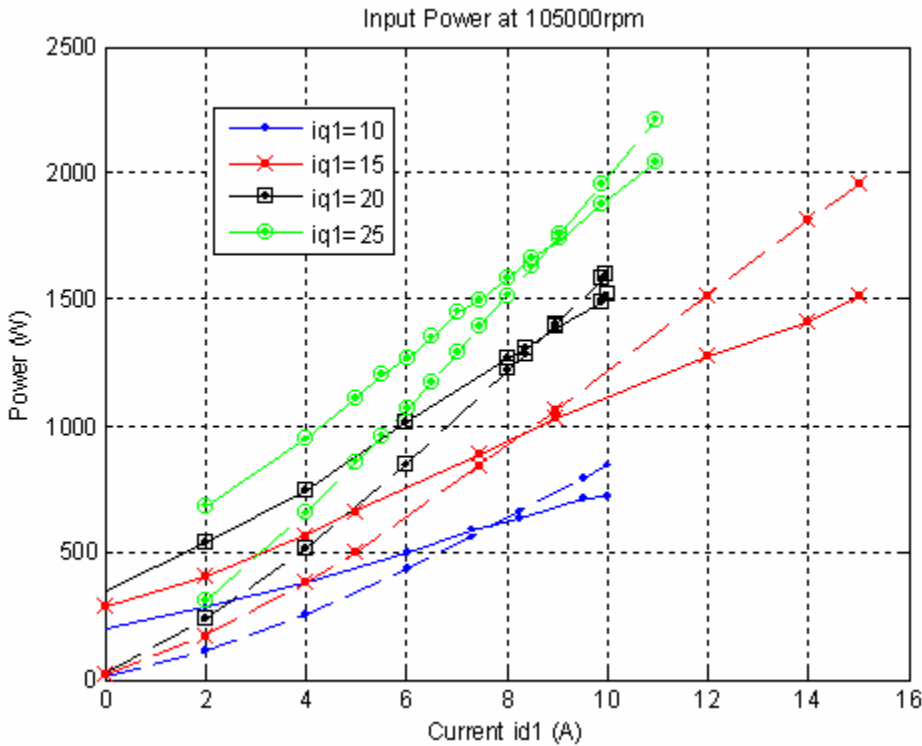


Figure 11-14: Test and Simulation Input Power for Constant Current Machine at 10,500 rpm

11.4 Rotor Loss

One of the goals of the testing was to derive the loss in the rotor. The procedure to find the rotor loss was to use an infrared thermal sensor to measure the temperature of the rotor shaft during operation. Temperature changes in the shaft could be used to derive a rough idea of the rotor loss.

This method did not work as well as expected for two reasons. The first is that the machine's bearing loss adds a significant amount of heat to the shaft. The temperature of the shaft changes more dependently on the speed of the machine and how long it maintains that speed than on current applied to the machine. The second reason is for ease in manufacturing the rotor was made with squared off edges as seen in Figure 9-4. These edges cause high windage loss as well as creating a good convection surface along the perimeter of the rotor. The majority of heat from rotor loss will leave the rotor at this convection surface rather than heating up the rotor and shaft. For these two reasons the shaft temperature will only rise if the rotor loss is large. During testing no such large temperature rises occurred.

While temperature sensing of the shaft is not as useful as desired, a couple of conclusions can be derived from it. The first is that it is unlikely the significantly increased loss at low i_d currents is taking place in the rotor. The second is that, while the rotor loss may be more than what is found in the simulations, it is probably not by a significant amount, or it would appear in the rotor temperature readings.

11.5 Conclusions From Test Results

The most important conclusion from testing is that the normal model for an axially laminated SYNREL is not valid if hot rolled steel is used for the rotor's magnetic layers. Instead a model is needed with the inclusion of a residual magnetic field in the d axis. This field increases the loss in the machine by a significant factor. The B-H curve for the hot rolled steel is also inferior to cold rolled steel due to a lower permability and lower saturation flux density. The combination of an inferior B-H curve and higher loss from the residual magnetic field makes the use of hot rolled steel unattractive for the full-scale machine.

No conclusion can be made about the iron loss in the rotor. The infrared temperature sensing was not able to find any thermal changes from applied current. The separation of rotor loss and stator loss is also not possible due to the residual magnetic field in the rotor layers. Instead, finite element transient simulations will need to be done to provide insight into rotor loss for the full-scale machine.

While the small-scale testing has not eliminated the axially laminated SYNREL from consideration, it has shown some definite problems. The requirement to use cold rolled steel presents a significant problem since it is only available in thin gauges. If thin gauge steel is used, the price of the machine goes up significantly since brazing needs to be done between each layer. In addition, the rotor shaft is a problem since its strength decreases significantly if it is composed of multiple layers instead of a solid piece.

12 Iron Loss Simulations

Classical equations for finding the iron loss in a synchronous machine are not practical for a SYNREL due to the complexity of the rotor geometry. Instead, the finite element method is used to find the flux density in the machine. If this method is used in a time stepping method, also

known as a transient simulation, the flux and current density in the machine can be used to find the iron loss. During the time stepping, the rotor or stator is moved by a prescribed angle to simulate the rotation speed of the machine. The calculation of the iron loss from transient simulations is done by one of three different methods.

The first method uses the ability of finite elements to calculate perpendicular current density, J_z , during transient simulations. This method is used only for the axially laminated rotor since its calculations are more time consuming. The machine is still only modeled in two dimensions (x and y axes), but the current density in the direction perpendicular to the modeled geometry (z axis) is calculated. The nodes of the materials for which the loss are calculated are coupled so that they are all at the same voltage potential. If certain areas are not shorted together due to electrical insulation, separately coupled sets are created. The coupling of voltage potentials simulates the effect of the areas being open circuited at the ends of the rotor.

The current density in the z axis is used to find the power loss per length for each element at a given sample n with the expression

$$\frac{P_e(n)}{\ell_{eddy}} = J_z^2(n) A_e \rho \quad (12-1),$$

where P_e is the power loss of the element in W, ℓ_{eddy} is the length of the eddy current path in m, ρ is the resistivity of the steel in $\Omega\text{-m}$, and A_e is the elements area in m^2 . Multiplying by the rotor length plus an extra factor for the end effects gives the power per element. All the elements using this method are then summed to find the total iron loss at that time step.

For this method, the iron loss needs to be summed for time steps spanning a 60 electrical degree span. Since J_z currents are not initially correct an extended settling time is needed before J_z becomes accurate. For this reason, the simulation is run for at least 120 electrical degrees and the last 60 electrical degrees are used to calculate the average rotor loss. The last 60 electrical degrees can be summed and divided by the number of time steps during this span to find the average iron loss for the parts using this first method.

The second method is used to find the eddy current loss in conventionally stamped laminations. The main harmonic frequencies in the part should penetrate the entire lamination. This method is suitable for the rotor since it typically has small hysteretic loss. In this method, the current sample for flux density in each element is subtracted from the previous sample. The following equation is used to find the power loss in the element:

$$P_e(n) = \left[\left(\frac{B_x(n) - B_x(n-1)}{\Delta t} \right)^2 + \left(\frac{B_y(n) - B_y(n-1)}{\Delta t} \right)^2 \right] \frac{A_e \ell_{rot} d_{lam}^2}{12 \rho} \quad (12-2),$$

where P_e is the loss in the element W, B_x and B_y are the flux densities in the x and y directions respectively in T, Δt is the time between simulations in sec, ℓ_{rot} is the length of the rotor in m, ρ is the rotor laminations' resistivity in $\Omega\text{-m}$, and d_{lam} is the thickness of the laminations in m. To find the total loss in a part, the power loss for all its elements are summed together.

In the second method, power loss is valid starting with the second simulation since the calculations are only based on flux density. Therefore, the number of simulations needed to find the average power loss in the part is 60 divided by the rotation angle increment plus one. The 60 electrical degrees represents the span for which the flux density is repeated in the rotor, and the plus one is to find an initial flux density. To find the average iron loss for the second method all

the simulations, except the first, are summed and divided by the total number of simulations minus one.

The third method calculates both eddy current and hysteretic loss for conventionally stamped laminations. The first step in this method is to find the harmonic components of the flux density in each element. This is done by sampling the flux density in the element for a 60 electrical degree span. In the rotor this span represents a complete cycle. For the stator, this only represents a sixth of a complete cycle. To obtain the rest of the cycle the stator is divided into three sections. The elements in each section are partitioned so that each section is identical. Each section's flux density results are calculated with an appropriate phase shift. The negative results of the flux density are also used with a 180 electrical degree phase shift. Figure 12-1 shows how the stator is segmented and the phase shift applied to each section. By using this method, a full 360 electrical degree span for the stator is calculated while only simulating a 60 electrical degree span.

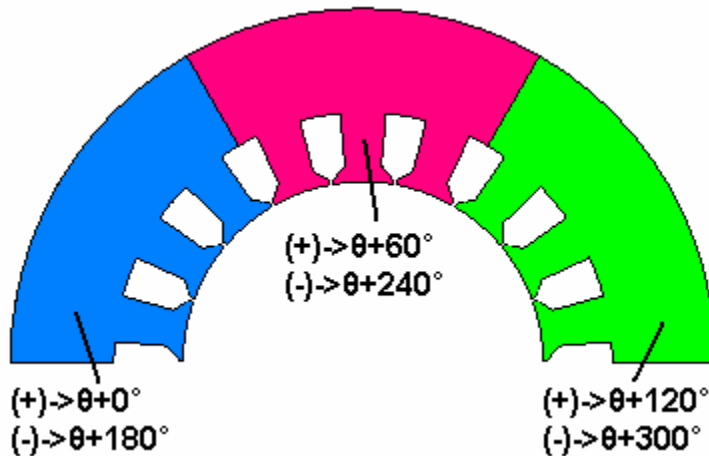


Figure 12-1: Stator Segmentation and Phase Shifting for Stator Iron Loss Calculations

The harmonics for the flux density are found using the Fourier transformation:

$$B_k = \frac{1}{N} \sum_{n=0}^{N-1} B_n(n) e^{-j2\pi kn} \quad \text{for } k=0,1,..,N-1 \quad (12-3),$$

where B_k is the flux density harmonics, B_n is the sampled flux density in the element, N are the number of samples for a period, and k is the order of the harmonic. The flux density harmonic results will look similar to the results shown in Figure 12-2. For the stator, each k harmonic is equal to a frequency

$$f_k = \frac{k \left(\frac{P}{2} \right) \Delta\theta}{360(\Delta t)} \quad (12-4),$$

where $\Delta\theta$ is the angle the stator is moved between simulations in degrees, P are the number of poles, and Δt is the simulation time step. The rotor is similar, but the frequency is six times faster

$$f_k = \frac{6k \left(\frac{P}{2} \right) \Delta\theta}{360(\Delta t)} \quad (12-5).$$

The flux density harmonics are found for both the x direction (B_x) and y direction (B_y) in each element.

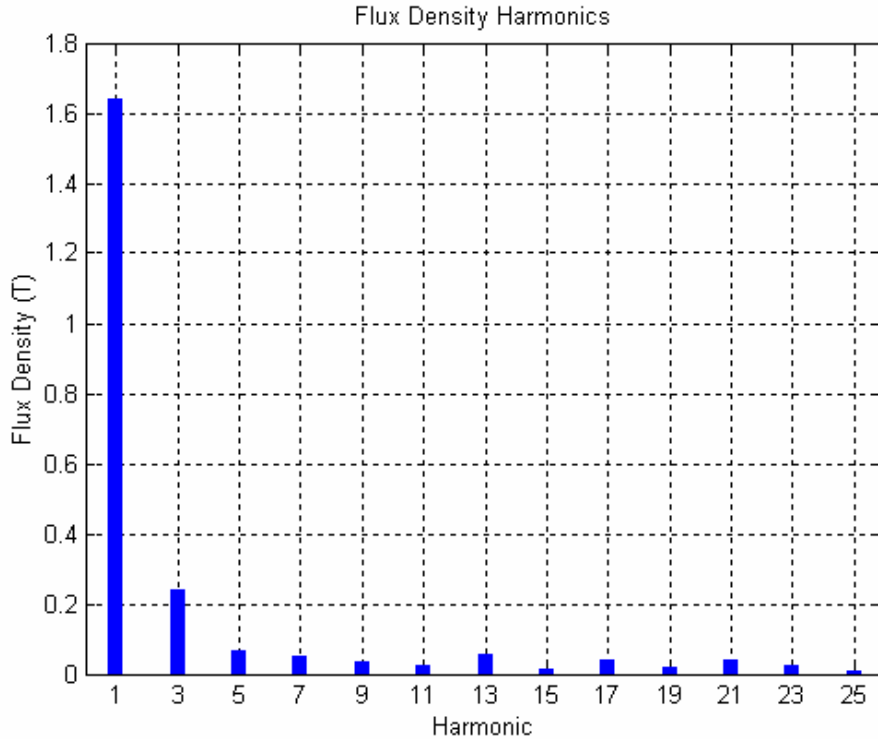


Figure 12-2: Example Flux Density Harmonic Results

If the flux density for an element is always in one vector orientation, the following equation can be used to calculate the iron loss:

$$B_s = \sqrt{B_x^2 + B_y^2}$$

$$P_e = \sum_{k=1}^{N-1} [k_{eddy}(kf)^2 B_s^2 + k_{hyst}(kf)^x B_s^y] A_e \ell_m \quad (12-6),$$

where P_e is the loss in the element in W, f is the frequency of the flux density in Hz, N are the number of samples, B_x and B_y are the peak flux densities for the x and y direction in T, A_e is the elements area in m^2 , ℓ_m is the length of the machine in m, and k is the order of the harmonic. The parameters k_{eddy} , k_{hyst} , x , and y depend on the type of steel being used. Table 12-1 shows these parameters derived from a curve fitting of Epstein tests done for M-15 29 gauge steel and M-19 steel 26 gauge steel [13]. While these results are valid for unidirectional flux density, a rotating machine usually sees flux density that changes orientation as rotation occurs. This rotating flux density can increase the iron loss significantly.

	Name in equation	M-15 29 gauge	M-19 26 gauge
Eddy current coefficient	k_{eddy}	0.4183	0.6679
Hysteresis coefficient	k_{hyst}	92.7595	64.4257
Hysteresis frequency exponent	x	2.15	2.16
Hysteresis flux density exponent	y	1.12	1.20

Table 12-1: Iron Loss Parameters Derived from Epstein Test Data

To account for the rotating flux density in an element, an additional factor δ is introduced. This additional factor takes into account the shape of the rotating flux density. Figure 12-3 shows three different plots of variation in flux density over an entire electrical cycle. How elliptical these plots are determine the value of δ . Taking the flux density short axis divided by the long axis yields

$$\delta = \frac{B_{sh}}{B_{lg}} \quad (12-7).$$

Figure 12-3(a) shows a case where $\delta=0$ and no extra rotational loss factor is needed. Figure 12-3(b) and (c) show the cases where δ equals 0.5 and 1.0 respectively.

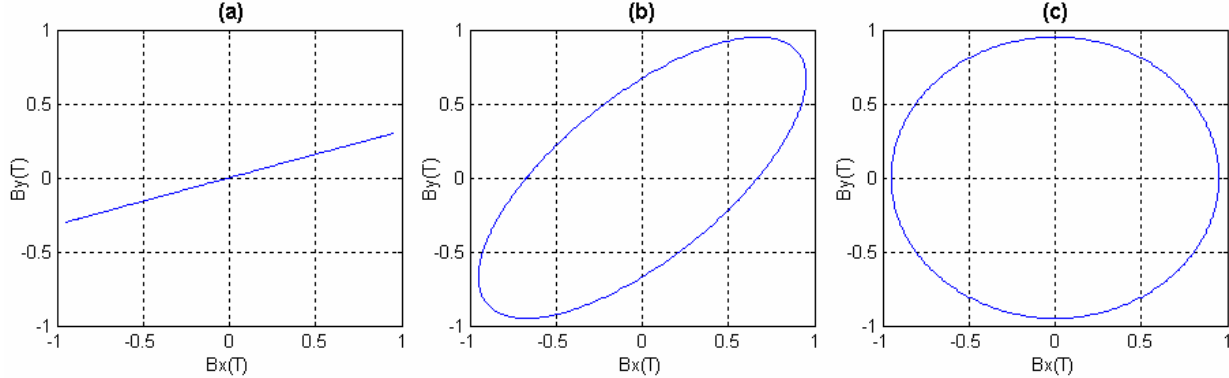


Figure 12-3: Example Flux Density Variation Over a Cycle (a) $y=0$ (b) $y=0.5$ (c) $y=1.0$

While it is easy to find the flux densities for the long and short axis of Figure 12-3(c), it is not so obvious how to find these values for Figure 12-3(b). To find these axis values, the following transformation is used:

$$\begin{aligned} \Phi_s &= \frac{1}{2} \arctan \left(-\frac{B_x^2 \sin(2\theta_x) + B_y^2 \sin(2\theta_y)}{B_x^2 \cos(2\theta_x) + B_y^2 \cos(2\theta_y)} \right) \\ B_u &= \sqrt{(B_x \cos(\Phi_s + \theta_x))^2 + (B_y \cos(\Phi_s + \theta_y))^2} \\ B_v &= \sqrt{(B_x \cos(\Phi_s + \theta_x + 90))^2 + (B_y \cos(\Phi_s + \theta_y + 90))^2} \\ B_{lg} &= \max(B_u, B_v), \quad B_{sh} = \min(B_u, B_v) \end{aligned} \quad (12-8),$$

where B_x and B_y are the peak flux densities for the x and y direction, θ_x and θ_y are the phase of the flux densities for the x and y direction in degrees, and B_{lg} and B_{sh} are the peak long and short axis flux densities.

To incorporate the rotational factor δ into the iron loss expression, an additional factor γ based on the fundamental flux density is needed [14]. The γ factor is large at low flux densities but decreases as the flux density in the material approaches saturation. For the materials in Table 9-1, the following expression is used for γ :

$$\begin{aligned} \gamma &= 2 && \text{for } B_{lg} < 0.4 \\ \gamma &= (-1.8182)B_{lg} + 2.7273 && \text{for } 0.4 \leq B_{lg} \leq 1.5 \\ \gamma &= 0 && \text{for } 1.5 < B_{lg} \end{aligned} \quad (12-9),$$

where B_{lg} is the fundamental harmonic's peak flux density along the long axis. For the stator, the fundamental flux density is determined by the first harmonic, which has a frequency equal to the electrical rotation rate in the machine. For the rotor, the zero harmonic component is used since it is the fundamental frequency.

The new equation for the iron loss, which accounts for rotational loss in the material, is

$$P_e = \sum_{k=1}^{N-1} [k_{eddy}(kf)^2 B_{lg}^2 + k_{hyst}(kf)^x B_{lg}^y] A_e \ell_m (1 + \gamma\delta) \quad (12-10),$$

where P_e is the loss in the element, N are the number of samples, B_{sh} and B_{lg} are the short and long peak flux densities, A_e is the elements area, ℓ_m is the length of the machine, k is the order of the harmonic, and

$$\delta = \frac{B_{sh}}{B_{lg}} \quad (12-11).$$

This expression accounts for eddy current loss, hysteric loss, and rotational loss. In addition, the γ factor accounts for decreased rotational loss in the material near saturation. This calculation is done for all the elements in a part and the results are summed to find the total iron loss.

Figure 12-4 and 12-5 show examples of loss for a stator and a rotor respectively. Because the electrical cycle repeats every 60 degrees in the rotor, the harmonics in Figure 12-5 are six times those of the stator. For this span, the stator also takes six times the number of samples than the rotor, and therefore more harmonics can be calculated for it.

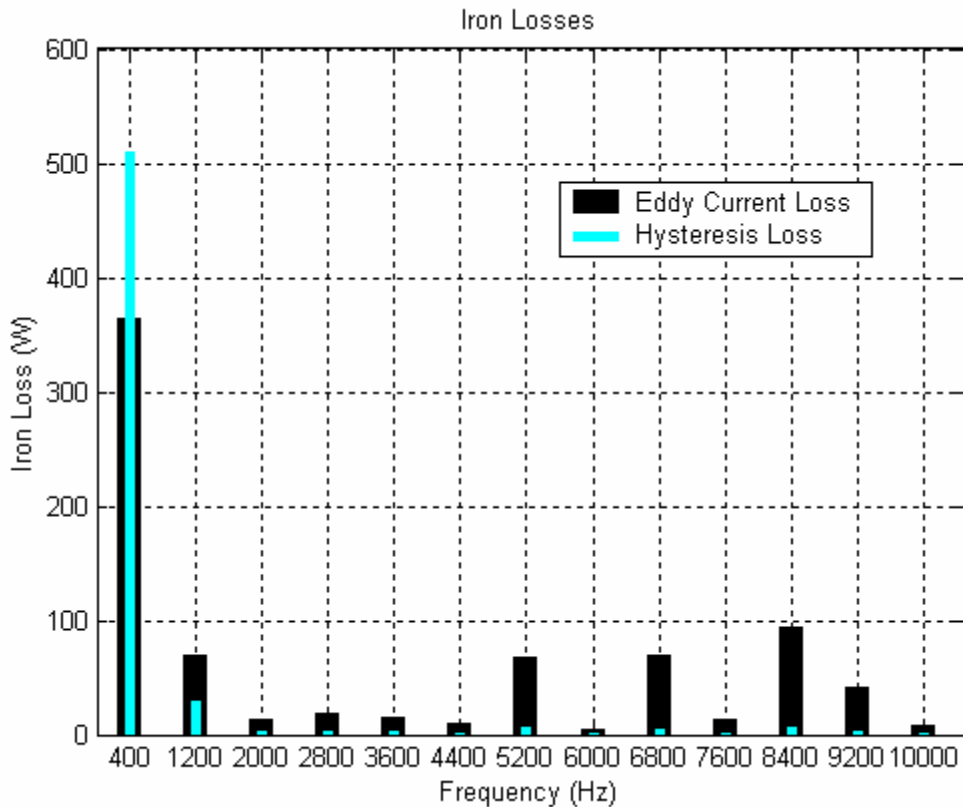


Figure 12-4: Example Stator Iron Loss Harmonics

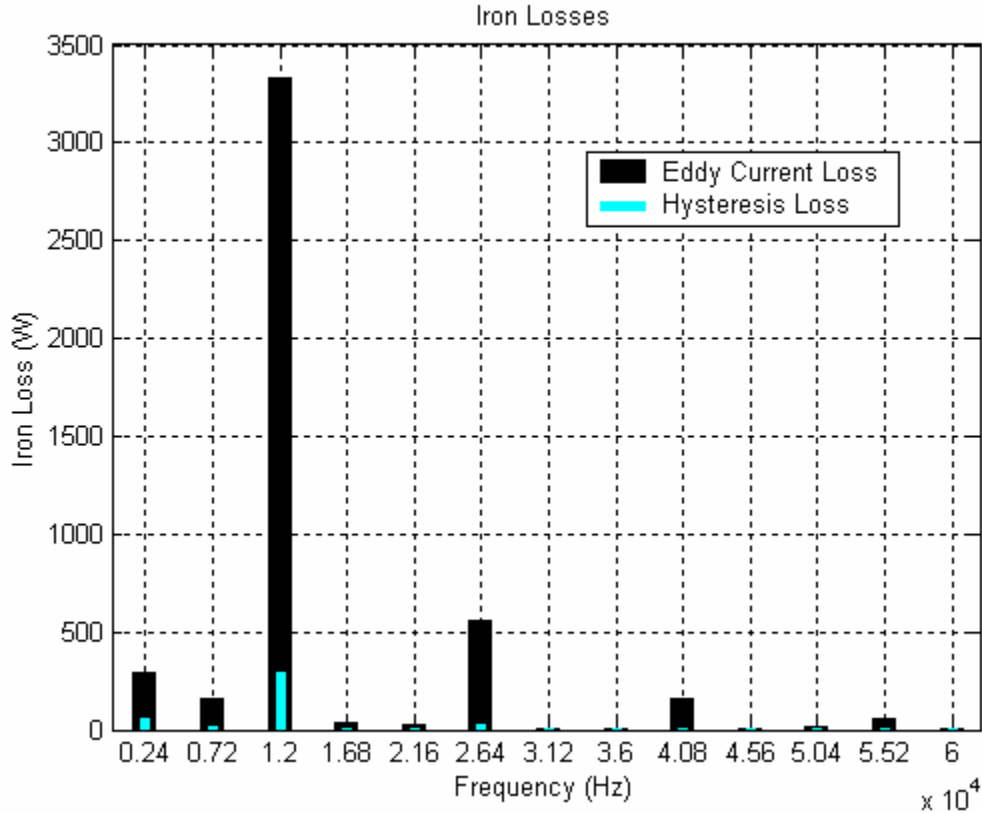


Figure 12-5: Example Rotor Iron Loss Harmonics

For the small-scale simulation results found in Section 11, the third method is used for the stator, and the first method is used for the rotor due to the axially laminated layers. The first method is also used for the full-scale axially laminated rotors in Section 14.2. For the stators in Section 14 and the conventionally laminated rotors in Section 14.3 and 14.4, the third method is used. The second method is also used on the conventionally laminated rotors in Section 14 and shows similar eddy current loss. However, the third method adds in the effects of hysteric and rotational loss and is more accurate.

13 Thermal Simulations

One of the main goals is to design the full-scale motor/generator so it is able to operate in a vacuum. Simulations are needed to determine if the rotor loss is low enough to prevent damaging the rotor. This is accomplished with the use of thermal finite element simulations.

Figure 13-1 shows how the thermal simulation problem is defined. The inner flat edged circle, labeled A and B, represents the rotor for a two-pole machine. A constant heat generation source is defined for the circular edge, labeled B. The heat generation represents the iron loss that occurs in the rotor. This loss is located on the edge since the majority of the rotor loss occurs here.

The portion labeled C represents the gap between the rotor and the stator. This region is modeled as a material for a non-vacuum or deleted in the case of a vacuum. The outside periphery of area C is assigned a radiation coefficient based on the stator material. In the same way, the inside periphery is assigned a radiation coefficient for the rotor material.

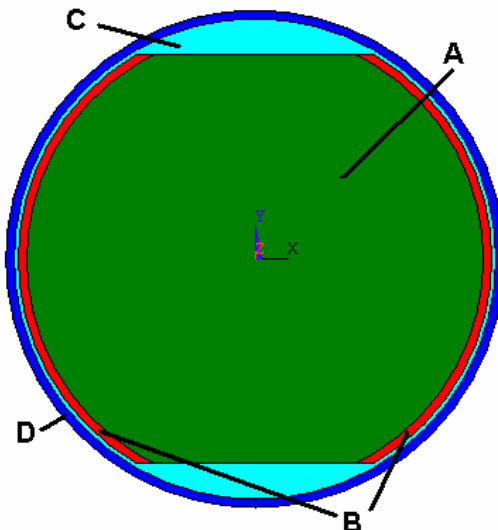


Figure 13-1: Thermal Simulation Geometry

The outer circle, labeled D, represents the stator. The outer portion of this ring is prescribed a boundary condition so that it is held at a constant temperature. This represents a rough estimate of liquid cooling in the stator slots. In certain cases, the high thermal conductivity of copper also makes it a really rough estimate for end turn type cooling.

The material properties of thermal conductivity, density, and specific heat need to be defined for each area in the thermal simulations. The basic model may also be changed to a full circle for the four-pole machine described in Section 14.4.

The two types of thermal simulations run are static and transient. The static simulation is used to find the temperature of the rotor for a given continuous power loss in the rotor. This type of simulation also calculates the amount of heat that is transferable from the rotor for a given rotor temperature.

Transient simulations calculate the temperature of the rotor as it varies with time. The first way to use transient simulations is to find the temperature change versus time in the rotor for a given rotor loss. If the loss in the rotor is set to zero, the transient simulation is also able to calculate how long it takes the rotor to cool to a usable temperature. This last type of simulation is especially useful if the flywheel battery is used in an application where it runs at maximum power and then is allowed to cool before being used again.

14 Redesign of the Full-scale Motor/Generator

Testing of the small-scale machine displays a clear problem with the use of an axially laminated rotor using hot rolled carbon steel. The use of cold rolled carbon steel or silicon steel could fix the problems found in testing. Currently, only thin gauges are commonly available for either of these types of steel, and this will result in expensive manufacturing costs and problems with the rotor shaft. The first set of full-scale simulations assumes that thicker cold rolled carbon steel and silicon steel are available.

Further structural investigation suggests that a larger rotor diameter can be used than in the initial full-scale design. This increase is due to the braze joints between layers being able to withstand greater stress than the previous limit. The rotor diameter is increased to 14 inches and the

magnetic length is decreased to 26 inches. The larger diameter will increase the performance needed from the magnetic bearings for a given stator to rotor gap. For this reason, the gap is increased to 0.125 inches. In addition, the inverter has been changed to a dc-bus voltage of 1800 V and a current rating of 1400 Arms.

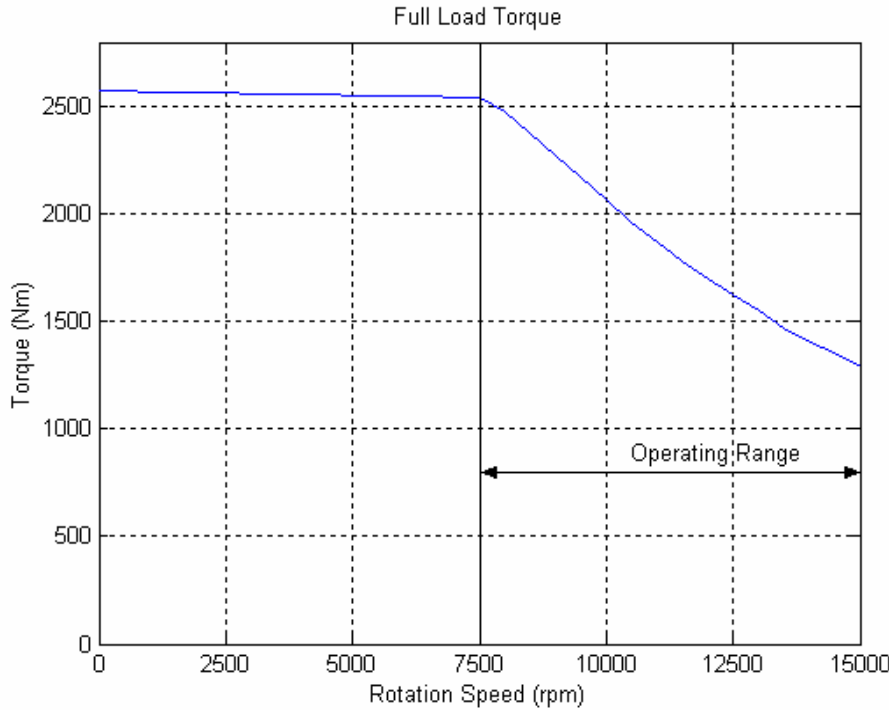


Figure 14-1: Simulation of Full-load Torque for Revised Axially Laminated Full-scale

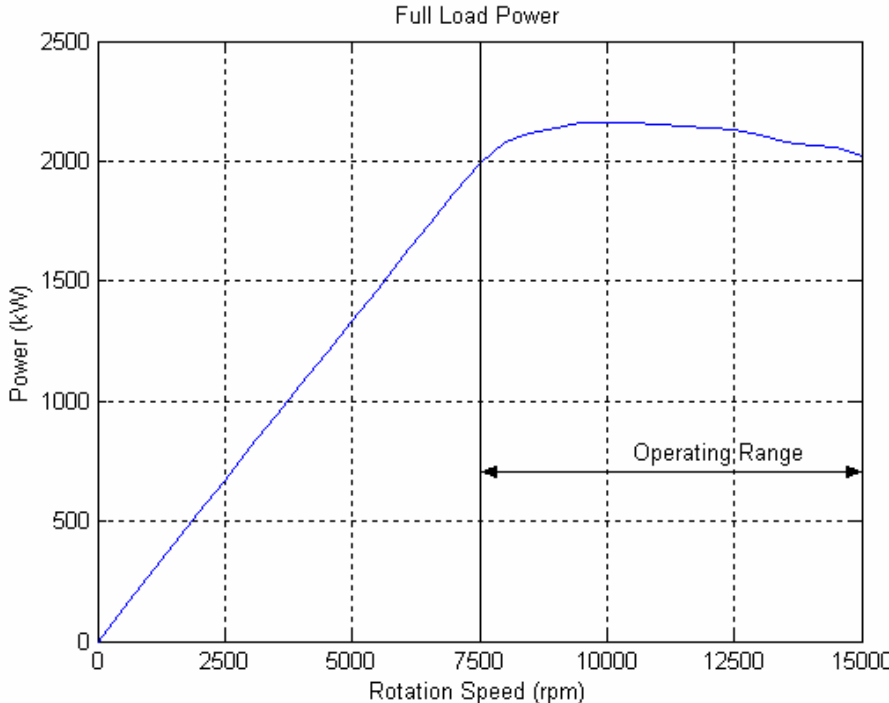


Figure 14-2: Simulation of Full-load Power for Revised Axially Laminated Full-scale

Figure 14-1 and 14-2 show the new full-load torque and power plots for the machine. The axially laminated rotor will be investigated to see if it will work in a vacuum. The amount of rotor loss this type of rotor can withstand will first be found with thermal analysis.

14.1 Base Case Thermal Analysis

The dimensions of the thermal simulation defined in Figure 13-1 are a rotor diameter of 14 inches, a length of 26 inches, and an air gap of 0.125 inches. The outer stator ring is assumed to have a thickness of 0.25 inches and the outside periphery is defined as being held at a temperature of 100°C.

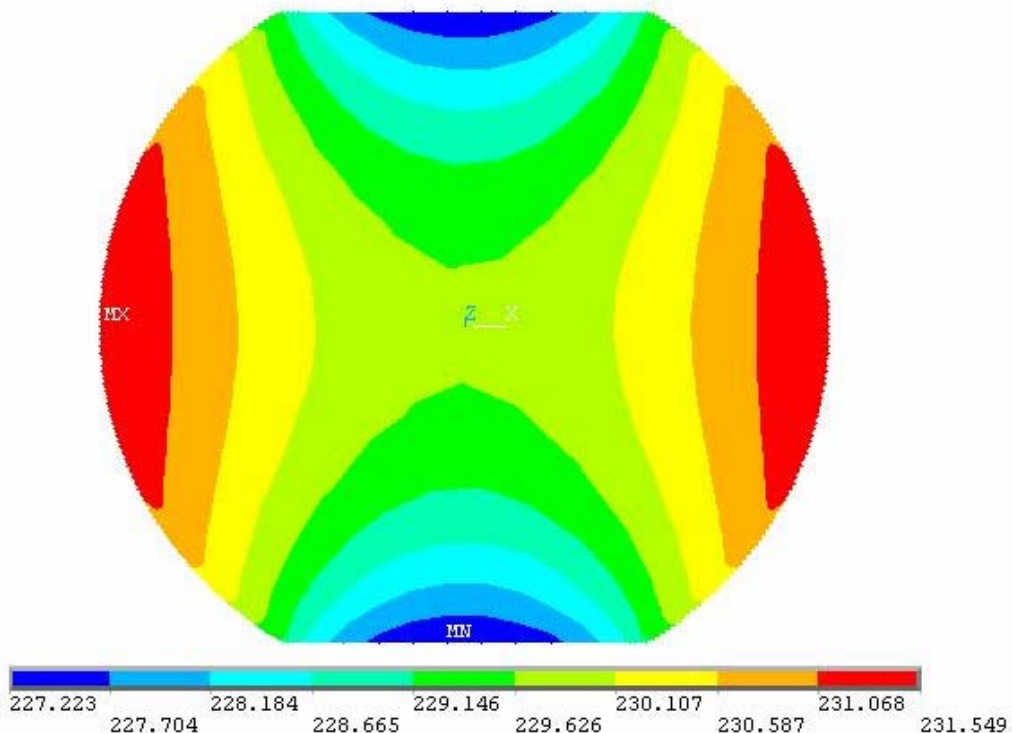


Figure 14-3: Example of Temperature Distribution from Thermal Simulations

Figure 14-4 shows how the temperature of the rotor changes with time for different power loss in the rotor. The emissivity in this case is set to 0.6 for the stator and 0.88 for the rotor. The higher rotor emissivity assumes that the rotor is coated with either a black paint or lacquer. As can be seen in Figure 14-4, the rotor has a fairly large heat capacity and takes a long time to heat up.

Figure 14-5 shows how the continuous rotor loss changes the continuous temperature of the rotor. Figure 14-5 can also be used to determine how much heat transfers across the rotor to stator gap. The amount of heat transferring is determined by the power loss at a given rotor temperature.

Figure 14-6 is generated with no loss in the rotor and a starting temperature of 250°C throughout the rotor. Due to the high heat capacity of the rotor and the amount of heat transferring across the gap, it takes a considerable amount of time for the rotor to cool down. Two different stator emissivity plots are shown corresponding to a black painted stator, and a stator that has not been coated. From these plots, it is obvious the painting surfaces black for higher emissivity is worth the extra cost.

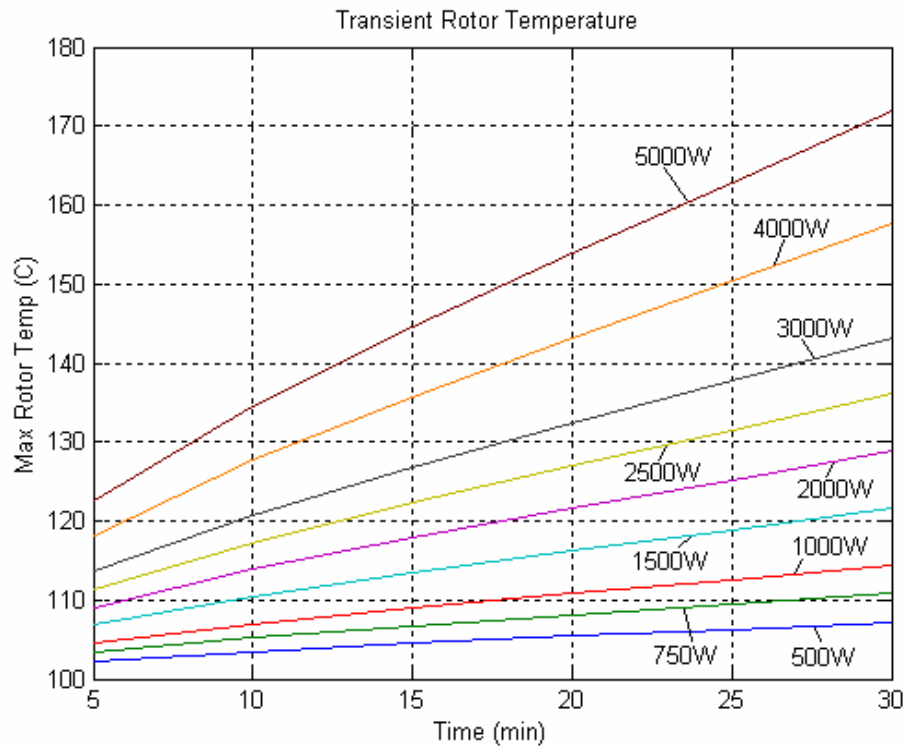


Figure 14-4: Transient Rotor Temperature Simulations with Rotor Emissivity of 0.88 and Stator Emissivity of 0.6

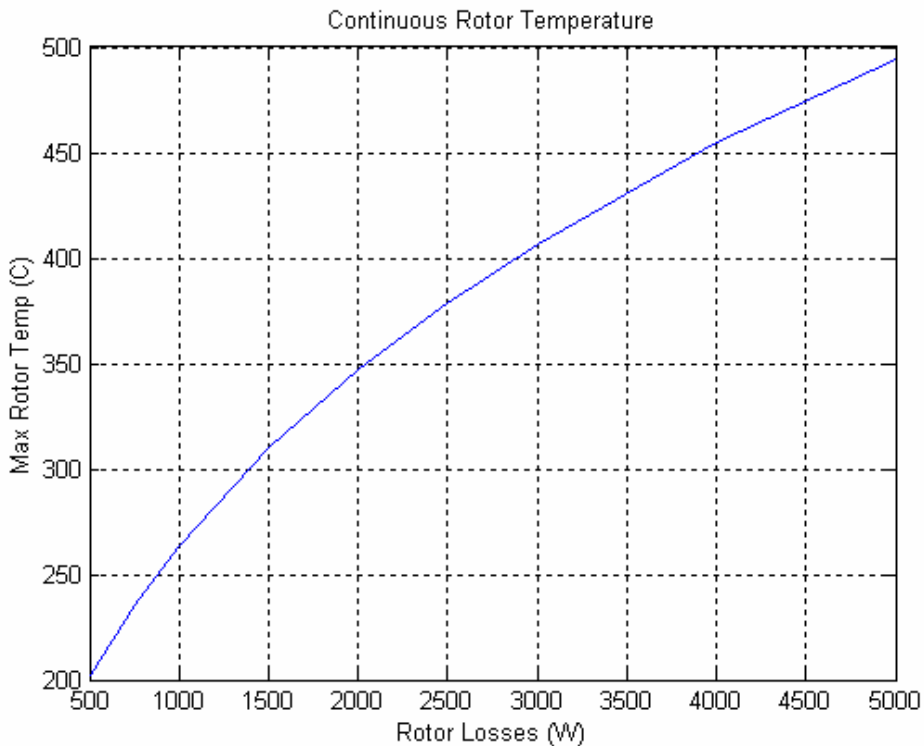


Figure 14-5: Continuous Rotor Temperature Simulations with Rotor Emissivity of 0.88 and Stator Emissivity of 0.6

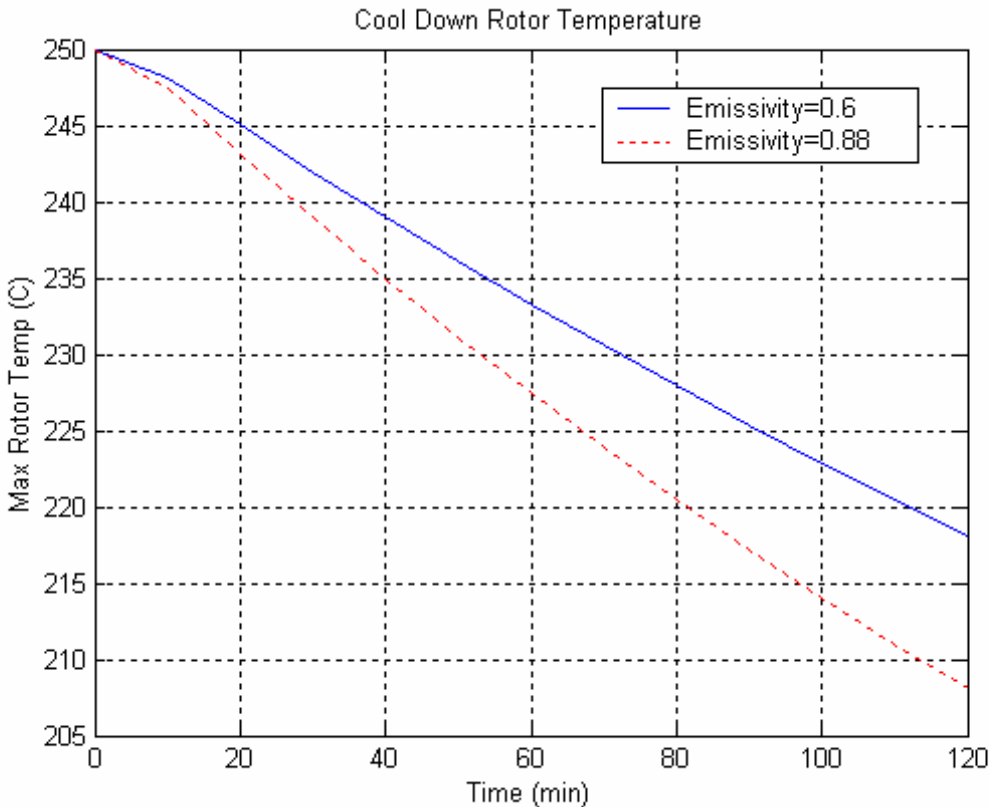


Figure 14-6: Zero Power Loss Cool Down in Rotor with Rotor Emissivity of 0.88 and different Stator Emissivities

While the above shows that the rotor takes fairly long to heat up, it takes even longer for it to cool down. This type of operation is acceptable if the application runs for short periods, and then idles for a moderate amount of time. For most applications, the desired operation will be to operate for longer times and withstand higher operating power loss.

One possible way to do this, without significantly increasing windage loss, is to use hydrogen in the enclosure. Slight modifications to the thermal simulation are needed to model hydrogen. The gap between the rotor and stator, which was previously deleted, is now modeled as a conductive material. The conductivity of the gap is modeled with a conductance of 0.1816 W/(m·°C). If more cooling is needed, the conductivity of the hydrogen can be increased by changing the pressure of the hydrogen gas. The ability to change hydrogen's thermal conductivity is useful since the windage loss changes inversely to the conductivity. It is therefore possible to reduce windage loss at low loading of the motor/generator, while still being able to operate continuously at high loads. Convection due to rotation is not included in the thermal analysis, but it would further increase the allowable power loss.

Figure 14-7 and 14-8 show a comparison of the hydrogen and vacuum conditions for both continuous power and cool down. The figures show that using hydrogen significantly increases the amount of loss the rotor can handle and decreases the time it takes to cool the rotor. The speed of the cooling is increased in large part due to no longer being mainly dependent on the cubic of the temperature difference.

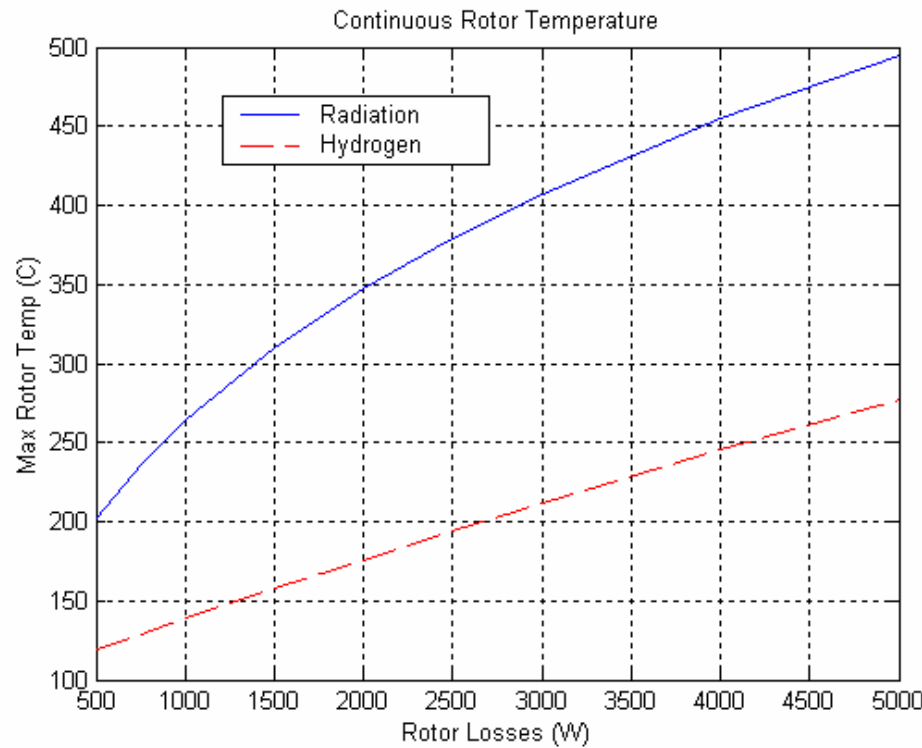


Figure 14-7: Comparison of Continuous Temperature for Hydrogen and Vacuum Environments

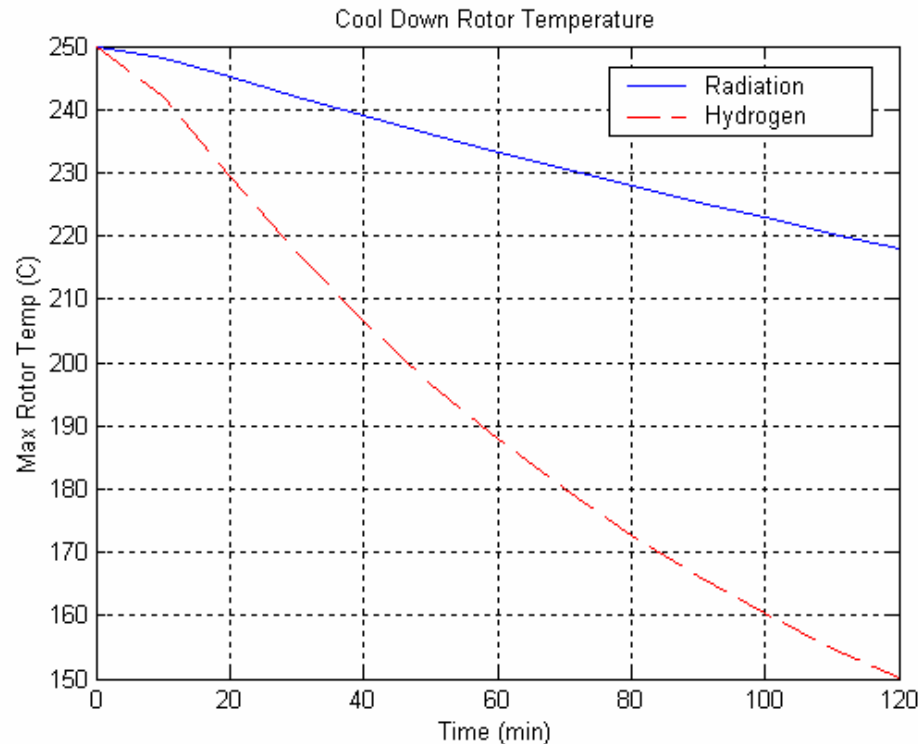


Figure 14-8: Comparison of Zero Power Loss Cool Down for Hydrogen and Vacuum Environments

The maximum temperature the rotor will be held at is most likely around 250°C. This means for a vacuum, the continuous rotor loss can be up to 872 W. For hydrogen, this will be significantly higher with an allowable loss of greater than 4,140 W.

14.2 Axially Laminated Rotor

The previously defined machine is run through transient simulations to find the rotor's iron loss, and see if they are within the thermal limits. The analysis is done at full-load power for rotation rates of 7,500 rpm, 12,000 rpm, and 15,000 rpm. The i_d and i_q currents for each of the conditions are calculated from the previous analysis. The rotor in this first set of simulations uses seven layers and is modeled as cold rolled AI-4140 steel.

For the first simulation at 7,500 rpm, the dc flux density is at maximum. This however does not mean the harmonics are high. From the simulation a total loss of approximately 61 kW is found in the rotor. Simulations are also run for 12,000 rpm and 15,000 rpm, and the results are loss of approximately 121 kW and 153 kW respectively. While the dc flux densities in the rotor are less for both these rotation rates, the harmonics increase significantly and thus the loss. The losses are obviously much greater than what was expected during the initial design.

Since the loss in the rotor is too high, some modifications are made to the rotor in an attempt to decrease the loss. For these modifications, the length of the machine and the stator geometry are modified for an equivalent full-load power curve. The geometry modifications for these machines will not be covered in detail since they are significantly different from the first design.

The first modification is to use the same rotor steel but to use more magnetic layers. The number of magnetic layers is increased to eleven. This results in loss of approximately 45 kW at 7,500 rpm. The increase in magnetic layers does not dramatically reduce the iron loss in the rotor. In addition, increasing the number of layers increases the cost of the rotor due to increased brazing surfaces. Even for this moderately large number of magnetic layers, there will be problems with the shaft since it will be segmented into at least three layers. While increasing the magnetic layers does decrease the iron loss, it is not effective enough to make up for the disadvantages.

The second modification is to change the magnetic layers to silicon steel. For this modification, the number of slots is reduced so that the i_d and i_q currents are somewhat similar to the previous simulation. The results for this simulation are still approximately 47 kW at 7,500 rpm. While the loss is again reduced by this modification, the improvement is only marginal. When this marginal gain is combined with the problems of silicon steel being damaged from high brazing temperatures and the probable high cost of thick sheet silicon steel, it seems unlikely that this is a realistic solution for lowering the iron loss.

It does not appear that the axially laminated rotor is able to operate in a vacuum or hydrogen enclosure. An additional modification that can be made is to machine slits in the rotor as in Figure 14-9. This adds extra length to the eddy current paths and thus increases the rotor resistance and decreases the iron loss. However, this process increases cost, decreases mechanical strength, and requires lengthening of the machine. As an example, to decrease the loss by 50%, the eddy current path has to be doubled. This would require a large amount of machining, since the rotor is 26 inches long, and the resulting decrease still results in approximately 76.5 kW of loss at 15,000 rpm.

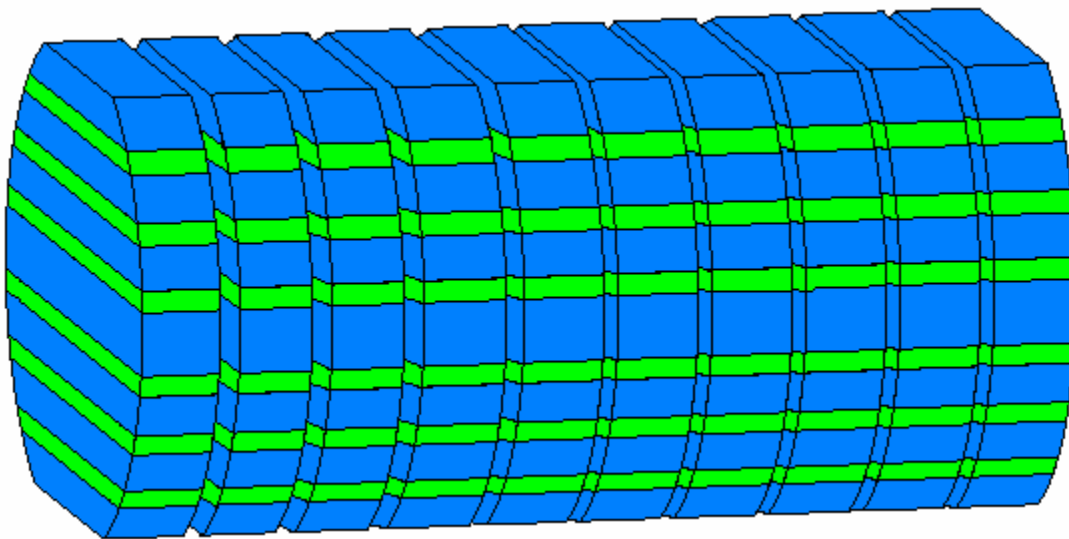


Figure 14-9: Slitting of Rotor to Reduce Iron Loss

From the above factors, it does not appear that an axially laminated rotor in any form is capable of low enough rotor loss for either a vacuum or in hydrogen. A conventionally laminated rotor will be examined to see if it can meet the required low rotor loss.

14.3 Conventionally Laminated Rotor

The conventionally laminated rotor consists of rotor laminations that are stamped in a pattern and stacked together. Bridges, like those in Figure 14-10, are included to allow the laminations to withstand the structural stresses from high rotation speed. These bridges decrease the L_d/L_q ratio of the machine. The reason the axially laminated rotor has such a high L_d/L_q ratio is that it has none of these bridges. It is therefore desirable to make these bridges as thin as possible, while keeping them thick enough that the lamination is not overstressed.

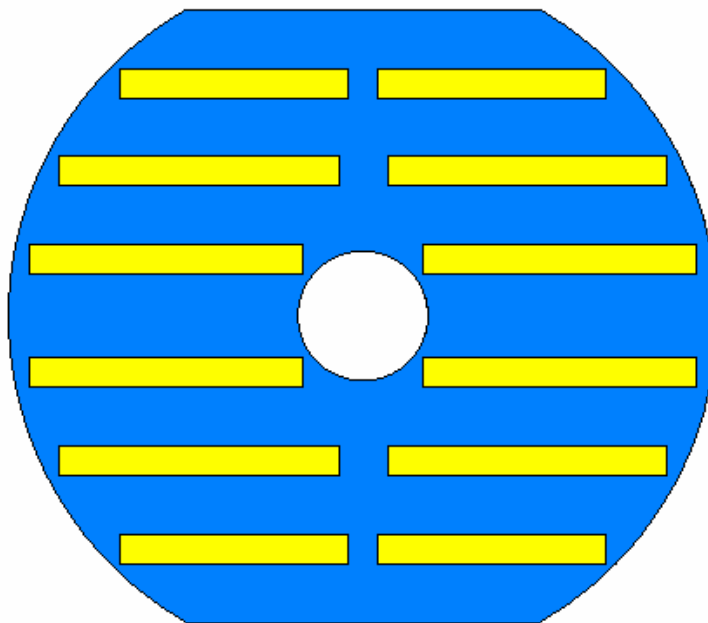


Figure 14-10: Conventionally Laminated Two-pole Rotor with Saturable Bridges

Figure 14-10 shows a cross-section of a two-pole conventionally laminated rotor. One problem with this rotor is how to incorporate a shaft. Due to the high rotation speed, a minimum of a 2.0 inch diameter shaft is needed. If the shaft is made from nonmagnetic steel, a problem is created since a large air gap is located in the center of the machine. The lowest reluctance path is suppose to pass through the center of the machine, but the introduction of the high reluctance air gap does not allow this to happen.

Since the large air gap eliminates the nonmagnetic shaft, a magnetic shaft instead needs to be used. A magnetic shaft of 2.0 inches will act as a magnetic bridge between the magnetic layers. The shaft and surrounding steel thus has the effect of significantly decreasing the L_d/L_q ratio of the motor. For one such design the L_d/L_q ratio at maximum is just under four. Due to this low ratio the two-pole conventionally laminated rotor does not seem to be practical.

A four-pole machine like the one in Figure 14-11 is considered instead. In such a design, there is plenty of room for a shaft to be located in the center of the machine. A four-pole machine consists of four sections of curved layers and an inner spider. The layers and spider are connected with saturable bridges. It is again desirable for these bridges to be small so that they saturate at low phase current. The radius of curvature for the pole layers is determined by the amount of flux traveling through each pole.

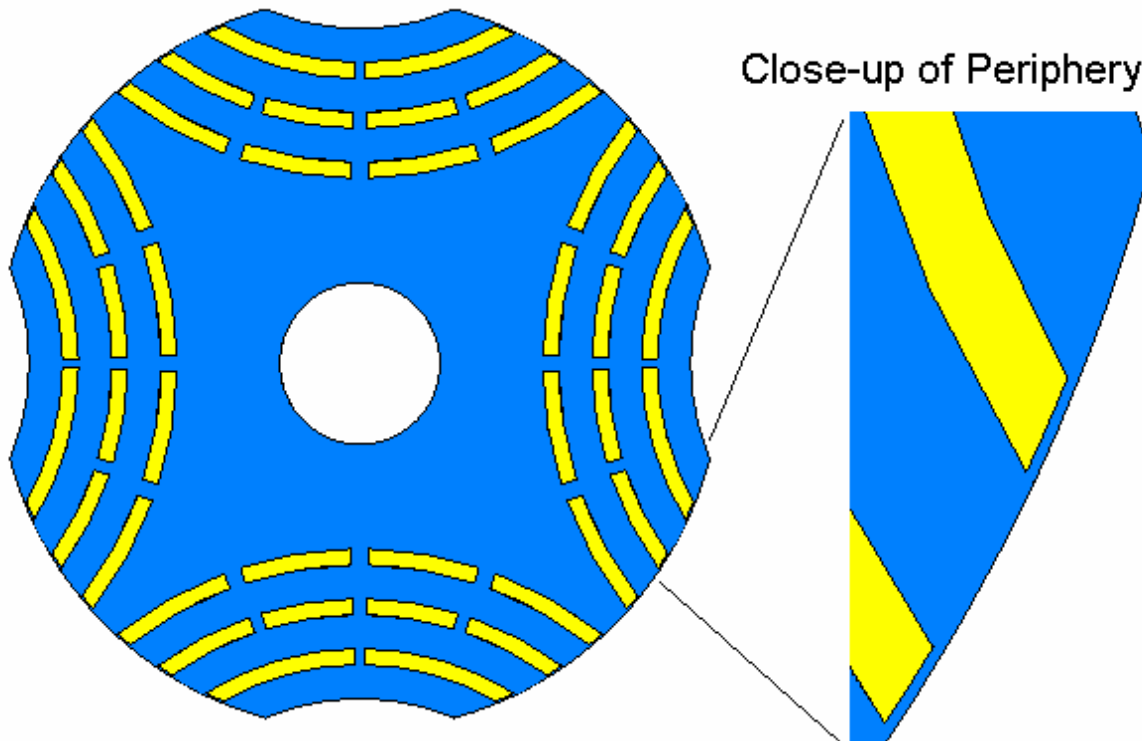


Figure 14-11: Conventionally Laminated Four-pole Rotor with Saturable Bridges

By changing to a four-pole machine, the frequency of the flux in the machine is doubled. To keep the iron loss reasonably low, the maximum rotation speed is lowered to 12,000 rpm. This is still higher than the base frequency, 250 Hz, for a two-pole motor at 15,000 rpm, but the 400 Hz for the four-pole at 12,000 rpm is still reasonable.

14.4 New Motor/Generator Design

For the four-pole machine, it is still desirable for the rotor to have a large outer diameter. The desire for small bridges though means that a smaller diameter has to be used to have reasonable structural stresses. To further strengthen the rotor the nonmagnetic sections are filled with injectable fiberglass.

Table 14-1 gives the dimensions for one such machine, and the cross-section is shown in Figure 14-11. The bridges on the periphery of the rotor are kept very small since they do not contribute a great deal structurally and decrease the L_d/L_q ratio more than the inner bridges due to increased leakage inductance. These periphery bridges instead function only to hold in the injectable fiberglass. The full-load torque and power curves are shown in Figures 14-12 and 14-13 respectively. The full-load power loss in the rotor is shown in Figure 14-14.

Machine length	30 inches
Stator diameter	16 inches
Rotor diameter	10 inches
Poles	4
Slots per-phase per-pole	3
Turns per-slot	1
Magnetic Layers per-pole	3.5

Table 14-1: Design for a Four-pole Machine with a Conventionally Laminated Rotor

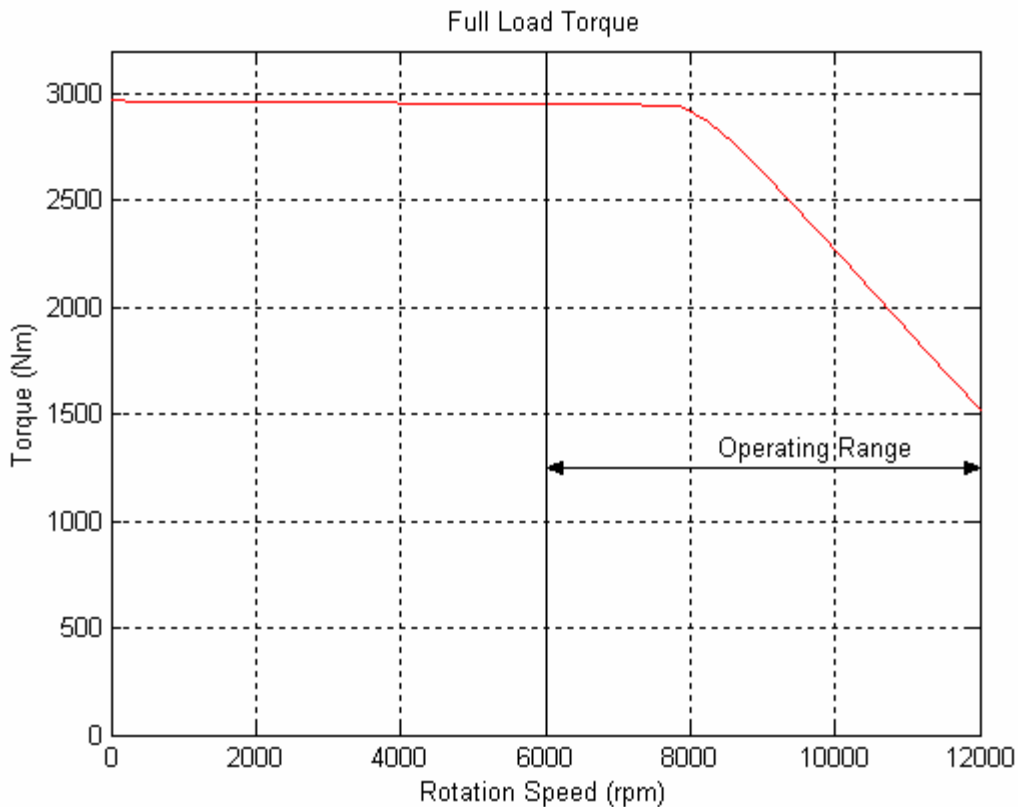


Figure 14-12: Simulation of Full-load Torque for Four-pole Machine

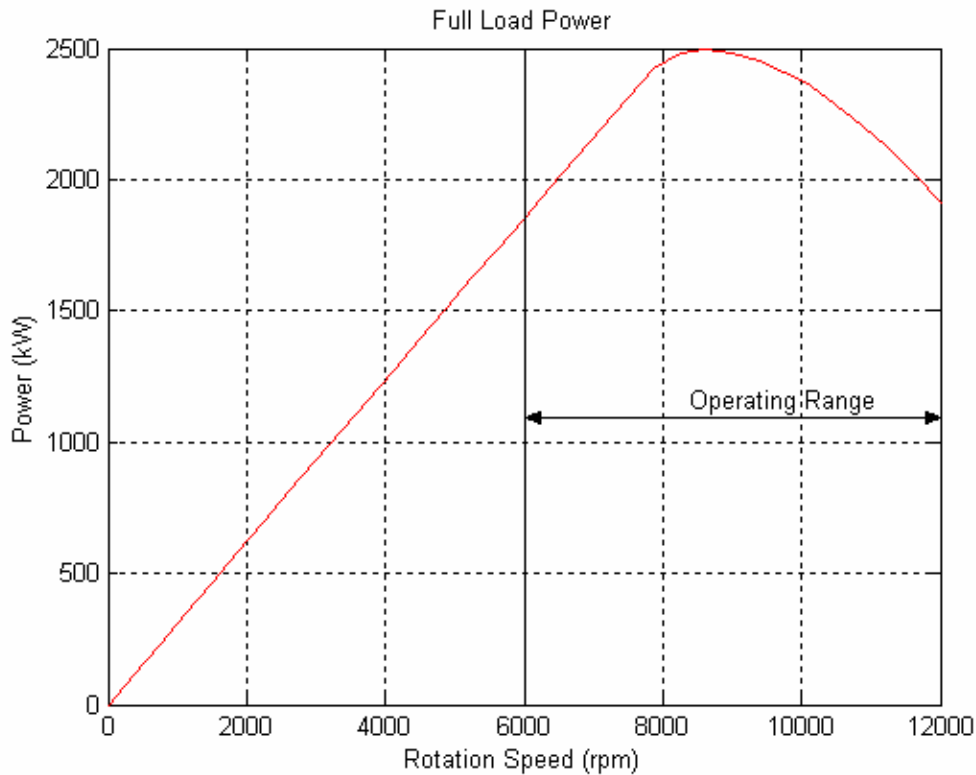


Figure 14-13: Simulation of Full-load Power for Four-pole Machine

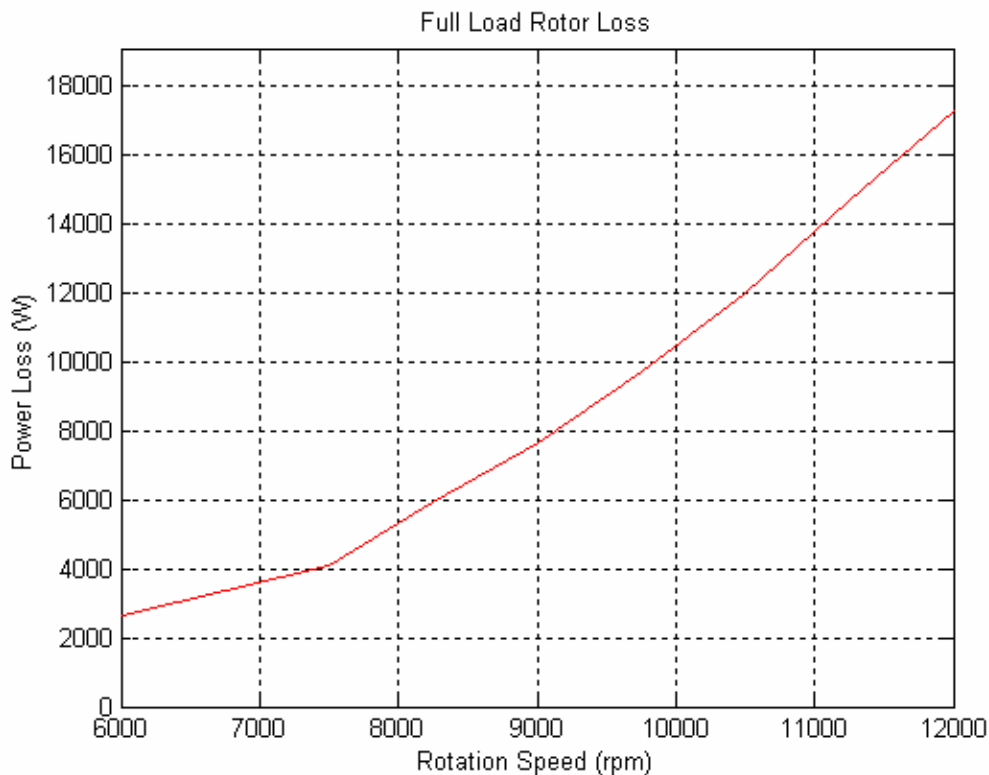


Figure 14-14: Simulation of Full-load Rotor Loss for Four-pole Machine

This machine design has much lower rotor loss than the previously designed machines. The maximum power that the rotor can continuously transfer in a hydrogen atmosphere is 10,240 W. The convection effects from rotation, which is currently not modeled in the thermal simulations, or through the use of a changeable hydrogen pressure, will increase this allowable loss. However even with a 10,240 W limit, this rotor will work for many applications.

The loss in the machine at high rpm is largely due to a current angle approaching 90 degrees. Figure 14-15 shows how the loss changes with rpm if the current angle is kept constant over the full speed range. One of the ways to utilize this effect in certain application is to gradually decrease the maximum power of the machine after it has run for extended time. Another option is to operate the wheel for the majority of the time between 6,000 rpm and 10,000 rpm. In other applications, the wheel can be charged and discharged at full power as long as sufficient idling time is inserted between charging and discharging. Which of these alternatives will work best is highly dependent on the flywheel battery application.

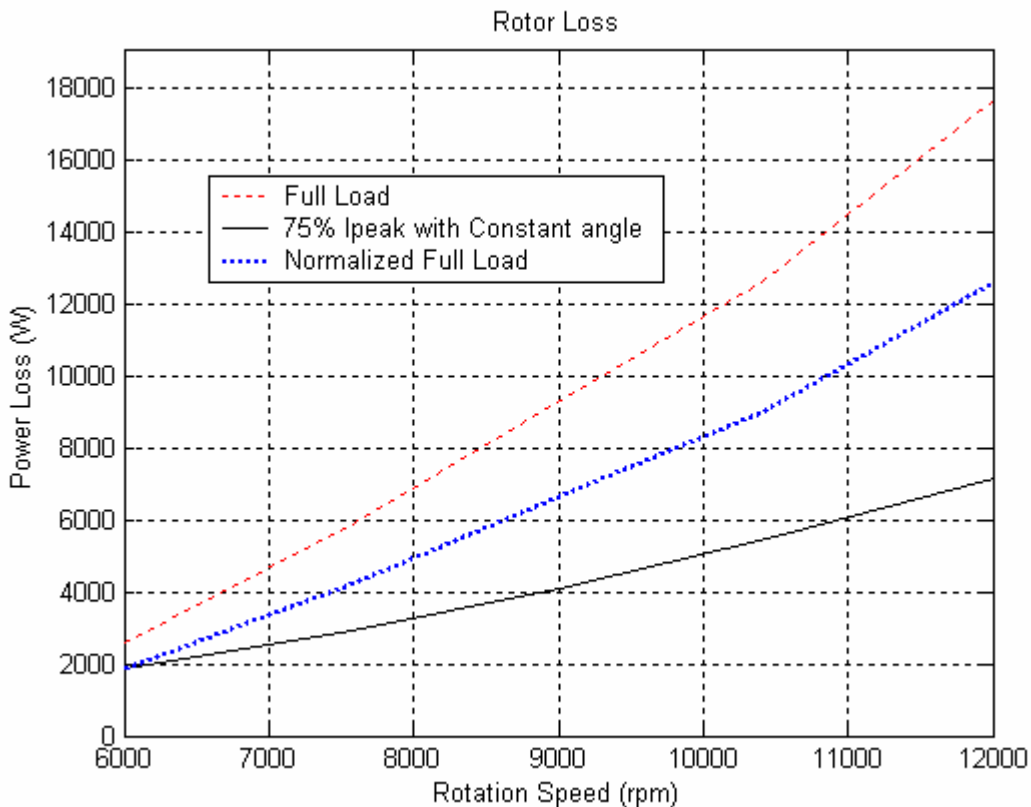


Figure 14-15: Four-pole Machine Rotor Loss with Constant Current Angle

A different solution is to change the power loss in the rotor by increasing the maximum power of the inverter without increasing the output power at 6,000 rpm. One simple way of doing this is to increase the dc-bus voltage of the inverter. Figure 14-16, 14-17, and 14-18 shows a comparison of how a 10% increase in inverter voltage changes the full-load power, current angle, and rotor loss. This change has the effect of lowering the operating current angle and thus lowering the rotor loss. It does this while increasing the full-load power at higher rotation speed. Due to the higher cost of this option, it may not be attractive for many applications.

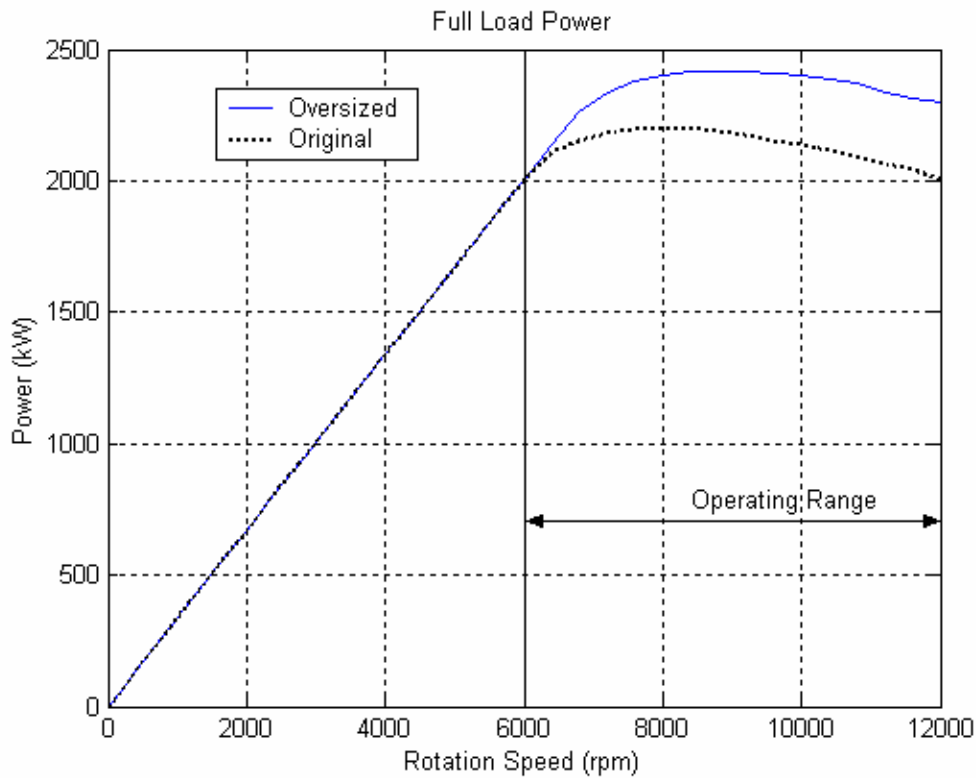


Figure 14-16: Comparison of Full-load Power for Regular and Oversized Inverter

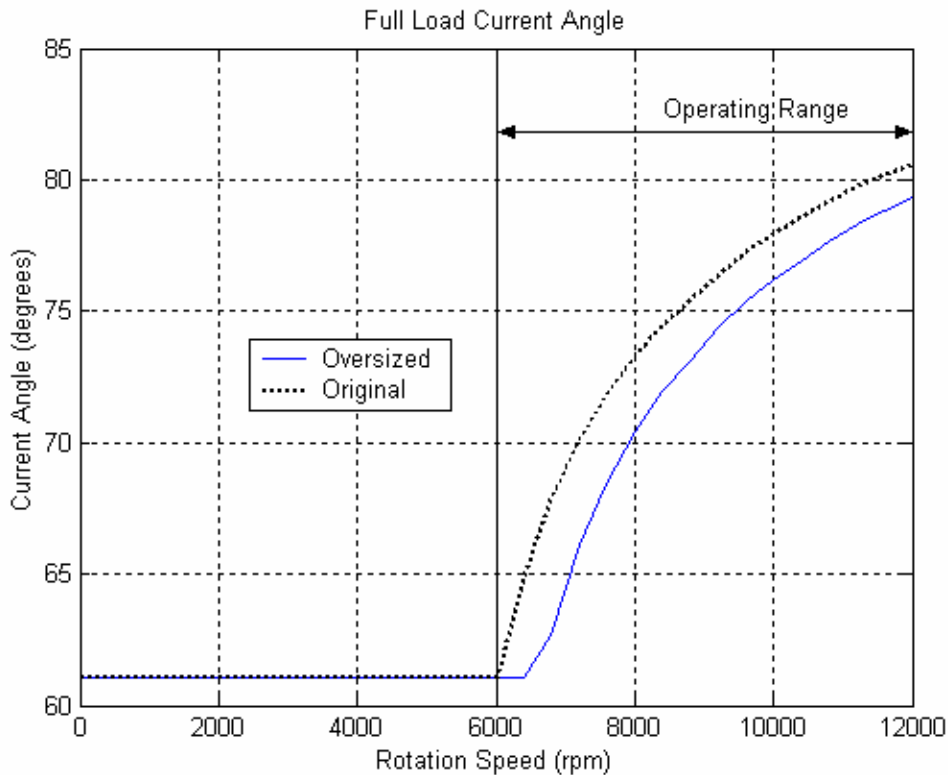


Figure 14-17: Comparison of Current Angle for Regular and Oversized Inverter

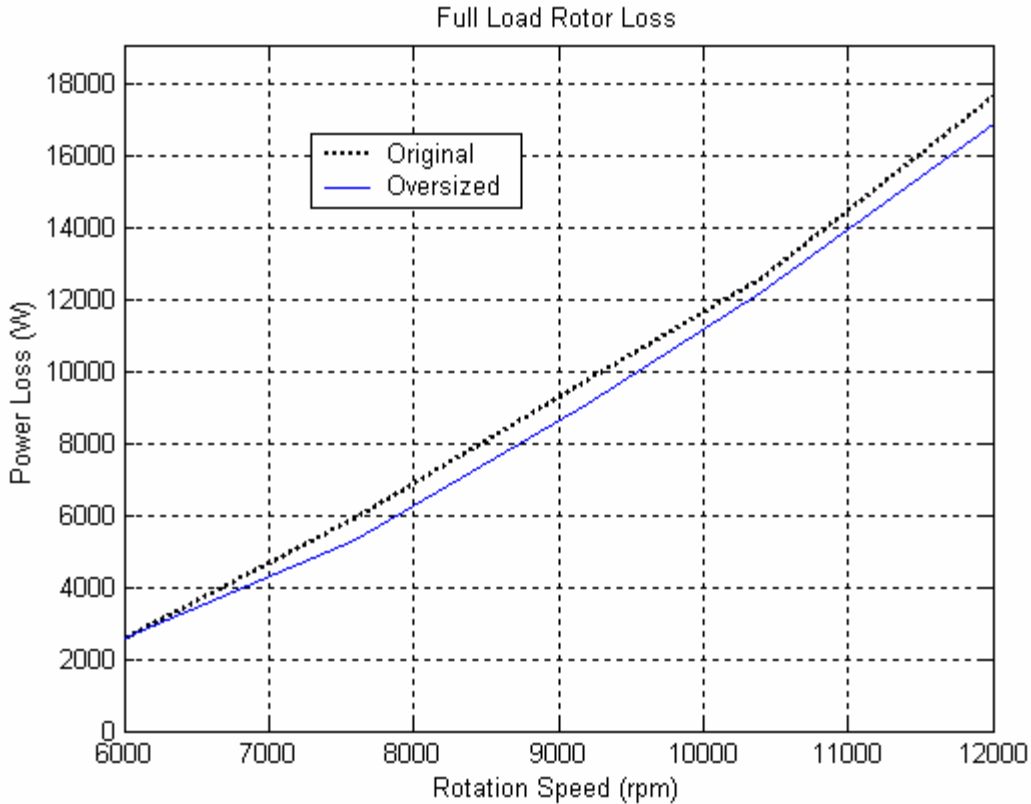


Figure 14-18: Comparison of Rotor Loss for Regular and Oversized Inverter

14.5 Conclusion of Four-pole Design

The conventionally laminated rotor appears to be the best solution for a low rotor loss SYNREL machine. Due to the shaft requirements for a high speed machine, a four-pole machine is better than a two-pole. The rotor in Table 14-1 and Figure 14-11 is one such machine that will work. Several operating options are possible that make the above rotor loss acceptable for many applications. When convection is included in the model combined with the ability to change the hydrogen pressure, the machine should be able to continuously run at full-load power.

A machine with a larger diameter than the one in Table 14-1 may be able to achieve higher performance or lower cost, but significant analysis of the structural stresses and dynamics would be needed and is beyond the scope of this thesis.

14.6 Motor/Generator Changes Based on Economic Analysis

An economic analysis of flywheel batteries is described in Section 16. In this analysis the appropriate ratio of power rating to maximum energy capacity are also derived for various applications. The conclusion of this work is that, with the possible exception of peak power buffer applications, a motor/generator with a continuous rating of 2 MW is oversized for a 100 kWh wheel. For a 100 kWh wheel more appropriate power ratings are 1 MW peak (500 kW continuous), 200 kW peak (100 kW continuous), and 40 kW peak (20 kW continuous) depending on the application.

For a 1 MW peak motor/generator, the only necessary changes to the 2 MW machine are to half the length and change the stator winding. The rotor loss at peak currents will be half those in Figure 14-14 (heat transfer will also be half), and since this is a temporary condition the loss is not excessive. At continuous power levels the rotor loss will be less due to lower flux density in the rotor, as illustrated in Figure 14-15. The lower flux density will occur due to decreases in both current angle and current magnitude. This decrease in rotor loss will allow the hydrogen pressure to be extremely low and will further reduce the flywheel's windage loss.

A possible additional change for the 1 MW motor/generator is to place rods through the rotor laminations and secure them with end plates. This allows for an increase in rotor diameter and decrease in machine length. This change in dimensions results in a larger L_d/L_q ratio for the machine and possibly eliminates a set of magnetic bearings. A larger L_d/L_q ratio obviously improves the motor/generator performance. The elimination of the magnetic bearing may be possible due to the shorter length of the rotating assembly. This additional change needs additional advanced structural analysis, but should be considered if a full-scale motor/generator of this size is fabricated.

For the 200 kW peak (or similar power rating) two design changes are possible. Due to the significantly lower power, it is possible to design the machine with significantly lower flux density in the rotor. This decrease in flux density results in a significant reduction in rotor loss, especially at continuous loads, and may enable the use of a vacuum type enclosure. The shorter length of this motor/generator also makes the design change for the 1 MW motor/generator an even better possibility. This will ensure the elimination of a magnetic bearing and improve the machine performance.

The design of a 40 kW peak or less motor/generator is considerably different from the original 2 MW motor/generator. Similar changes as for the 200 kW are possible. These changes should definitely eliminate one of the magnetic bearings and enable the use of a vacuum type enclosure. At this low power level, for a 100 kWh capacity flywheel, the use of a PMAC machine may also need to be reconsidered.

15 Control of the Synchronous Reluctance Machine

The control of a synchronous reluctance machine, at a high level, is similar to other brushless synchronous machines. Figure 15-1 shows a high level block diagram for the control system. It consists of a speed controller, current controllers, and the various transformations.

The speed controller is identical to the type of control utilized by many brushless motor controllers. The controller inputs are the desired speed and the actual speed. The outputs are a torque magnitude that is changed to an appropriate current for the current controller. The controller itself can be of any type, but the simplest solution is to use a PI controller with an equation of

$$G_c(s) = \frac{k_I}{s} + k_P \quad (15-1).$$

The open loop transfer function of the system is

$$G_o(s) = \frac{\omega_m(s)}{X_{in}(s)} = \frac{k_t}{B_{fric} + J_{eq}s} \quad (15-2),$$

where k_t and X_{in} are both derived from the SYNREL torque equation as will be described, B_{fric} is the coefficient of friction for the system including bearings and windage, and J_{eq} is the inertia of the motor and load. If the current controller is significantly fast, the speed controller is designed by choosing a cutoff frequency, gain margin, and phase margin using the following equations:

$$\left| \frac{k_t k_I + \omega_c k_t k_P}{(B_{fric} + J_{eq} \omega_c) \omega_c} \right| = 1 \quad (15-3),$$

$$\angle \left(\frac{k_t k_I + \omega_c k_t k_P}{(B_{fric} + J_{eq} \omega_c) \omega_c} \right) = -180 + \psi_{PM}$$

where k_t is the machines torque coefficient, k_P and k_I are the P and I term of the PI controller, ω_c is the cutoff frequency, and ψ_{PM} is the desired phase margin in degrees [9].

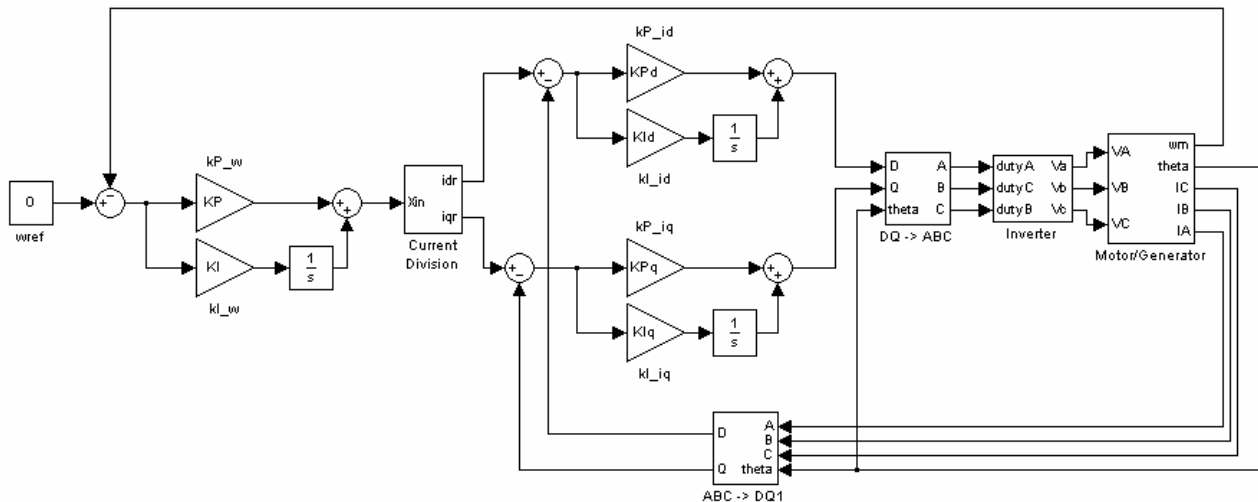


Figure 15-1: High level Control Diagram for Synchronous Reluctance Machine

The current controller in the system has significant differences from the standard brushless motor controller. While the controllers for the d and q axis currents are similar to other systems, the calculation of the requested d and q axis currents are quite different. One of the simplest types of controller to use for the current is again a PI controller. So that the currents can be decoupled, the q axis current should respond faster than the d axis current. If this is the case, the open loop transfer functions for the d and q axis currents are

$$G_d(s) = \frac{i_d(s)}{V_d(s)} = \frac{1}{R_s + L_d s} \quad (15-4),$$

$$G_q(s) = \frac{i_q(s)}{V_q(s)} = \frac{1}{R_s + L_q s}$$

where R_s is the phase resistance, L_d and L_q are the d and q axis inductances, V_d and V_q are the d and q axis voltages, and i_d and i_q are the d and q axis currents. Using these transfer functions the controller can be designed by choosing a cutoff frequency, gain margin, and phase margin using the following equations:

$$\left| \frac{k_{Id} + \omega_c k_{Pd}}{(R_s + L_d \omega_{cd}) \omega_{cd}} \right| = 1 \quad (15-5)$$

$$\angle \left(\frac{k_{Id} + \omega_c k_{Pd}}{(R_s + L_d \omega_{cd}) \omega_{cd}} \right) = -180 + \psi_{PMd}$$

$$\left| \frac{k_{Iq} + \omega_c k_{Pq}}{(R_s + L_q \omega_{cq}) \omega_{cq}} \right| = 1 \quad (15-6),$$

$$\angle \left(\frac{k_{Iq} + \omega_c k_{Pq}}{(R_s + L_q \omega_{cq}) \omega_{cq}} \right) = -180 + \psi_{PMq}$$

where k_{pd} , k_{pq} , k_{id} and k_{iq} are the P and I term of the PI controller, ω_{cd} and ω_{cq} are the cutoff frequencies, and ψ_{PMd} and ψ_{PMq} are the desired phase margins.

How to divide up the desired torque from the speed controller between the d and q axis currents can be done in several different ways. The basis for the all of them is transferring the torque expression $T = \frac{3}{2} \left(\frac{P}{2} \right) (L_d - L_q) i_d i_q$ into $T = k_t X_{in}$ with $X_{in} = i_d i_q$. The currents are then set to a ratio using the expression $\frac{i_d}{i_q} = k_R$, where k_R is determined by the kind of machine performance

that is desired. From this expression, it can be derived that $i_q = \sqrt{\frac{X_{in}}{k_R}} = k_q \sqrt{X_{in}}$ and $i_d = \sqrt{X_{in} k_R} = k_d \sqrt{X_{in}}$, where k_d and k_q are the terms seen in Figure 15-2.

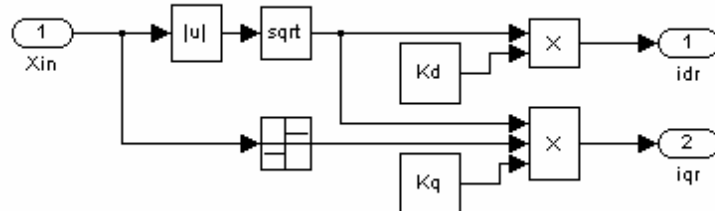


Figure 15-2: Controls for Deriving i_d and i_q Reference Current

The first method for dividing up the current achieves maximum torque per current and thus has the lowest resistive loss. To find this condition

$$\frac{T}{I_s} = \frac{\frac{3}{2} \left(\frac{P}{2} \right) (L_d - L_q) i_d i_q}{\sqrt{i_d^2 + i_q^2}} \quad (15-7),$$

where I_s is the peak vector of the stator currents. The k_R value is found by solving for i_d and i_q

with $\frac{\partial \left(\frac{T}{I_s} \right)}{\partial \left(\frac{i_d}{i_q} \right)} = 0$. The resulting k_R value is $k_R = \frac{i_d}{i_q} = 1$ and for Figure 15-2 $k_d=1$ and $k_q=1$. Using

this relationship can result in large saturation in the d axis. To alleviate the problem, the k_R term is decreased slightly so that the i_q current is greater than i_d .

Another useful method is to set the ratio for maximum power factor. To find this

$$\frac{P}{VA} = \frac{\frac{3}{2} \left(\frac{P}{2} \right) (L_d - L_q) i_d i_q \omega_m}{\sqrt{\left(L_d i_d \omega_m \left(\frac{P}{2} \right) \right)^2 + \left(L_q i_q \omega_m \left(\frac{P}{2} \right) \right)^2} \left(\sqrt{i_d^2 + i_q^2} \right)} \quad (15-8),$$

where P is the power produced by the machine, VA is the voltage peak times the current peak, and ω_m is the rotation speed of the machine. The k_R value is found by solving for i_d and i_q with

$\frac{\partial \left(\frac{P}{VA} \right)}{\partial \left(\frac{i_d}{i_q} \right)} = 0$. The resulting k_R value is $k_R = \frac{i_d}{i_q} = \sqrt{\frac{L_q}{L_d}}$ and for Figure 15-2 $k_d = \sqrt[4]{\frac{L_q}{L_d}}$ and

$k_q = \sqrt[4]{\frac{L_d}{L_q}}$. If a very simple controller is needed for a flywheel application, this ratio will

probably work best since it maximizes the output power of the machine, but the machine will not run at maximum efficiency.

The last constant angle method maximizes the torque response. To achieve fast torque response, the torque per flux linked needs to be maximized. This results in

$$\frac{T}{\lambda_s} = \frac{\frac{3}{2} \left(\frac{P}{2} \right) (L_d - L_q) i_d i_q}{\sqrt{(L_d i_d)^2 + (L_q i_q)^2}} \quad (15-9),$$

where λ_s is the peak flux linkage of the machine. The k_R value is found by solving for i_d and i_q

with $\frac{\partial \left(\frac{T}{\lambda_s} \right)}{\partial \left(\frac{i_d}{i_q} \right)} = 0$. The resulting k_R value is $k_R = \frac{i_d}{i_q} = \frac{L_q}{L_d}$ and for Figure 15-2 $k_d = \sqrt{\frac{L_q}{L_d}}$ and

$k_q = \sqrt{\frac{L_d}{L_q}}$. For the majority of flywheel battery applications, this method is not needed since the

response time of the other methods are usually adequate.

The constant current angle control will work fairly well but is not able to maximize the efficiency of machine. The constant current angle set to achieve maximum torque per current comes close at low rotation speeds, but as speed increases the iron loss in the machine should also be considered. The maximum torque per loss is

$$\frac{T}{P_r + P_{fe}} = \frac{\frac{3}{2} \left(\frac{P}{2} \right) (L_d - L_q) i_d i_q}{R_s (i_d^2 + i_q^2) + R_{ms} i_d^2 + R_{mr} i_q^2} \quad (15-10),$$

where P_r is the resistive loss of the machine, P_{fe} are the iron loss in the machine, R_s is the resistance of the machine, R_{ms} is an equivalent resistor that represents the stator iron loss, and R_{mr} is an equivalent resistor that represents the rotor iron loss [12]. Both R_{ms} and R_{mr} assume that the stator loss is mainly dependent on d axis current, and the rotor loss is mainly due to q axis currents. While this isn't exactly accurate, it is sufficient for finding a correct k_R current ratio.

The k_R value for maximum efficiency is found by solving for i_d and i_q with $\frac{\partial}{\partial \left(\frac{i_d}{i_q} \right)} \left(\frac{T}{P_r + P_{fe}} \right) = 0$. The

resulting k_R value is $k_R = \frac{i_d}{i_q} = \sqrt{\frac{R_s + R_{mr}(\omega_m)}{R_s + R_{ms}(\omega_m)}}$ and for Figure 15-2 $k_d = \sqrt[4]{\frac{R_s + R_{mr}(\omega_m)}{R_s + R_{ms}(\omega_m)}}$ and

$k_q = \sqrt[4]{\frac{R_s + R_{ms}(\omega_m)}{R_s + R_{mr}(\omega_m)}}$. Unlike the constant angle expressions, the k_d and k_q terms are now a function of the rotation speed.

In the majority of flywheel battery applications, the most desirable control operation will be to use the maximum efficiency control until the maximum peak voltage is reached. When the peak voltage is reached, the control switches to maximum power factor control. An easy way to accomplish this is to calculate both i_d and i_q for both efficiency and power factor, and use the i_d and i_q combination that has the minimum i_d current. The ratios k_d and k_q for efficiency change with rotation speed to achieve minimal loss. These changeable k_d and k_q terms also limit the i_d current. This limiting is again done to prevent magnetic saturation in the machine.

As the speed of the machine increases, the maximum torque of the machine is decreased due to the maximum voltage of the inverter. To account for this in the control, a block is needed that limits the X_{in} term so that higher torques than can be achieved are not requested. In addition, X_{in} should be limited to account for the maximum current of the inverter. If the limiting is not included in the controller, higher X_{in} values can be requested that will change the k_R value and thus prevent the machine from working at maximum efficiency or power factor. The X_{in} value should be limited to the following:

$$X_{lim} = \frac{k_R I_{spk}^2}{1 + k_R^2} \quad \text{for } \omega_m < \omega_{base}$$

$$X_{lim} = \frac{\sqrt{\omega_e^2 I_{spk}^2 V_{spk}^2 (L_d^2 + L_q^2) - V_{spk}^4} - \omega_e^4 L_d^2 L_q^2 I_{spk}^4}{\omega_e^2 (L_d^2 - L_q^2)} \quad \text{for } \omega_m \geq \omega_{base}$$
(15-11),

where X_{lim} is the limiting X_{in} value, k_R is the $\frac{i_d}{i_q}$ ratio, I_{spk} is the maximum peak current of the inverter, V_{spk} is the maximum peak voltage of the inverter, ω_m is the rotation speed, ω_{base} is the rotation speed at which the voltage limit is encountered at maximum current, and ω_e is the electrical frequency or $\omega_e = \omega_m \left(\frac{P}{2} \right)$.

It is also advisable to include the temperature of the machine and or the inverter in the limiting block so that neither overheats. There are numerous way of achieving this depending on the types of thermal system used and the desired safety factors. A rough concept of the controller for the flywheel motor/generator is shown in Figure 15-3.

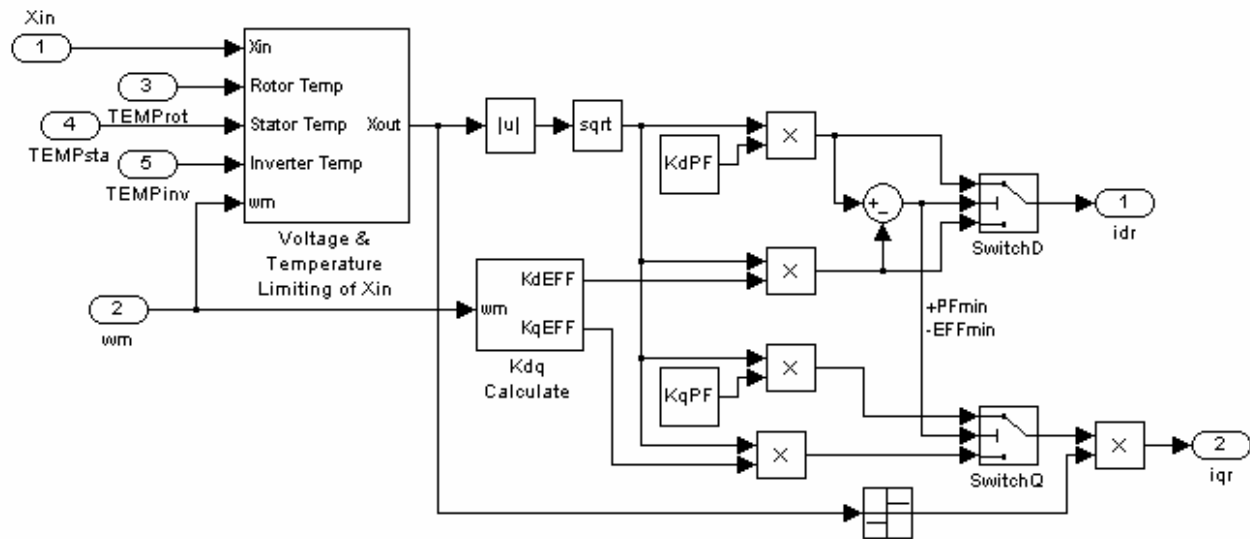


Figure 15-3: Current Division with Limiting Controls

For the system in Figure 15-1, the speed control loop is not the most useful control method for the flywheel battery. A better type of control replaces the speed loop with a controller that maintains the dc-bus voltage of the inverter. This type of control allows quick bi-directional current flow depending on load conditions. The load conditions are tracked by the grid connected inverter. This allows the motor/generator inverter to control the machine and maintain the dc-bus voltage regardless of the grid conditions. The grid inverter in the same way is decoupled from the motor/generator and instead can control functions such as voltage support.

Figure 15-4 shows the control system where the dc-bus voltage is instead controlled by the inverter. For this system, it is assumed that a constant dc-bus voltage is desired. The open loop transfer function of the system is

$$G_v(s) = \frac{V_{dc}(s)}{X_{in}(s)} = \frac{k_t \omega_m \left(\frac{P}{2} \right)}{V_{dcref} (R_{load} + C_{dc}s)} \quad (15-12),$$

where V_{dc} is the dc-bus voltage, k_t is the machine torque constant, P is the number of machine poles, ω_m is the rotation speed, V_{dcref} is the desired dc-bus voltage, R_{load} is the estimated load resistance, and C_{dc} is the dc-bus capacitance. For this transfer function, it is assumed that the dc-bus voltage does not change greatly, or this equation will not yield a good controller. It is also assumed that ω_m changes slowly compared to the control. For most flywheels, this is a fairly safe assumption since the inertia is usually large. The controller is designed using the equations:

$$k_v = \frac{k_t \omega_m \left(\frac{P}{2} \right)}{V_{dcref}}$$

$$\left| \frac{k_v k_I + \omega_c k_v k_p}{(R_{load} + C_{dc} \omega_c) \omega_c} \right| = 1 \quad (15-13),$$

$$\angle \left(\frac{k_v k_I + \omega_c k_v k_p}{(R_{load} + C_{dc} \omega_c) \omega_c} \right) = -180 + \psi_{PM}$$

where k_p and k_I are the P and I term of the PI controller respectively, ω_c is the cutoff frequency, and ψ_{PM} is the desired phase margin. This controller must specifically be designed for robustness since both the ω_m and R_{load} terms will be variable during operation. One possible solution is to change the k_p and k_I value depending on rotation speed and load.

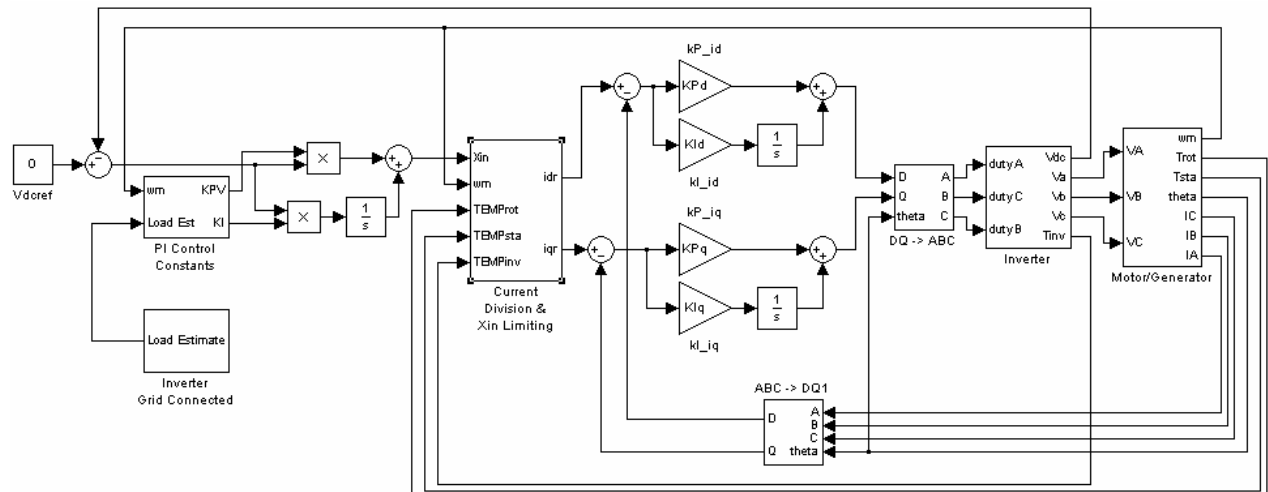


Figure 15-4: DC Voltage Link Control

By combining the controllers in Figures 15-3 and 15-4, a high performance controller for the motor/generator is possible. This controller will give high efficiency, maximum power, and fast response. In addition, the grid connected inverter is decoupled from the motor/generator but will still have the power it needs at any given time.

16 Economics of Possible Flywheel Applications

The economics of flywheel batteries are examined for wind systems and non-wind applications. The economics in both cases are examined for both current generation and technology conditions, and for possible future changes and advancements.

For all applications the initial capital investment for the flywheel batteries is

$$CAP_T = P_f d_{pe} + P_f d_{mg} + E_f d_{en} \quad (16-1),$$

where CAP_T is the initial capital investment in dollars, P_f is the power rating of the flywheel, E_f is the storage capacity of the flywheel in kWh, d_{pe} is the cost of the power electronics in \$/kW, d_{mg} is the cost of the motor/generator in \$/kW, and d_{en} is the cost of the energy storage including the wheel, bearings, and enclosure in \$/kWh. Costs of the flywheel components are difficult to obtain since much of the technology is still in development, but for a rough analysis of the economics d_{pe} , d_{mg} , and d_{en} are projected to be 10 \$/kW, 90 \$/kW, and 3000 \$/kWh respectively. The energy storage cost, d_{en} , may come down greatly from this number as composite technology improves and becomes less costly.

16.1 Flywheel Economics for Non-wind Applications

For non-wind applications, energy storage is examined as a possible future business. If the energy storage results in a sufficient profit each year, the flywheel batteries become a realistic business. To determine the required yearly profit, the justifiable capital per MW is calculated using

$$CAP_J = \frac{C_y}{FCR} \quad (16-2),$$

where CAP_J is the justifiable capital, C_y is the yearly profit in \$, and FCR is the fixed charge rate, which factors in costs such as interest, depreciation, taxes, etc., is set to 15% [15]. If CAP_J is greater than the initial capital, CAP_T , then the flywheel battery application is a viable business.

In the following analysis only the main economic factors are considered. Using the flywheel's grid connected inverter to provide reactive power, improve grid stability, or provide other FACTs [16] like functions is not factored into the analysis. The ability of flywheel batteries to provide these additional services will further improve the economics.

16.1.1 Spinning Reserve

In the case of an emergency or incorrect load forecasting, spinning reserve is required to quickly come online to provide the required additional power. Currently, gas turbines idle until spinning reserve is required at which time the gas turbines produce the additional generation. If flywheels are utilized for spinning reserve, the gas turbines can normally be turned off. When the spinning reserve is required, the flywheels provide the power until the gas turbines come online (typically 10 minutes). From this type of operation a profit is achievable due to the much lower cost of idling the flywheel as opposed to the gas turbine. As composite technology advances it might also be possible to increase the energy storage of the flywheel so that slower and low cost generation sources may also be able to bid for spinning reserve generation.

The economics of utilizing a flywheel with gas turbine generation is first analyzed. In this situation the yearly idling cost of the gas turbine per MW is

$$C_{gy} = 365t_d P_g d_g + C_{gm1} \quad (16-3),$$

where t_d is the average idling time in a day in hours, P_{gi} is the idling power of the gas turbine as a fraction of the MW rating, d_g is the gas turbine's energy cost in \$/MWh, and C_{gm1} is the yearly maintenance cost of the gas turbine in \$. The yearly idling cost of the flywheel per MW is

$$C_{fy} = 365 \left(\frac{n_{sp} E_{sp}}{\eta_{mg}^2} + t_d P_{fi} \right) d_f + C_{fm} - (C_{gm1} - C_{gm2}) - C_{env} \quad (16-4),$$

where n_{sp} is the average number of times the spinning reserve is turned on during a day, E_{sp} is the storage capacity of the flywheel in MWh, η_{mg} is the motor/generator efficiency, P_{fi} is the idling power of the flywheel as a fraction of the MW rating, d_f is the flywheel's energy cost in \$/MWh, C_{fm} is the yearly maintenance cost of the flywheel in \$, $(C_{gm1} - C_{gm2})$ is the yearly difference in the gas turbines maintenance cost due to the flywheel in \$, and C_{env} is a possible environmental credit in \$. The profit per year, C_{ysp} , for each MW of spinning reserve is calculated as

$$C_{ysp} = C_{gy} - C_{fy} \quad (16-5).$$

The required flywheel capacity, E_{sp} , is

$$E_{sp} = \frac{P_{sp} t_{sp}}{\eta_{mg}} \quad (16-6),$$

where P_{sp} is the spinning reserve power (1 MW for consistency with Equation 16-4) and t_{sp} is the time period for which the flywheel must supply the spinning reserve power. A gas turbine's maintenance cost is highly dependent on its hours of operation. Since the flywheel significantly reduces the hours of operation, a cost reduction is included in equation 16-4 as $(C_{gm1} - C_{gm2})$. Due to the substantial improvement in emissions by using the flywheel for spinning reserve, an environmental credit is very likely possible for this application and thus C_{env} is included in equation 16-4.

To gain a rough understanding of the economic feasibility of the flywheel for spinning reserve, the estimates in Table 16-1 are used.

t_d	24 hr	C_{gm1}	\$50,000	C_{fm}	\$5,000
P_{gi}	0.1	η_{mg}	0.97	$(C_{gm1} - C_{gm2})$	\$25,000
d_g	100 \$/MWh	P_{fi}	0.002* E_{sp}	C_{env}	\$0

Table 16-1: Estimates for Rough Economic Feasibility of Spinning Reserve

In these estimates a worse case situation for the flywheel is assumed, by assigning no environmental credit and only reducing the gas turbine's maintenance cost in half. For these estimates, Figure 16-1 shows the variation in justifiable capital, CAP_J , based on variations in d_f for various values of t_{sp} and n_{sp} . E_{sp} is equal to 171.8 kWh and 343.6 kWh for t_{sp} equal to 10 and 20 minutes respectively. Since the grid or the gas turbine can supply the flywheel's power consumption (depending on which is more cost effective at the time), d_f becomes an important economic factor for the spinning reserve application. The initial capital investment, CAP_T , is also graphed in Figure 16-1 for t_{sp} equal to 10 and 20 minutes.

If the flywheel batteries supply spinning reserve power for a time period of 10 minutes, Figure 16-1 shows that the spinning reserve application is indeed a viable business. If slower startup times, such as 20 minutes, are required, Figure 16-1 shows that modest improvements in the cost of the energy storage, d_{en} , are necessary. If an environmental credit is possible, and a less conservative decrease in gas turbine maintenance cost is used, these improvements may not be required, and the profit for 10 minute startup units will be even more significant.

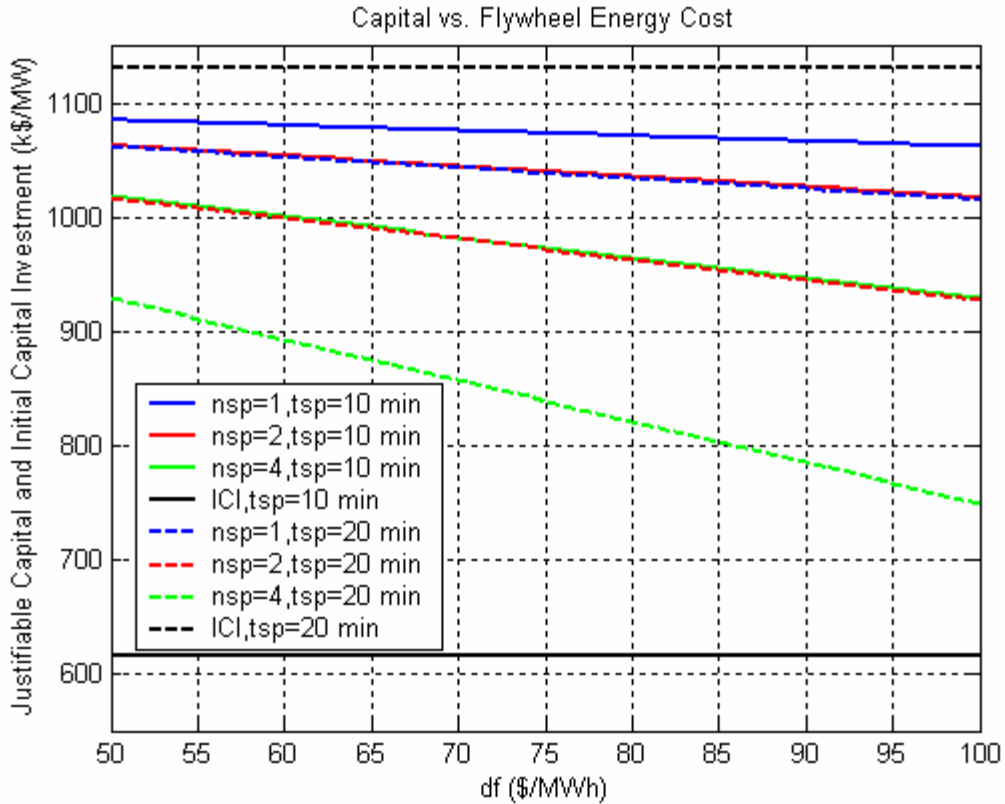


Figure 16-1: Justifiable Capital and Initial Capital Investment for Spinning Reserve Applications

While Figure 16-1 shows that increasing the startup time for the generation source decreases profits, the ability to use low cost generation sources will change these results. Since in these applications the cost of d_f will be less than 50 \$/MWhr, the required improvement in the cost of the energy storage will be less. If such an improvement is possible, the flywheel battery will enable slower low cost generation sources to bid for spinning reserve.

From the above analysis the power to energy ratio of a flywheel unit can be obtained. For t_{sp} equal to ten minutes the ratio is 5.82. For the ten minute startup time a 100 kWh flywheel will thus require a motor/generator with a rating of less than 600 kW, and for longer startups the rating will be even less. This result thus leads to the discussion of motor/generator power sizing in Section 14.6.

16.1.2 Frequency Regulation

Frequency regulation provides the power necessary to supply variations in the load on a short-term basis (10 to 15 minute basis). Since gas turbines can quickly adjust power output, they are utilized for this type of regulation. By combining flywheel batteries with slower and lower cost generation sources, such as coal-fired plants, frequency regulation is also possible. Thus generation sources that have traditionally only been able to supply base power, can now supply both base power and frequency regulation resulting in the potential for substantial profit.

The economics of utilizing a flywheel with a coal-fired plant are compared to the cost of installing and using gas turbines for frequency regulation. The yearly flywheel operating cost per MW is

$$C_{fy} = 365 \left(\frac{n_{fr} E_{fr}}{\eta_{mg}^2} + t_d P_{fi} \right) d_f + C_{fm} \quad (16-7),$$

where n_{fr} is the average equivalent charge/discharge cycles during a day, E_{fr} is the storage capacity of the flywheel in MWh, η_{mg} is the motor/generator efficiency, P_{fi} is the idling power of the flywheel as a fraction of the MW rating, t_d is the average time in a day hours that frequency regulation is performed, d_f is the flywheel's energy cost in \$/MWh (cost of coal-fired energy in this case), and C_{fm} is the yearly maintenance cost of the flywheel in \$. The yearly gas turbine operating cost per MW is

$$C_{gy} = 365 \left(n_{fr} E_{fr} (1 - P_{gi}) + t_d P_{gi} \right) d_g \quad (16-8),$$

where P_{gi} is the idling power of the gas turbine as a fraction of the MW rating and d_g is the gas turbine's energy cost in \$/MWh. In Equation 16-8 the costs are correlated to the flywheel cost and the gas turbines maintenance cost is integrated into d_g . The profit per year, C_{yfr} , for each MW of frequency regulation is calculated using equation 16-5, but the initial capital cost, CAP_T , is different since the cost of building the gas turbine should be included or

$$CAP_T = P_f d_{pe} + P_f d_{mg} + E_f d_{en} - P_f d_{gt} \quad (16-9),$$

where d_g is the installation cost of gas turbines in \$/kW.

Additional environmental credit may also be possible due to lowered emissions with the flywheel setup, but it may be more difficult to get for frequency regulation than for the spinning reserve. Additional cost savings or lower emissions may also be possible by the flywheel allowing the generation source to have a slower time constant for changing power. This is related to the pollution credit discussed in 1.1.4.

To gain a rough understanding of the economic feasibility of the flywheel for frequency regulation, the estimates in Table 16-2 are used.

η_{mg}	0.97	C_{fm}	\$5,000
t_d	24 hr	P_{gi}	0.1
P_{fi}	0.002* E_{fr}	d_g	200 \$/MWh
d_f	25 \$/MWh	d_{gt}	500 \$/kW

Table 16-2: Estimates for Rough Economic Feasibility of Frequency Regulation

For these estimates Figure 16-2 and Figure 16-3 show justifiable capital, CAP_J , and initial capital cost, CAP_T , for variations in E_{fr} and n_{fr} respectively.

Figure 16-2 and 16-3 show that flywheel batteries are extremely profitable in frequency regulation. The key to realizing a high profit is a moderately large number of equivalent cycles, n_{fr} , during the day. If n_{fr} is great, large energy capacity, E_{fr} , also increases the profitability (assuming full flywheel capacity is utilized). The appropriate energy capacity, E_{fr} , and equivalent cycles, n_{fr} , vary depending on the system, and require an in depth study of the specific power system. Similar to spinning reserve the power to energy ratio is low (at most 10 and 5 or less provides better profit) and again leads to the discussion of motor/generator power sizing in Section 14.6. From this analysis it appears that frequency regulation is a tremendously attractive application for flywheel batteries.

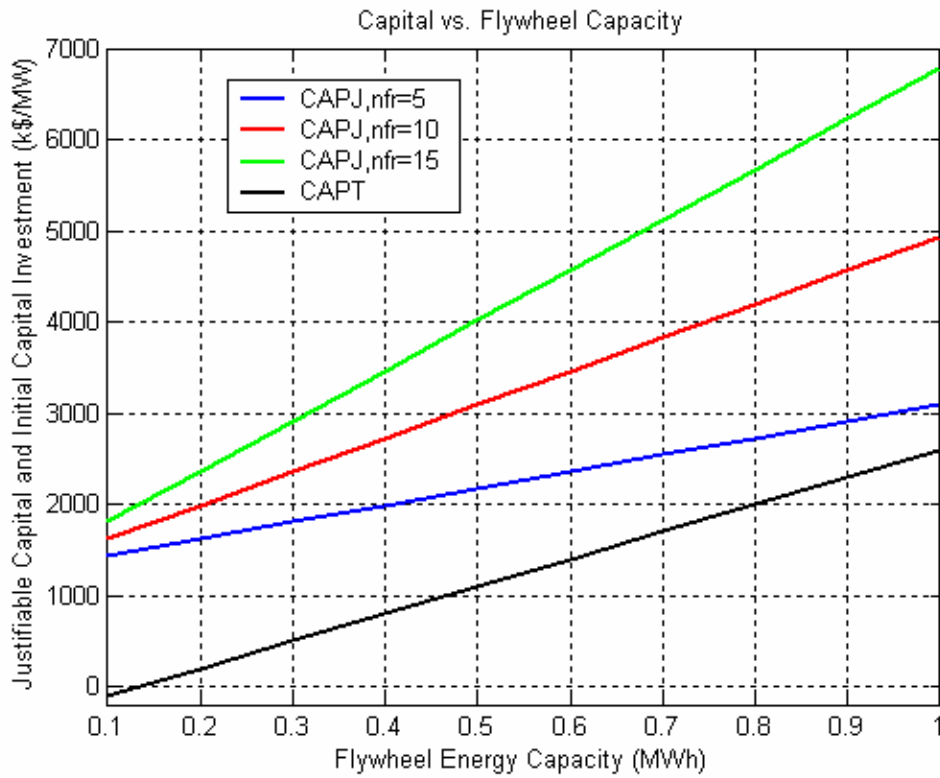


Figure 16-2: Justifiable Capital and Initial Capital Investment Depending on E_{fr}

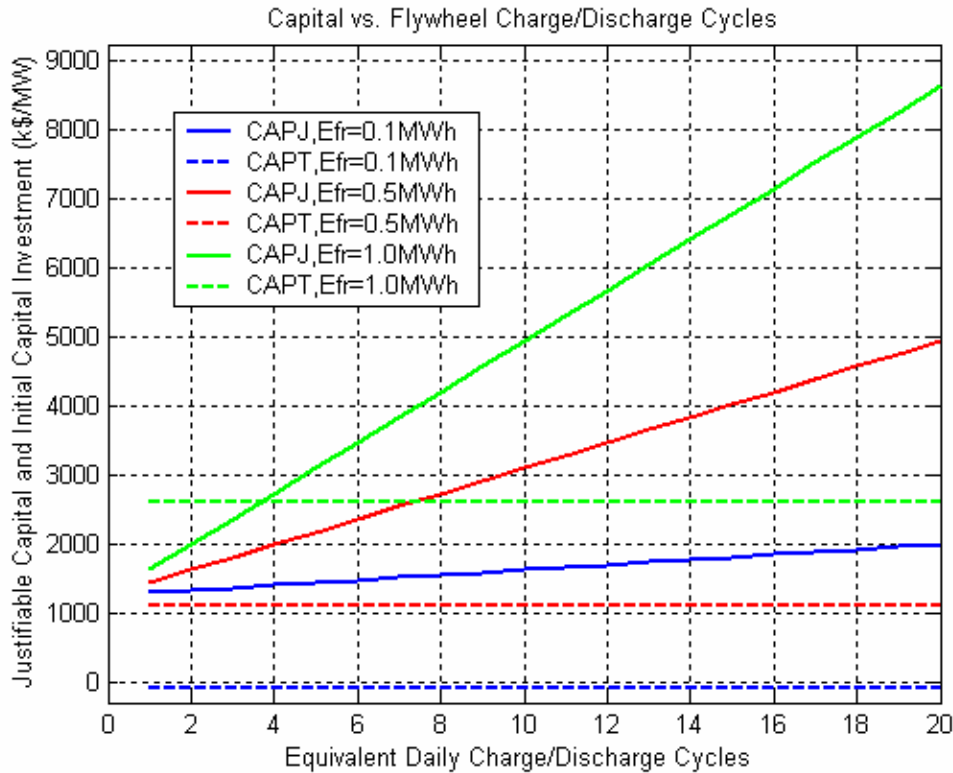


Figure 16-3: Justifiable Capital and Initial Capital Investment Depending on n_{fr}

16.1.3 Peak Power Buffer

As a peak power buffer, the flywheel batteries limit the maximum power drawn from the utility or a specified line. The flywheel thus supplies the peak power while the baseline power is supplied by the utility. By reducing the peak power drawn from the utility the power charged to the entity is limited. A simple example of where the peak power can be utilized is for supplying the initial turn on power for industrial motors.

The economics of the peak power buffer are found by comparing the cost of energy with the flywheel batteries and without them. The yearly flywheel operating cost per MW is

$$C_{fy} = 365 \left(\frac{n_{pk} E_{pk}}{\eta_{mg}^2} + t_d P_{fi} \right) d_f + C_{fm} \quad (16-10),$$

where n_{pk} is the average equivalent charge/discharge cycles during a day, E_{pk} is the storage capacity of the flywheel in MWh, η_{mg} is the motor/generator efficiency, P_{fi} is the idling power of the flywheel as a fraction of the MW rating, t_d is the average time in a day hours that peak power functions, d_f is the flywheel's energy cost in \$/MWh, and C_{fm} is the yearly maintenance cost of the flywheel in \$. The normal yearly cost of energy per MW beyond the baseline power is

$$C_{ey} = 365 P_{pk} t_c d_e \quad (16-11),$$

where P_{pk} is the power that exceeds the baseline power in MW (1 MW for calculations), t_c is the time period in hours for which the entity is charged this peak power rate, and d_e is the utility energy cost of the peak power in \$/MWh. The profit per year, C_{ypk} , for each installed MW of peak power buffer is

$$C_{ypk} = C_{ey} - C_{fy} \quad (16-12).$$

Due to flexibility in the charging of the flywheel, d_f in Equation 16-10 will generally be less than d_e in Figure 16-11.

To gain a rough understanding of the economic feasibility of the flywheel as a peak power buffer, the estimates in Table 16-3 are used.

η_{mg}	0.97	C_{fm}	\$5,000
t_d	24 hr	d_e	85 \$/MWh
P_{fi}	0.002* E_{fr}	t_c	24 hr
d_f	85 \$/MWh		

Table 16-3: Estimates for Rough Economic Feasibility of Peak Power Buffer

For these estimates Figure 16-4 and Figure 16-5 show justifiable capital, CAP_J , and initial capital cost, CAP_T , for variations in E_{pk} and n_{pk} respectively.

Figure 16-4 and Figure 16-5 show that the flywheel is profitable as a peak power buffer. In this application low energy capacity, E_{pk} , and equivalent daily cycles, n_{pk} , yield better profitability. If the cost for flywheel energy capacity decreases, the relation between E_{pk} , n_{pk} , and yearly profit will change significantly and the analysis should be redone. This analysis also assumes that both d_e and d_f are the same, but due to the flywheels ability to charge during off peak hours the additional cost savings and profit are possible.

An additional benefit of the peak power buffer is that it also serves to prevent power use above an entities scheduled rate. If an entity uses power beyond the scheduled rate, the penalty cost is typically twice the normal rate and is charged for the entire contracted period. By preventing these penalty charges the flywheel gains additional profitability.

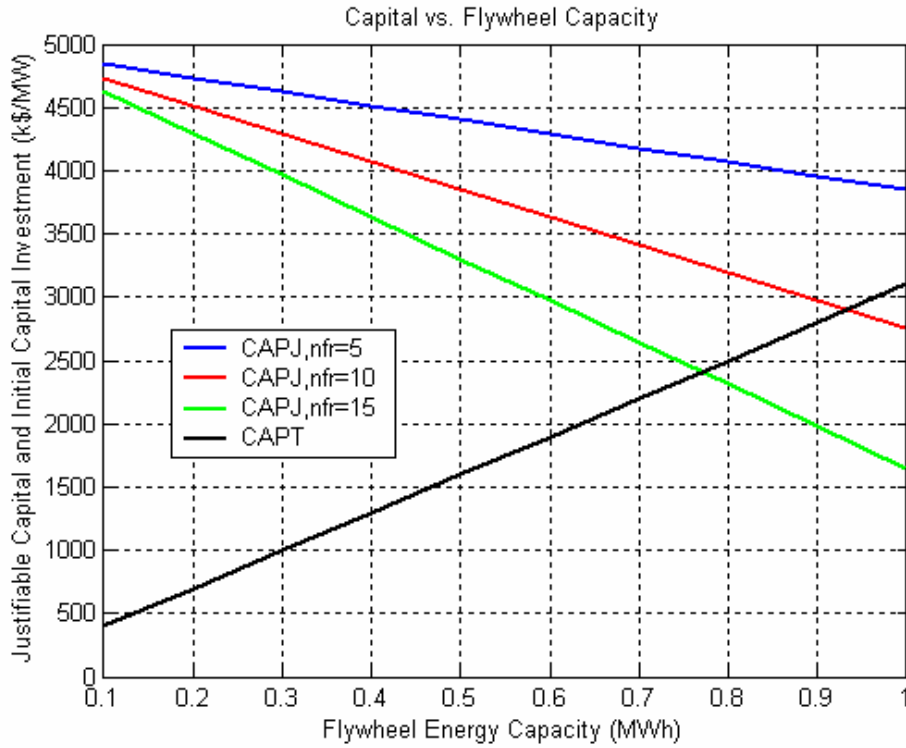


Figure 16-4: Justifiable Capital and Initial Capital Investment Depending on E_{pk}

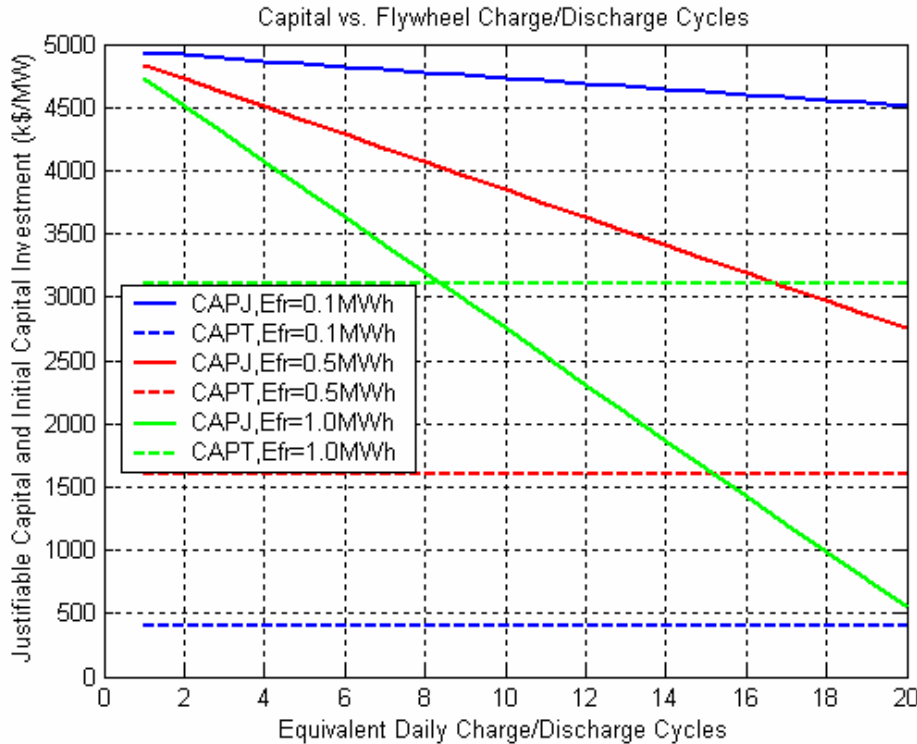


Figure 16-5: Justifiable Capital and Initial Capital Investment Depending on n_{pk}

16.1.4 Pollution Credit

The pollution credit is only covered briefly. This credit is based on the flywheel battery enabling the generation source to operate near its optimal efficiency and thus reduce emissions. The flywheel thus provides a buffer between the required output power and the optimal generating power. The profit for the pollution credit is derived from either avoiding emission (pollution) penalties or preventing the installation of emission control equipment to the generation source. Since this credit is highly dependent on the generation source, the economics need to be examined individually for each specific generation problem. More information on pollution credit can be found in reference [15].

16.1.5 Transmission Credit and Load Leveling Credit

The load leveling credit is examined first since it relates to the deviation of the transmission credit. For load leveling energy is purchased (flywheel is charged) during off-peak hours and the energy is sold (flywheel is discharged) during peak hours. The load leveling credit is determined by the difference in energy cost between peak and off-peak hours. In depth analysis of the load leveling credit is found in reference [15]. The conclusions in this reference are that to be profitable a very large and affordable energy capacity is required or the difference in price between peak and off-peak has to be extremely large. Since the peak to off-peak price difference is unlikely to change by magnitudes, a very significant decrease in the cost of the energy capacity is required to make the load leveling viable. This is not likely to happen in the near future making load leveling an unlikely application for flywheel batteries.

For the transmission credit the flywheel is utilized to decrease the maximum power of a transmission line. The flywheel batteries are located near the load in this application. During off-peak hours when the transmission line power is low the flywheel charges, and during peak hours the flywheel discharges to the load so that the maximum power of the transmission line is reduced. The flywheel batteries thus utilize the transmission line more effectively, and prevent the need to build new transmission lines. The efficiency of the energy transfer across the transmission line is also improved due to the I₂R losses of the line. When these abilities are combined with the flywheel's capability to provide voltage support, supply reactive power, and improve stability, a transmission line's power transferring capability is substantially improved.

While the transmission application requires large energy capacity, similar to the load leveling, the high cost of this energy capacity is offset by the high cost of building new transmission lines. Additional profit, beyond the cost of the transmission line, is also possible by utilizing the possible profits from load leveling and more efficient power transfer. While decreases in the flywheel energy capacity are required to enable the transmission application, the high cost and increased demand for new transmission makes the necessary improvement significantly less than for load leveling applications.

For transmission applications the power to energy ratio is extremely low. For current large capacity flywheels the maximum energy capacity is 100 kWh. In transmission applications the desired continuous power for a 100 kWh flywheel is in the range of 10 kW to 20 kW. This is considerably lower than the design in this paper. Thus the low power motor/generator design discussed in Section 14.6 is most applicable for transmission applications. If the motor/generator is able to operate in a vacuum, as discussed in Section 14.6, it will also further the flywheel's design and further reduce windage loss.

16.2 Flywheel Economics for Wind Applications

The main objective of this project was to investigate the possibility of making wind energy dispatchable through the use of inertial storage. In such a situation a wind system would be able to provide a base power for an entire day, and thus the wind system would be able bid for energy production similar to other types of generation. However, the needed energy capacity to supply the base power for an entire day is too large. Instead, a hybrid wind system is considered in which a gas turbine is combined with the wind generators and flywheel batteries.

In addition to a dispatchable hybrid wind system, the flywheel is also examined as an energy buffer for wind energy. With the energy buffer the wind system is capable of generating a constant power for hourly periods. The magnitude of the generation for each hour is derived from forecasting done prior to each hourly period (likely between 15 minutes to four hours prior, depending on forecasting capabilities).

The energy buffer enabling this type of operation provides three significant advantages. The first is that generation scheduling in a power system containing wind generation becomes more reliable due to the wind power being both constant and known for each hourly period. The second advantage is that, if accurate wind forecasting can be done for three to four hours in advance, low cost generation sources, such as coal-fired plants, can supplement the wind systems generation instead of higher cost generation such as gas turbines. The last and most important advantage is that, due to the combination of both higher reliability and lower cost supplemental generation, it is possible to increase the total percentage of power generation allotted to wind in a power system.

16.2.1 Hybrid Wind System: Power and Energy Sizing

Before the economics of a hybrid wind system are analyzed, the power rating of the gas turbine, and the power rating and energy capacity of the flywheel batteries need to be determined. To determine this sizing a 100 MW wind system is considered using wind data collected from a wind site near Buffalo Ridge, MN.

Since the goal of the hybrid wind system is to maximize the amount of wind generation, a gas turbine with a smaller rating the wind generation is desired. A gas turbine with the same rating as the wind generation could be utilized, but this situation is no different than the current generation systems except that the gas turbine is located near the wind generation (this could be an advantage or disadvantage). Half the wind system rating (50 MW) is selected as the gas turbine power rating for this analysis. For this gas turbine it is also assumed that the generator startup time is 10 minutes and that its maximum efficiency occurs at 60% of its rated power.

To minimize fuel consumption the hybrid system operates the gas turbine at its maximum efficiency power whenever possible. By avoiding idle or low generation levels (minimum power level is 5 MW) the fuel consumption is also improved. In addition to avoid frequent startup and shutdown conditions (which waste fuel), a minimum run time of 30 minutes is also established.

For the flywheel batteries the energy capacity of each wheel is assumed to be 100 kWh. To find the necessary energy capacity and power rating of the flywheel batteries 25 (2.5 MWh), 50 (5 MWh), 100 (10 MWh), and 200 (20 MWh) flywheels are analyzed.

Figures 16-6 thru 16-9 show the hybrid power levels for six different days for both 25 and 100 flywheel batteries. In these figures the following are shown: the hybrid system's base power

bounds (UB (+10%) and LB (-10%) of base power level), the hybrid systems output power (HP), generated wind power (WP), gas turbine power (GP), and flywheel power (FP).

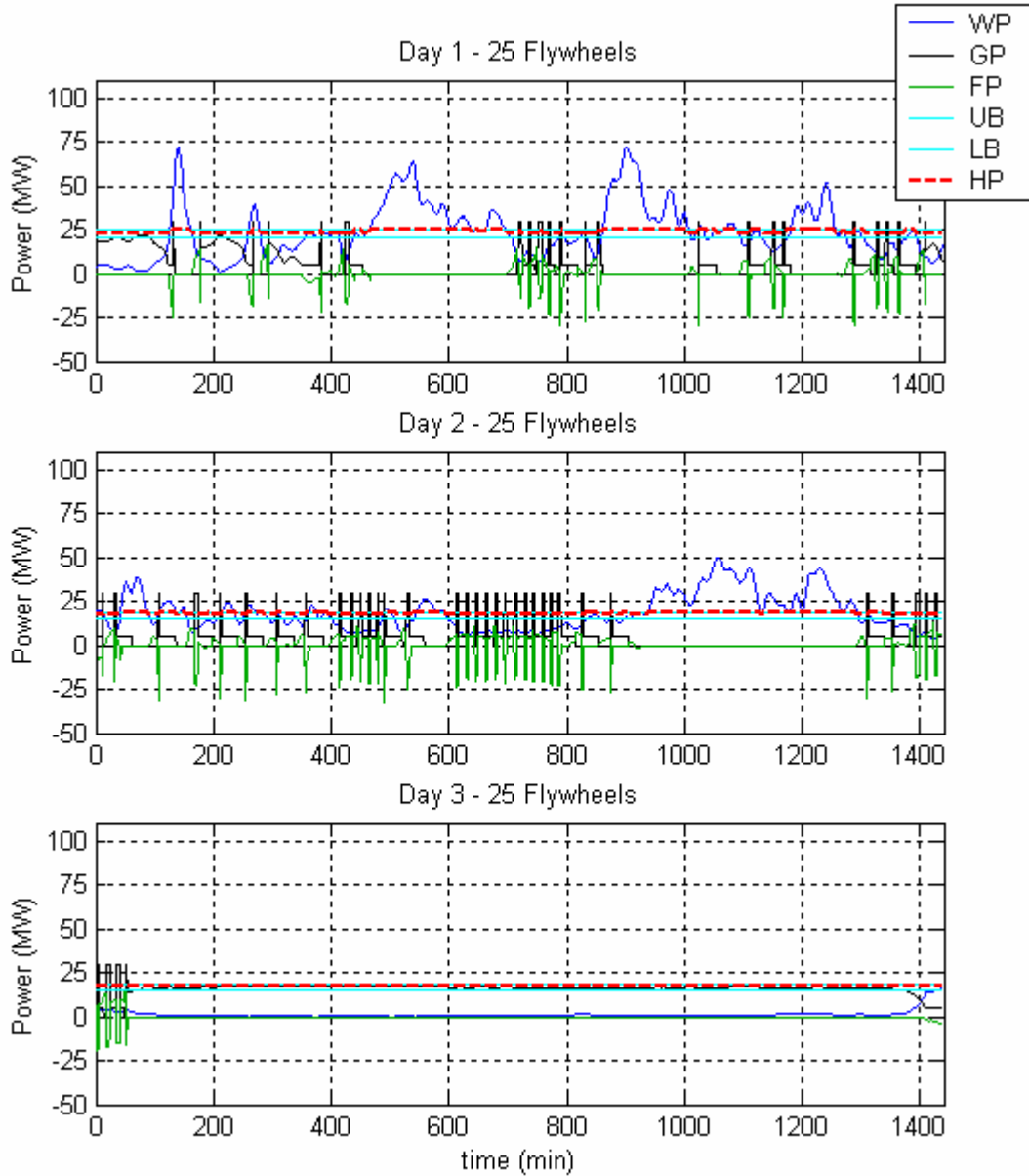


Figure 16-6: Hybrid Wind System Power for Days 1 to 3 for 25 Flywheels

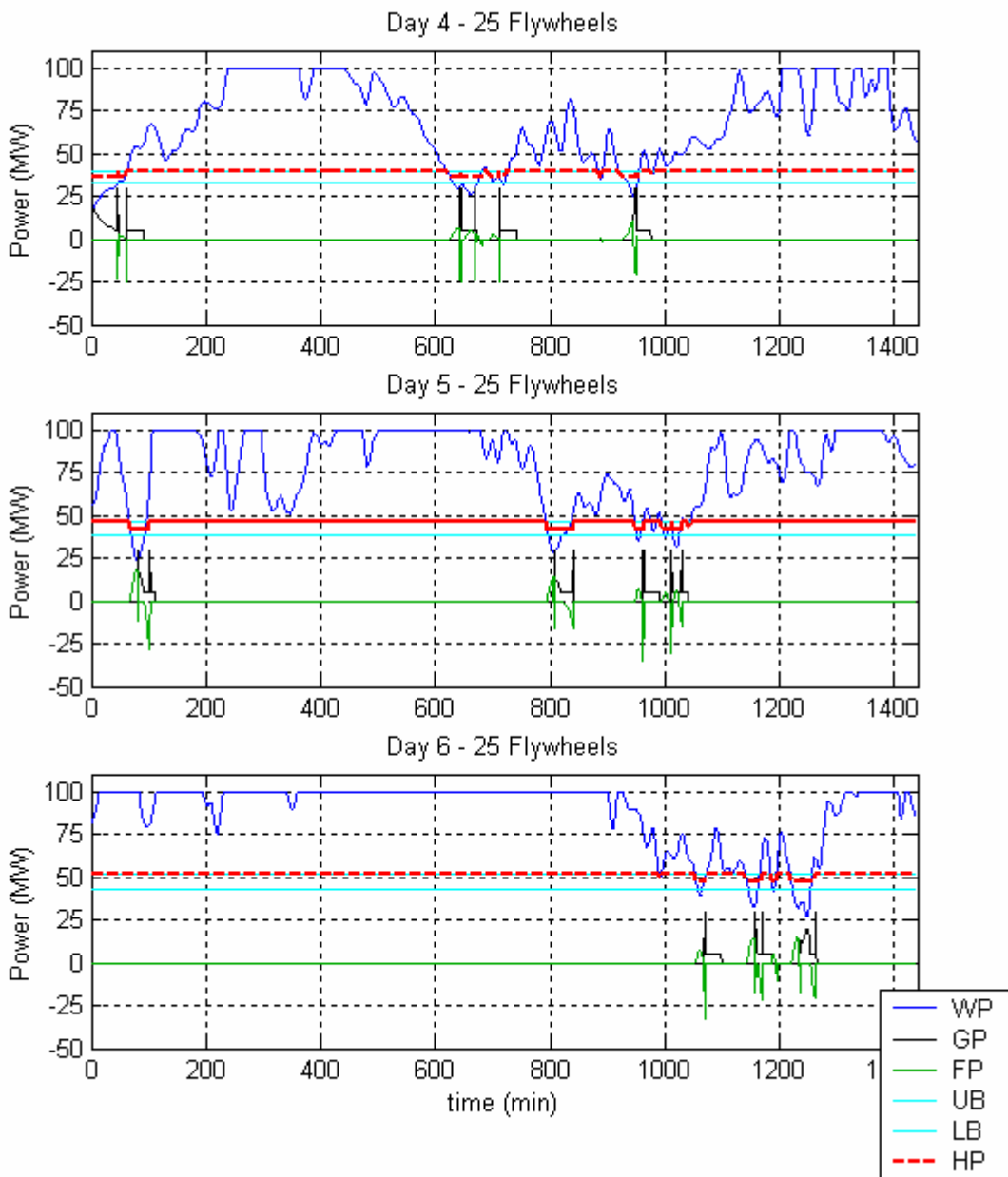


Figure 16-7: Hybrid Wind System Power for Days 4 to 6 for 25 Flywheels

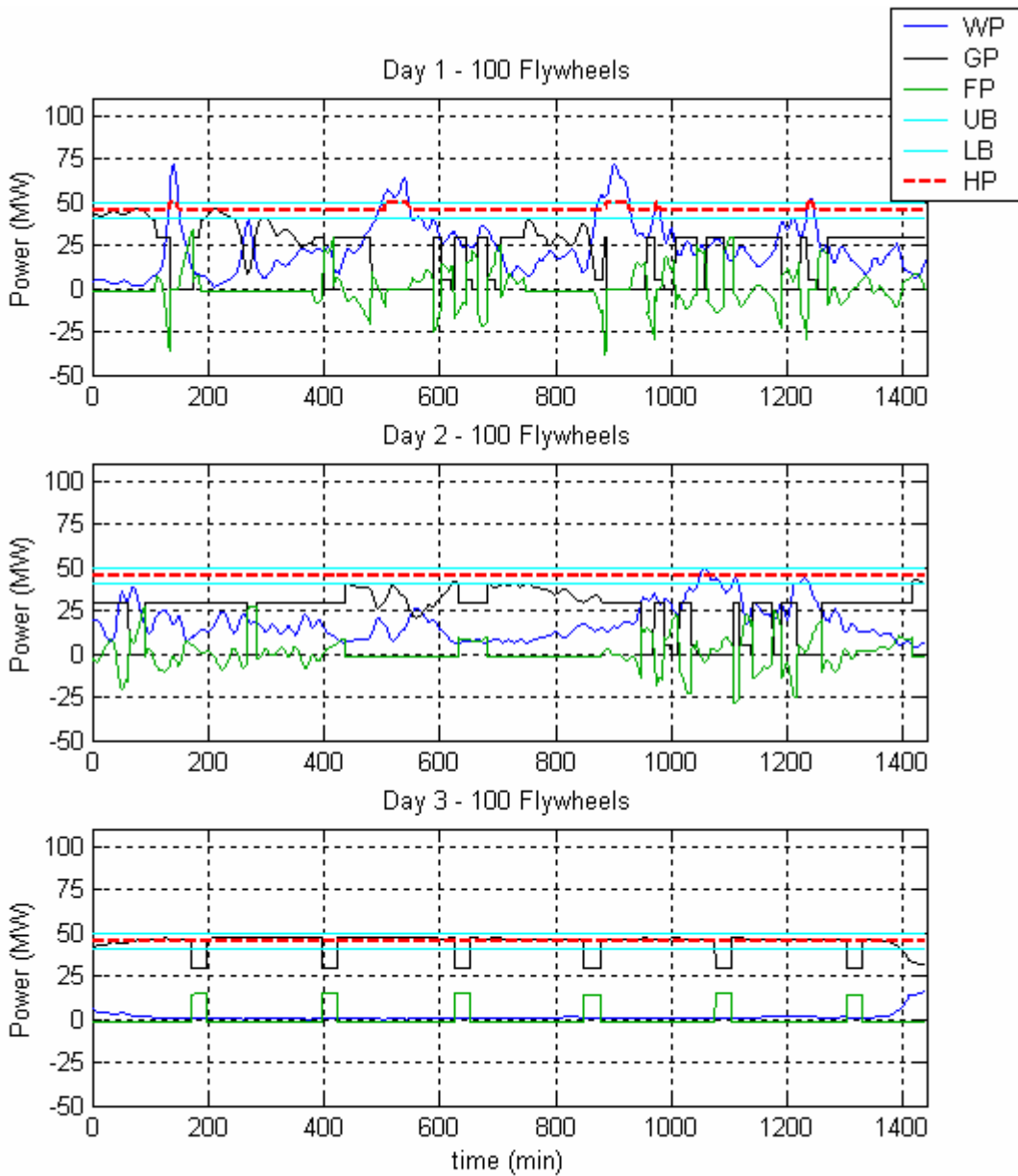


Figure 16-8: Hybrid Wind System Power for Days 1 to 3 for 100 Flywheels

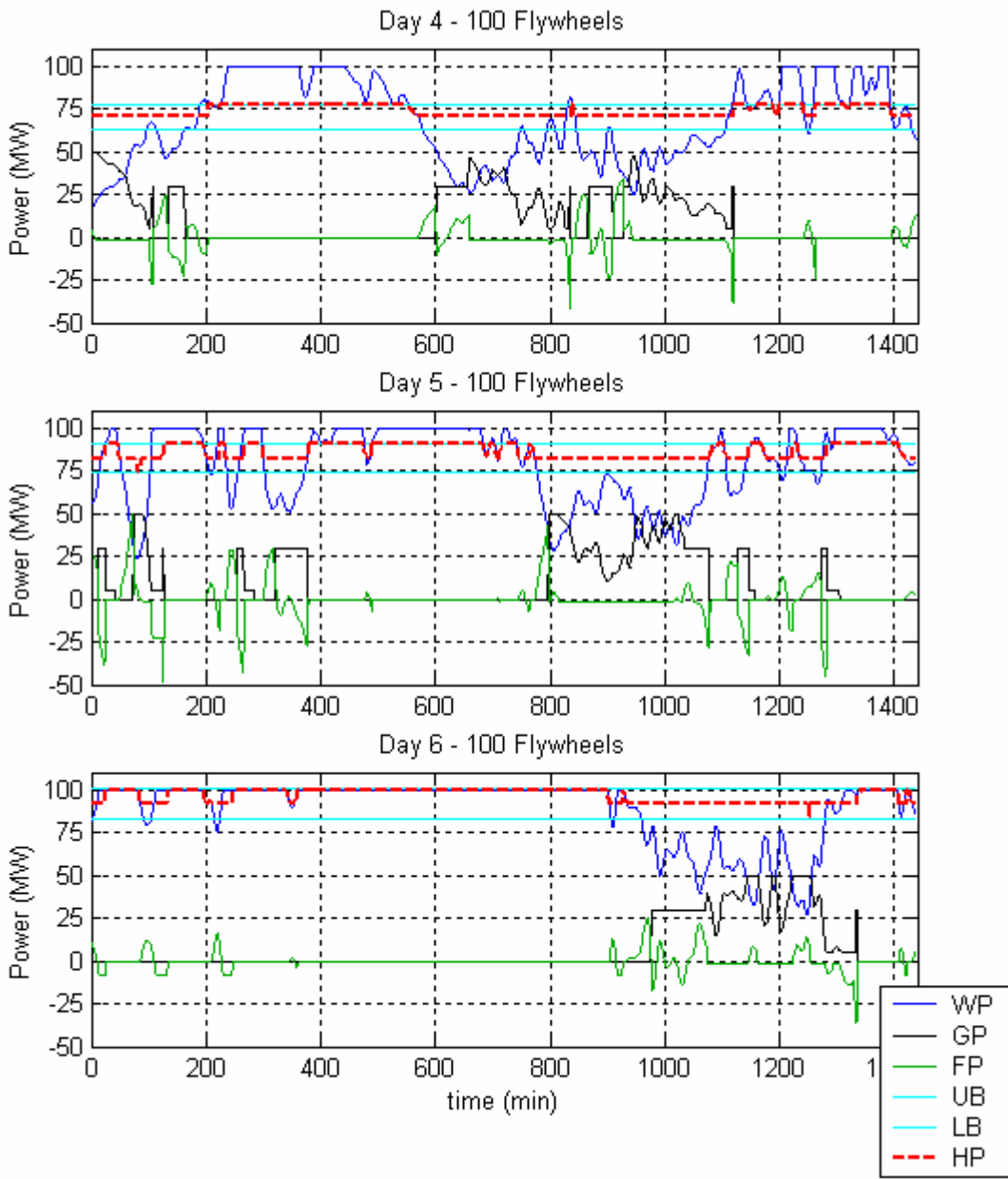


Figure 16-9: Hybrid Wind System Power for Days 4 to 6 for 100 Flywheels

The base power level for the hybrid system is derived from the maximum value of either: the maximum wind power during the day multiplied by a constant (days 1 and 4), the average wind power during the day multiplied by a constant (days 5 and 6), or a minimum power level (days 2 and 3). The constants and the minimum power level are increased as the number of flywheel batteries increases. If the base power level is based on the maximum or average power, the hybrid system acts more like a wind system and accurate wind forecasting for the day becomes important. If the base power level is the minimum power level, the hybrid system acts similar to gas turbine generation except that the wind generation and flywheel batteries reduce fuel consumption.

The wind generation in Figures 16-6 thru 16-9 is either within, less than, or greater than the base power level bounds. If the power is within the bounds, only wind generation occurs. When the wind generation is less than the bounds, either the flywheel batteries discharge and or the gas turbine generates power. If the wind generation is greater than the bounds, the flywheel batteries charge. When the flywheel batteries' capacity is exceeded, the excess wind power needs to be dissipated. For wind system this is accomplished by pitching the wind turbines to decrease the output power. Obviously this wastes power, but there is little choice and is an advantage using more flywheels.

To compare the performance of the different number of flywheel batteries three different 30 day data sets, like those in Figures 16-6 thru 16-9 are analyzed. The results are shown in Tables 16-4 thru 16-6. The hybrid wind system is set up to minimize generation power levels below the lower bound. This results in more dissipated wind power (or more power over the upper base power bound), but the penalties charged to generation sources that violate the base power bounds are too substantial to not set up the system this way.

Fore-casting Error (%)	# of fly-wheels	Total energy exceeding lower bound	Total energy exceeding upper bound	Total wind energy output to grid	Total hybrid system energy output to grid	GT energy generated at 10% of optimal efficiency	GT energy generated at greater than 40% rated power
		(kWh)	(kWh)	(kWh)	(kWh)	(kWh)	(kWh)
0	25	0.0	5553.8	10503.4	17100.8	864.4	1511.6
	50	0.0	1408.5	14649.5	31592.9	7175.0	16240.7
	100	0.0	1102.3	14956.7	36758.0	5875.2	21592.7
	200	0.0	994.8	15061.8	39428.0	6459.1	24350.7
-10	25	0.1	6282.4	9774.9	15442.0	780.8	1298.4
	50	0.0	2087.7	13971.0	28551.4	10892.5	13907.5
	100	0.0	1710.8	14346.9	33203.4	6961.1	18665.9
	200	0.0	1531.8	14524.8	38260.1	6712.8	6712.8
+10	25	1.2	4864.4	11192.8	18755.2	865.8	1816.4
	50	20.2	919.6	15136.3	34474.5	5030.4	18746.4
	100	27.2	729.0	15330.0	40097.9	4412.9	24517.8
	200	25.5	666.0	15390.6	40439.0	6385.0	25015.0

Table 16-4: Hybrid Wind System Results for Data Set 1

Fore-casting Error (%)	# of fly-wheels	Total energy exceeding lower bound	Total energy exceeding upper bound	Total wind energy output to grid	Total hybrid system energy output to grid	GT energy generated at 10% of optimal efficiency	GT energy generated at greater than 40% rated power
		(kWh)	(kWh)	(kWh)	(kWh)	(kWh)	(kWh)
0	25	0.2	5766.6	12141.2	17493.1	726.0	1740.8
	50	0.0	1972.3	15934.3	31221.5	7218.2	14422.4
	100	0.0	1636.7	16267.4	35579.6	7487.4	19037.1
	200	0.0	1450.5	16448.6	38000.3	8879.5	21531.2
-10	25	0.4	6546.2	11361.6	15811.3	594.9	876.8
	50	0.1	2587.8	15318.7	28204.7	8333.7	12034.5
	100	0.0	2169.9	15734.1	32108.3	8727.7	16122.4
	200	0.0	1832.4	16066.6	36853.7	9029.9	20771.6
+10	25	2.1	5073.8	12834.0	19159.1	880.7	2365.3
	50	5.5	1448.9	16457.7	34194.8	6310.0	16974.7
	100	5.3	1190.7	16713.3	39001.5	6135.4	22020.9
	200	5.3	1101.2	16797.8	39291.2	8657.6	22457.0

Table 16-5: Hybrid Wind System Results for Data Set 2

Forecasting Error (%)	# of fly-wheels	Total energy exceeding lower bound	Total energy exceeding upper bound	Total wind energy output to grid	Total hybrid system energy output to grid	GT energy generated at 10% of optimal efficiency	GT energy generated at greater than 40% rated power
		(kWh)	(kWh)	(kWh)	(kWh)	(kWh)	(kWh)
0	25	0.9	2960.1	9027.7	15373.4	915.6	1353.3
	50	0.7	846.9	11141.7	28519.4	8911.0	16689.2
	100	0.0	655.1	11333.8	34120.8	7305.8	22611.5
	200	0.0	599.6	11391.8	37002.5	8526.5	25602.0
-10	25	1.1	3305.2	8682.5	14635.5	698.9	1022.4
	50	0.3	1069.2	10919.1	27615.7	9036.8	15988.8
	100	0.0	845.0	11144.4	33340.4	7507.9	22037.6
	200	0.0	775.8	11213.1	36209.6	8734.0	24988.2
+10	25	1.2	2628.6	9359.2	16130.1	938.9	1639.8
	50	15.5	622.9	11364.7	29600.9	8695.7	17551.6
	100	17.5	484.3	11503.0	34845.7	6812.9	23135.2
	200	16.3	440.7	11551.4	37731.8	8154.9	26164.5

Table 16-6: Hybrid wind system results for data set 3

In Tables 16-4 thru 16-6 as the storage increases the performance of the hybrid system also increases. This performance includes a decrease in the dissipated wind energy, an increase in total system output, and in an increase in higher efficiency gas turbine operation. The tables also show only a marginal performance gains when increasing from 50 to 100 flywheels or from 100 to 200 flywheels. It can be concluded that the desired number of flywheels per 100 MW of wind generation for this site (with 50 MW of gas turbine generation) is between 50 and 100.

Tables 16-4 thru 16-6 indicate how the performance changes with forecasting errors of +/-10%. As expected a larger number of flywheel batteries handle this error better. An exception to this is the amount of energy (or penalty power) under the lower bound for the 25 flywheel setup in the +10% case. This result is deceiving and is only the case due to the initially lower power base (or initially expected low performance of 25 flywheels).

For all three data sets the total peak power from the flywheel batteries is around 50 MW regardless of the number of flywheels. The continuous power rating of the flywheel batteries is 20 MW, 25 MW, 28 MW, and 30 MW for 25, 50, 100, and 200 flywheel batteries respectively. These rating again point to the use of flywheel designs with fairly low power to energy ratios. For the 50 flywheel batteries for example, a more appropriate motor/generator is one that has a peak power of 1 MW and is optimized for continuous power and low rotor loss at 500 kW or less.

16.2.2 Economics of Hybrid Wind System

For 100 kWh flywheels, somewhere between 50 and 100 flywheel batteries appear to give the best combination of low cost and high performance for 100 MW of generation and 50 MW of gas turbine generation. Using previously defined estimates; the initial capital investment for the hybrid wind system is approximately \$45 million (\$20 million for flywheels and \$25 million for gas turbine).

Due to the current leniency wind system are granted in their generation, this extra cost is difficult to justify. Since the hybrid wind system requires pitching of the wind turbine blade at times, it also does not maximize the production of wind energy. The cost of gas turbine generation used in the hybrid system is also high compared to other generation sources. This higher cost is usually justified by the gas turbine providing regulatory services, but for the hybrid wind system

only functions to provide a base power. Due to these factors, the hybrid wind system is practical only if wind systems are required to be dispatchable.

16.2.3 Energy Buffer for Wind Systems: Power and Energy Sizing

The goal for the energy buffer is to maintain the output of a wind system at a constant power during time periods of an hour. To determine the required power rating and energy capacity of the energy buffer a similar analysis as that for the hybrid wind system is considered using the same 100 MW wind system and 100 kWh flywheels. The analysis includes results for 25, 50, 100, 200, and 250 flywheel batteries.

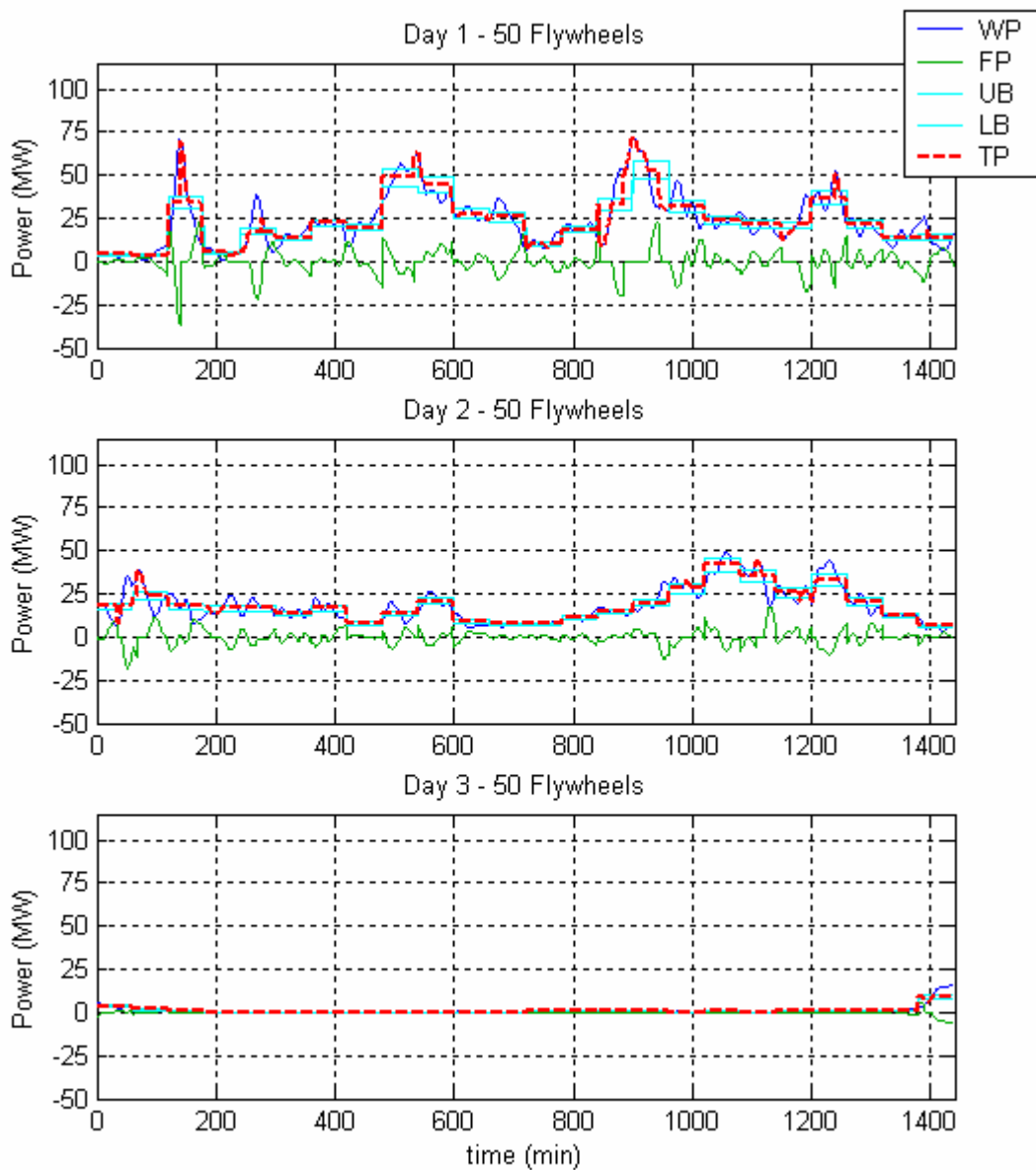


Figure 16-10: Wind system power with energy buffer for days 1 to 3 for 50 flywheels

Figures 16-10 thru 16-13 show the power levels for six different days for both 50 and 200 flywheel batteries. In these figures the following are shown: the wind system's base power bounds (UB (+10%) and LB (-10%) of base power level), the total output power of the wind system and flywheel (TP), generated wind power (WP), and flywheel power (FP). Forecasting determines the base power level that is communicated to the power system dispatcher. In Figures 16-6 thru 16-9 the power level transitions in step increments between hours. In a real power systems these transition would be smooth coordinated transitions.

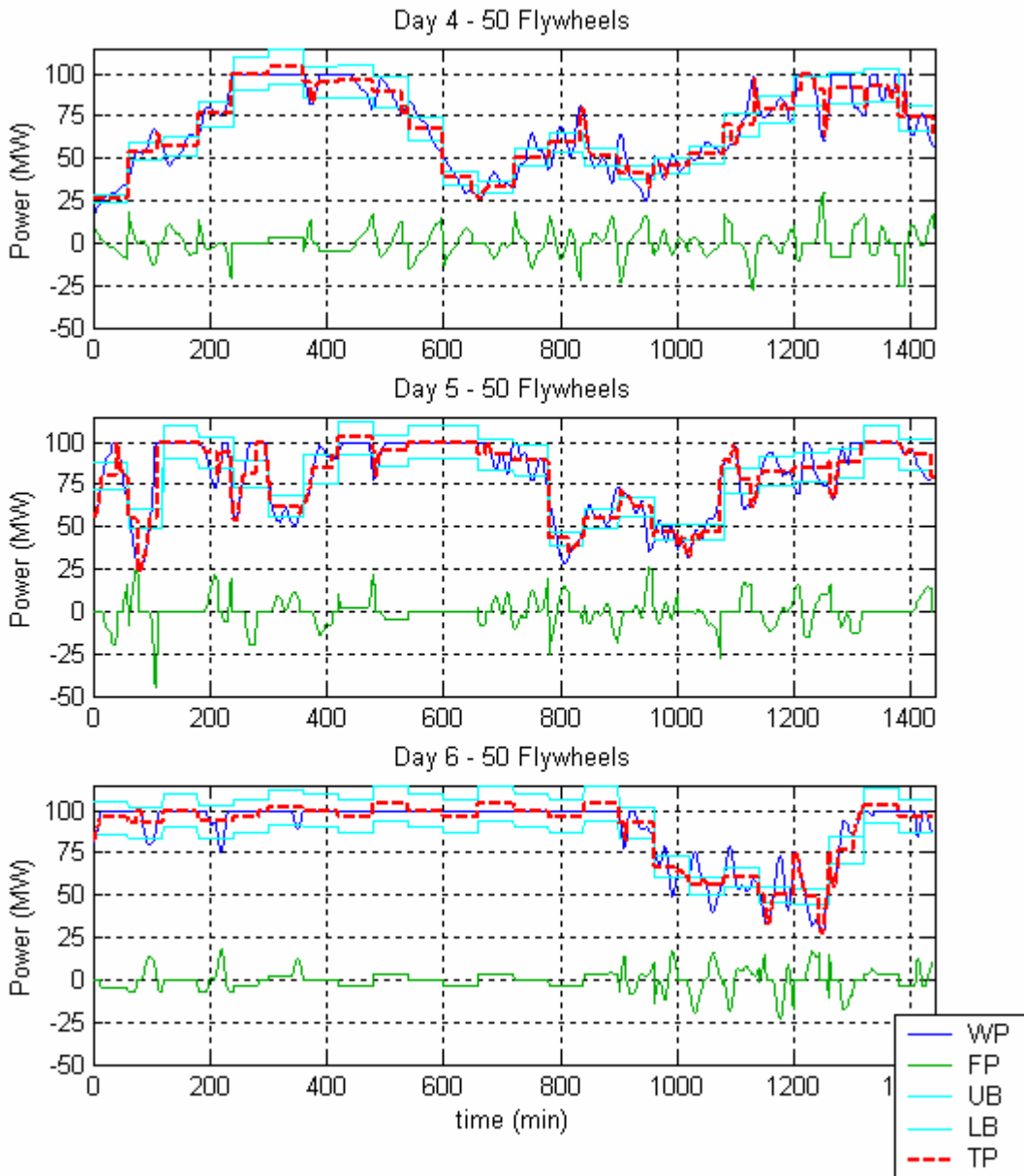


Figure 16-11: Wind system power with energy buffer for days 4 to 6 for 50 flywheels

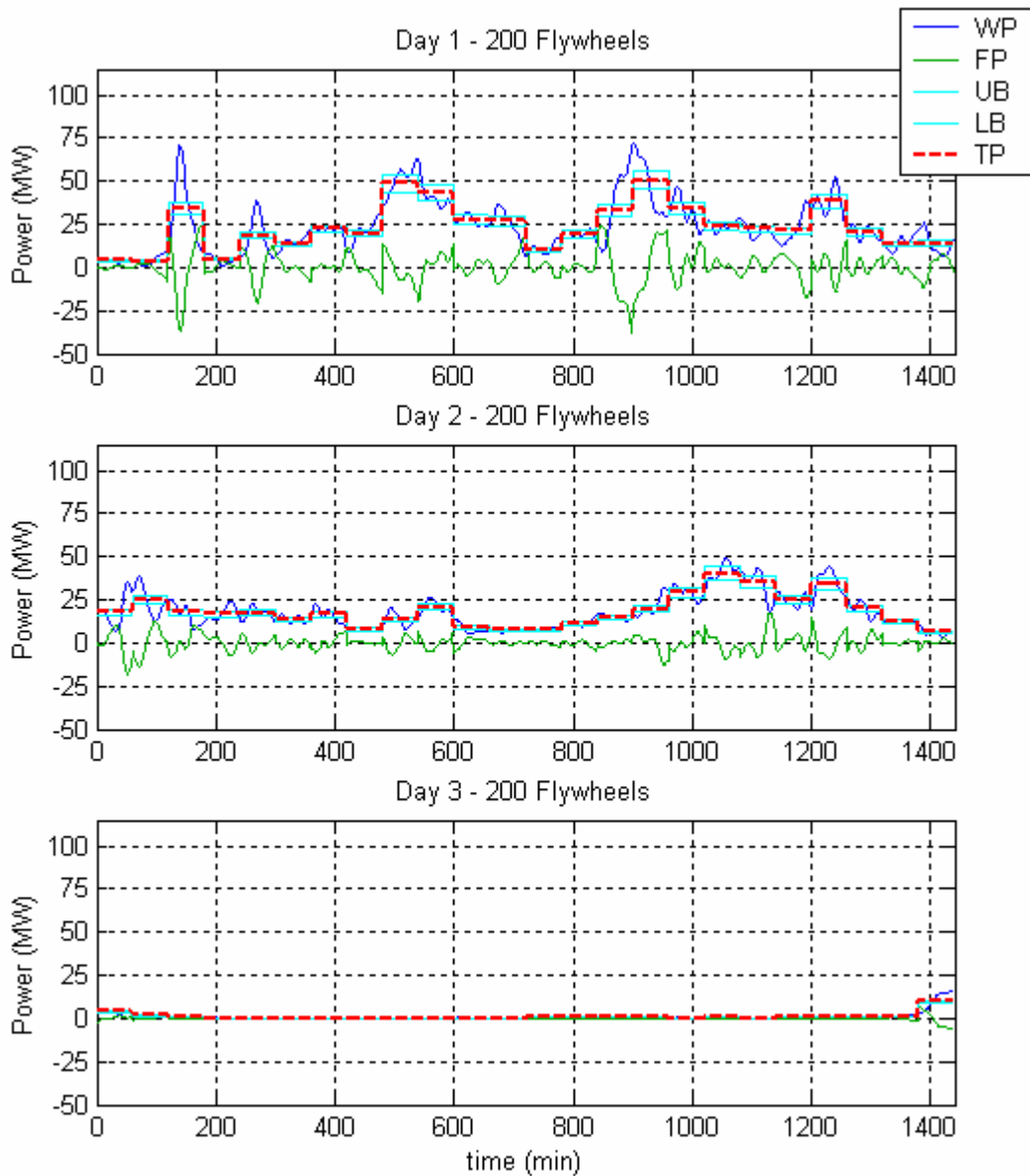


Figure 16-12: Wind system power with energy buffer for days 1 to 3 for 200 flywheels

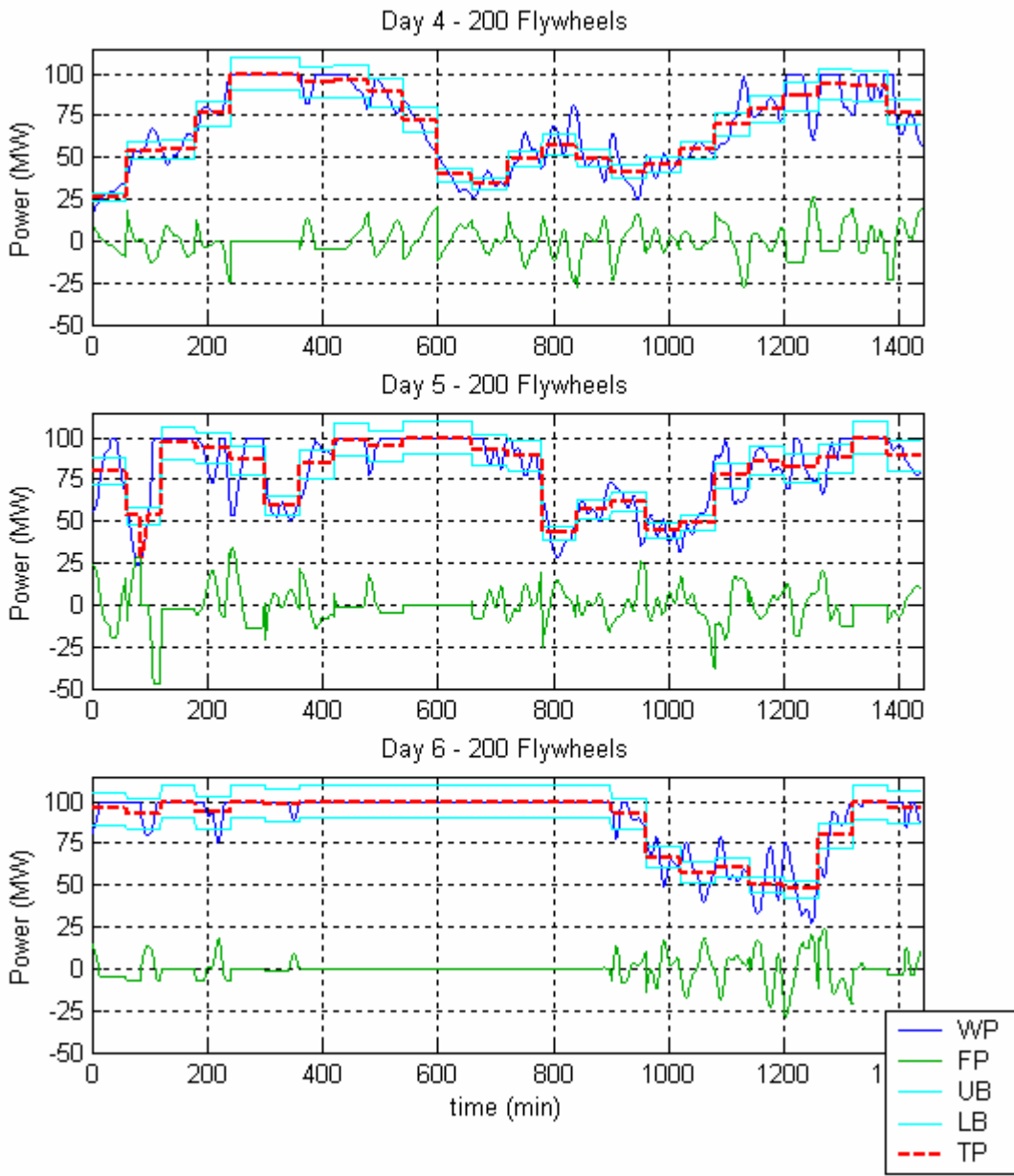


Figure 16-13: Wind system power with energy buffer for days 4 to 6 for 200 flywheels

To compare the performance of different numbers of flywheel batteries three different 30 day data sets, like those in Figures 16-10 thru 16-13 are analyzed. The results are shown in Tables 16-7 thru 16-9. For each size of flywheel two methods are used for to determine base power level. Method (a) uses the average of the power over the hour. Method (b) also uses the average, but in addition the desired output power is modified based on the flywheel's state of charge 15 minutes prior to a new hour time period. While method (b) introduces some last minute adjustment,, the adjustment is less than 3% of the value derived from method (a). The low value of the adjustment combined with the 15 minutes of preparation should make method (b) viable in real power systems.

Forecast error	# of fly-wheels	Method (a)					Method (b)				
		Total energy exceeding lower bound	Lower bound errors	Total energy exceeding upper bound	Upper bound errors	Days with no errors	Total energy exceeding lower bound	Lower bound errors	Total energy exceeding upper bound	Upper bound errors	Days with no errors
		(kWh)	(#)	(kWh)	(#)	(#)	(kWh)	(#)	(kWh)	(#)	(#)
0%	0	487.0	815	504.5	827	0	487.0	815	504.5	827	0
	25	203.8	221	195.8	164	5	201.2	220	196.6	164	4
	50	110.4	126	102.8	68	7	103.0	96	103.2	69	7
	100	31.5	32	28.8	15	17	28.7	29	28.6	14	19
	200	4.1	1	5.2	6	25	3.1	2	1.7	1	28
	250	0.0	1	2.7	2	27	0.0	1	0.0	1	28
-10%	0	244.0	616	1105.1	916	0	244.0	616	1105.1	916	0
	25	47.1	48	860.9	562	0	50.5	55	77.4	556	0
	50	16.0	12	821.4	545	0	20.9	16	543.9	439	0
	100	3.0	1	806.4	534	0	3.8	1	620.7	485	0
	200	0.0	0	799.5	521	1	0.0	0	524.1	427	1
	250	0.0	0	797.8	511	1	0.0	0	529.3	425	2
+10%	0	940.0	897	246.9	615	0	940.0	897	246.9	615	0
	25	739.8	733	61.1	42	0	680.9	721	65.0	51	0
	50	707.8	724	272.0	11	0	475.5	606	33.9	20	0
	100	692.3	719	7.1	3	0	545.8	661	7.8	3	0
	200	682.3	701	0.0	0	0	452.6	595	0.0	0	1
	250	680.7	688	0.0	0	1	455.1	584	0.0	0	2
Random Set A	0	524.4	793	561.3	813	0	524.4	793	561.3	813	0
	25	249.8	247	259.4	184	1	245.2	234	256.7	185	2
	50	167.2	134	167.1	102	8	152.3	116	160.7	100	7
	100	84.0	78	82.8	54	11	70.3	68	72.9	44	11
	200	38.6	26	30.9	27	17	24.1	16	11.7	11	21
	250	29.6	17	23.4	19	21	21.2	16	14.2	14	21
Random Set B	0	519.6	807	563.0	800	0	519.6	807	563.0	800	0
	25	245.0	274	255.9	205	1	240.2	264	254.1	206	1
	50	151.5	143	156.4	107	6	144.1	118	148.0	96	8
	100	72.1	77	74.4	62	11	62.9	63	62.9	53	12
	200	31.0	36	32.9	32	13	17.6	24	13.8	9	20
	250	18.9	25	21.7	25	16	14.6	19	8.5	9	19
Random Set C	0	513.7	803	561.9	814	0	513.7	803	561.9	814	0
	25	241.0	277	267.4	205	2	236.4	258	266.4	199	2
	50	150.3	179	16.8	101	5	141.9	145	16.8	97	6
	100	67.7	88	74.6	56	7	58.3	69	67.0	49	9
	200	21.9	26	30.7	34	13	13.5	16	6.3	8	20
	250	14.2	15	21.7	29	16	7.2	10	7.6	8	21

Table 16-4: Energy buffer results for data set 1

Forecast error	# of fly-wheels	Method (a)						Method (b)					
		Total energy exceeding lower bound	Lower bound errors	Total energy exceeding upper bound	Upper bound errors	Days with no errors	Total energy exceeding lower bound	Lower bound errors	Total energy exceeding upper bound	Upper bound errors	Days with no errors		
		(kWh)	(#)	(kWh)	(#)	(#)	(kWh)	(#)	(kWh)	(#)	(#)		
0%	0	563.2	803	573.2	842	0	563.2	803	573.2	842	0		
	25	231.2	273	217.3	200	0	227.0	265	216.1	202	0		
	50	115.2	158	35.2	91	1	103.5	106	101.0	90	2		
	100	34.4	45	25.5	32	11	28.6	27	18.9	29	13		
	200	0.0	0	1.5	6	25	1.1	3	0.5	2	26		
	250	0.0	0	1.1	4	26	0.0	0	0.0	0	30		
-10%	0	274.2	559	1285.9	974	0	274.2	559	1285.9	974	0		
	25	66.5	47	1023.0	710	0	70.0	52	929.7	697	0		
	50	16.6	13	962.8	693	0	23.9	20	646.1	615	0		
	100	0.0	1	942.1	688	0	0.7	2	733.2	633	0		
	200	0.0	0	938.8	686	0	0.0	0	622.4	596	0		
	250	0.0	0	937.3	684	1	0.0	0	626.0	596	1		
+10%	0	1098.3	947	260.8	564	0	1098.3	947	260.8	564	0		
	25	876.1	819	61.4	59	0	804.5	796	66.3	63	0		
	50	833.5	806	18.2	16	0	556.1	674	25.5	21	0		
	100	813.4	799	0.0	0	0	636.8	726	0.3	2	0		
	200	810.9	794	0.0	0	1	533.6	671	0.0	0	1		
	250	809.6	792	0.0	0	1	537.8	671	0.0	0	1		
Random Set A	0	602.3	797	626.8	813	0	602.3	797	626.8	813	0		
	25	282.7	286	268.8	255	0	277.1	275	271.0	254	0		
	50	159.8	170	142.9	136	2	146.5	139	143.6	126	2		
	100	76.6	89	60.4	71	4	61.0	63	48.3	58	4		
	200	38.2	41	24.8	25	12	9.9	17	6.0	9	19		
	250	29.0	32	10.7	16	17	11.0	17	3.5	7	18		
Random Set B	0	609.7	790	638.7	807	0	609.7	790	638.7	807	0		
	25	299.4	304	287.4	236	0	292.7	298	288.2	236	0		
	50	186.6	187	159.6	131	4	169.4	161	161.3	128	3		
	100	99.6	99	67.5	69	4	79.1	83	53.4	49	4		
	200	55.8	43	29.6	36	10	19.7	20	6.5	7	17		
	250	46.9	39	26.2	33	12	23.7	21	6.5	10	16		
Random Set C	0	591.0	800	653.5	823	0	591.0	800	653.5	823	0		
	25	275.0	325	304.3	264	0	266.9	312	302.5	264	0		
	50	156.0	200	168.6	152	1	140.5	133	165.9	148	3		
	100	71.3	84	23.4	67	5	58.2	65	58.6	59	5		
	200	27.9	36	27.4	34	12	11.3	14	9.6	17	17		
	250	22.3	28	18.4	24	15	7.2	12	6.5	12	17		

Table 16-5: Energy buffer results for data set 2

Forecast error	# of fly-wheels	Method (a)						Method (b)					
		Total energy exceeding lower bound	Lower bound errors	Total energy exceeding upper bound	Upper bound errors	Days with no errors	Total energy exceeding lower bound	Lower bound errors	Total energy exceeding upper bound	Upper bound errors	Days with no errors		
		(kWh)	(#)	(kWh)	(#)	(#)	(kWh)	(#)	(kWh)	(#)	(#)		
0%	0	472.3	869	497.8	827	0	472.3	869	497.8	827	0		
	25	154.8	232	154.5	157	2	150.7	214	153.7	156	2		
	50	69.8	97	71.7	58	6	59.8	70	66.1	65	9		
	100	23.2	25	18.6	21	16	17.0	16	15.9	18	19		
	200	0.0	0	2.6	4	26	1.8	1	1.1	2	27		
	250	0.0	0	1.2	4	26	0.0	0	0.0	0	30		
-10%	0	238.5	641	1009.6	962	0	238.5	641	1009.6	962	0		
	25	34.3	41	754.1	647	0	37.2	45	695.0	633	0		
	50	5.2	7	718.4	635	0	8.0	10	493.8	534	0		
	100	0.0	0	710.0	632	0	0.0	0	566.2	583	0		
	200	0.0	0	706.9	626	0	0.0	0	483.7	531	0		
	250	0.0	0	705.1	622	0	0.0	0	485.0	530	0		
+10%	0	884.6	962	244.5	597	0	884.6	962	244.5	597	0		
	25	665.4	817	42.0	41	0	612.3	797	447.6	46	0		
	50	632.4	806	13.2	7	0	419.9	666	16.9	13	0		
	100	619.8	799	0.4	2	0	486.7	734	0.9	2	0		
	200	616.1	793	0.0	0	0	406.5	676	0.0	0	0		
	250	614.7	790	0.0	0	0	410.9	678	0.0	0	0		
Random Set A	0	506.8	847	550.4	789	0	506.8	847	550.4	789	0		
	25	200.3	265	210.7	199	0	197.1	246	209.6	194	0		
	50	109.1	128	111.8	100	5	96.5	98	106.0	93	7		
	100	50.9	66	51.8	42	9	37.7	47	42.3	33	12		
	200	20.0	39	20.3	24	17	5.7	5	3.9	7	25		
	250	11.8	24	17.0	17	22	1.6	4	5.6	6	24		
Random Set B	0	517.2	840	527.9	820	0	517.2	840	527.9	820	0		
	25	207.7	272	193.6	205	0	204.0	262	192.8	209	0		
	50	116.6	135	100.7	97	6	101.7	117	96.5	95	6		
	100	56.9	69	40.7	42	8	46.2	59	37.9	36	12		
	200	17.0	32	5.9	10	21	11.7	9	7.7	4	23		
	250	11.5	20	2.9	7	23	3.4	6	1.3	3	25		
Random Set C	0	498.4	857	538.9	825	0	498.4	857	538.9	825	0		
	25	194.6	291	207.8	197	0	0.0	276	0.0	198	0		
	50	101.5	157	112.3	98	4	189.0	111	203.8	96	4		
	100	53.5	87	58.3	52	7	40.3	42	48.3	41	11		
	200	24.7	52	31.0	30	13	8.6	6	13.9	10	23		
	250	19.8	44	27.2	24	16	7.4	6	12.8	9	22		

Table 16-6: Energy buffer results for data set 3

The main objective of the energy buffer is to maintain the wind system's power generation within the power bounds. However, it may be more desirable to undershoot the forecasted projections as is done with the hybrid wind system in Section 16.2.1. Similar to the hybrid case power generation above the upper bound is dissipated by pitching the blades of the wind turbines. If the wind system is penalized for exceeding the bounds, this is the preferred operation, but if there are no penalty charges, accurate forecasts should be exploited to maximize wind energy generation.

In Tables 16-7 thru 16-9 six different sets of data are given. The first three sets assume forecast exactly at the hourly average, 90% of the hourly average, and at 110% of the hourly average. In addition three random sets of data are used in which the percentage of the hourly average fall at a random point between 90% and 110% of the hourly average. From the results in the tables, it is obvious that accurately forecasting the wind significantly increases the performance of the energy buffer. The time period before the base power level for each hour is forecasted should therefore be selected to achieve high accuracy. If it is possible to accurately forecast the wind power three to four hours in advance, it is especially beneficial since it enables the wind system to be coupled with slower low cost generation.

From Tables 16-7 thru 16-9 at least 100 flywheel batteries are required for 100 MW wind system that maintain constant power for hour periods, and 200 or more flywheels are preferable. Also, if accurate forecasting is possible and a small amount of undershooting is done of the base power level, 200 flywheel batteries will almost always remain above the lower bound.

For all three data sets the total peak power from the flywheel batteries is around 50 MW regardless of the number of flywheels. The continuous power rating of the flywheel batteries is 15 MW, 20 MW, 23 MW, 26 MW, and 28 MW for 25, 50, 100, 200, and 250 flywheel batteries respectively. These rating again point to the use of flywheel designs with fairly low power to energy ratios. For the 200 flywheel batteries for example, a more appropriate motor/generator is one that has a peak power of 250 kW and is optimized for continuous power and low rotor loss at 130 kW or less.

16.2.4 Economics of Energy Buffer for Wind Systems

From the above analysis more flywheel batteries are required for the energy buffer than for the hybrid wind system. This extra cost though is offset by the lack of a gas turbine. It is also clear that accurate wind forecasting is important to minimizing the number of flywheel batteries and improving the reliability of the energy buffer. Since the forecasting at most has to be three to four hours ahead, advance wind sensing equipment should make this quite possible.

To further decrease the number of flywheel batteries it is possible to shorten the constant power periods from an hour to 15 or 30 minutes. If this is taken one step further and the constant power is changed on a minute-by-minute basis, the flywheel batteries are basically providing frequency regulation. A wind system can therefore be coordinated with flywheel batteries and low cost generation, such as coal-fired generation, to provide a base level power that is reliable and low cost. The number of flywheel batteries required for this frequency regulation will depend on both the wind profiles and the rate at which the low cost generation can change output power. The energy buffer economics in this case will be the same as for frequency regulation, which is already shown in Section 16.1.2 to be substantially profitable.

Due to current leniency for wind generation, the energy buffer is a much better application for inertial storage such as flywheels. Such an energy buffer reduces emissions since gas turbines are not required to compensate for minute to hourly wind variations. When the energy buffer and wind generation are combined with low cost generation, they provide low cost and reliable base level generation. Most importantly, the energy buffer provides a means to significantly increase the percentage of power generated from wind.

17 Conclusion

This report has detailed the state of the art in wheel, enclosure, and magnetic bearings for flywheel batteries. A motor/generator design has also been developed that is capable of handling the low windage loss environment inside the flywheel battery's enclosure. In addition, the economics of flywheel batteries has been investigated for both wind and non-wind applications.

The synchronous reluctance machine is chosen as the motor/generator for a flywheel battery. This type of machine is chosen due to its relatively low rotor loss and its ability to operate continuously at high temperatures. The initial full-scale and small-scale machines were designed as axially laminated SYNREL machines.

The small-scale machine was fabricated and tested. The testing showed that using hot rolled carbon steel significantly decreases the performance of the machine. This reduction is due to the hot rolled steel's low permeability, low saturation point, and residual magnetic field. Switching to cold rolled carbon steel or silicon steel will alleviate these problems, but due to the thin gauge of these types of steel, the fabrication costs of the rotor are significantly increased.

More importantly, the rotor loss simulations show that even if cold rolled steel is used for the magnetic layers, the rotor loss is too high for a full-scale machine. Even modifying the number of layers or the layer materials is not able to significantly lower the rotor loss.

A design using a conventionally laminated four-pole rotor results in significantly reduced rotor loss. This motor/generator provides a suitable solution for the flywheel battery. Depending on the flywheel battery application, further improvements to this design are possible. To achieve this additional performance advanced structural analysis needs to be done. The SYNREL though does provide a high performance motor/generator for flywheel batteries.

Economic analysis shows that flywheel batteries are a profitable solution as an energy buffer or for providing frequency regulation for wind systems. Both of these solutions are not only profitable, but also allow for the possibility of increasing the percentage of wind utilized in a power system. The flywheel battery is also currently a possible solution for other utility applications such as frequency regulation (for load variations), spinning reserve, and peak power buffering. In the future a reduction in the cost of flywheel energy capacity will also enable the use of flywheel batteries to more effectively utilize transmission lines. Overall the flywheel battery appears to be a promising solution for numerous utility applications.

References

- [1] Herbst, J.D.; Manifold, S.M.; Murphy, B.T.; Price, J.H.; Thompson, R.C.; Walls, W.A.; Alexander, A.; Twigg, K., "Design, Fabrication, and Testing of 10MJ Composite Flywheel Energy Storage Rotors", 1998 SAE Aerospace Power Systems Conference, Paper #981282, April 1998
- [2] Thelen, R. F., "Advanced Locomotive Propulsion Systems (ALPS)", Technology Prospectus, Aug. 2002
- [3] Strubhar, J.L.; Thompson, R.C.; Pak, T.T.; Zierer, J.J.; Beno, J.H.; Hayes, R.J., "Lightweight Containment for High-Energy Rotating Machines", IEEE Transactions on Magnetics, Volume: 39 Issue: 1, Jan. 2003

- [4] Zhu, Z.Q. and Howe, D., "Halbach Permanent Magnet Machines and Applications a Review", Electric Power Applications, IEE Proceedings-, Volume: 148 Issue: 4, July 2001
- [5] Pichot, M.A.; Kajs, J.P.; Murphy, B.R.; Ouroua, A.; Rech, B.M.; Hayes, R.J.; Beno, J.H.; Buckner, G.D.; Palazzolo, A.B., "Active Magnetic Bearings for Energy Storage Systems for Combat Vehicles", Magnetics, IEEE Transactions on, Volume: 37 Issue: 1 Part: 1, Jan. 2001
- [6] Tsao, P.; Sanders, S.R.; Risk, G., "A Self-Sensing Homopolar Magnetic Bearing: Analysis and Experimental Results", IEEE Industry Applications Conference, 1999, Volume: 4, Oct. 1999
- [7] Antila, M.; Lantto, E.; Arkkio, A., "Determination of Forces and Linearized Parameters of Radial Active Magnetic Bearings by Finite Element Technique", IEEE Transactions On Magnetics, Volume: 34 Issue: 3, May 1998
- [8] Hofmann, H. and Sanders, S.R., "Synchronous Reluctance Motor/Alternator for Flywheel Energy Storage Systems", Power Electronics in Transportation 1996, IEEE, 1996
- [9] Mohan, N., "Electric Drives: An Integrative Approach", MNPERE, Minneapolis, MN, 2003
- [10] Boldea, I. and Nasar, S.A., "Electric Drives", CRC Press LLC, Boca Raton, US, 1999, chapter 10 and 11, pp. 253-325
- [11] Begalke, T., "Flywheel Battery with a Synchronous Reluctance Motor/Generator", M S Thesis, University of Minnesota-Twin Cities, Minneapolis, MN, 2004
- [12] Boldea, I., "Reluctance Synchronous Machines and Drives", OUP, Oxford, U.K., 1996
- [13] Epstien Test Data obtained from AK Steel
- [14] Ma L.; Sanada M.; Morimoto S.; Takeda Y., "Iron Loss Prediction Considering the Rotational Field and Flux Density Harmonics in IPMSM and SynRM", IEE Proceedings-Electric Power Applications, Volume: 150, Number. 6, Nov. 2003
- [15] Yadavalli, S.R., "Economics of Superconductive Energy Storage Inductor-Converter Units in Power Systems", PHD Thesis, University of Wisconsin-Madison, Madison, WI, 1975
- [16] Hingorani, N.G. and Gyugyi, L., "Understanding FACTS: Concepts and Technology of Flexible AC Transmission Systems", IEEE Press, Inc, New York, NY, 2000
- [17] Hofmann, H. and Sanders, S.R., "High-Speed Synchronous Reluctance Machine with Minimized Rotor Losses", Industry Applications, IEEE Transactions on, Volume: 36 Issue: 2, March-April 2000
- [18] Howe, D.; Mason, P.; Mellor, P.H.; Wu, Z.Y.; Atallah, K., "Flywheel Peak Power Buffer for Electric/Hybrid Vehicles", Electric Machines and Drives, 1999. International Conference IEMD '99, 1999

Appendix A

Agenda of 4 Workshops organized during 2003, 2004, 2005 and 2006

NSF-Sponsored Workshop “Teaching of Power Electronics and Electric Drives”

Wednesday July 9, 2003

6:00-9:00PM Pizza Party
3rd Floor Electrical Engineering/Computer Science

Thursday July 10, 2003

Breakfast *on your own*

- 8:30 – 12:00 Hands-on Tutorials on Using PSpice in Teaching of Power Electronics and Using Simulink in Modeling of Controlled Drives. These sessions will be recorded.
PLEASE BRING YOUR LAPTOP.
Mechanical Engineering 108 & 212
- 12:00 - 1:30 Lunch - *Radisson Hotel Metrodome*
- 1:30 – 1:40 Welcome – Professor Mostafa Kaveh, Head of ECE, University of Minnesota
Electrical Engineering 3-180
- 1:40 – 2:30 NSF CCLI Program for Lab Development - Dr. Roger Salters
Electrical Engineering 3-180
- 2:30 – 3:30 Panel discussion to identify needs, challenges and solutions
Electrical Engineering 3-180
- 3:30 – 5:30 Poster Session Presented by Attendees (Papers for Poster Presentations will be included in the workshop proceedings)
3rd Floor Electrical Engineering

6:30 – 7:30PM Reception - *A.I. Johnson Room, McNamara Alumni Center*

Friday July 11, 2003

Breakfast *on your own*

- 8:30 – 5:00 First Course on Power Electronics
 - Integrating Lectures with Simulations and Hardware Laboratory
 - Discussion of Curriculum Structure*8:30-12:00 Electrical Engineering 3-180*
12:00-1:30 Lunch *on your own*
- 1:30-5:00 Discussion Continued
Electrical Engineering 3-210

6:00 – 8:30PM Reception and Banquet - *Campus Club, Coffman Union*

Saturday July 12, 2003

Breakfast *on your own*

- 8:30 – 12:00 First Course on Electric Drives
• Integrating Lectures with Simulations and Hardware Laboratory
• Discussion of Curriculum Structure
Electrical Engineering 3-210
- 12:00-1:30 Lunch *on your own*
- 1:30-5:00 Discussion Continued
Electrical Engineering 3-210
- 6:00–9:30PM MOA (Mall of America)
The bus will pick up outside the Radisson Hotel Metrodome at 6 p.m sharp. The bus will depart MOA at 9:30 p.m. sharp and return to the Radisson by 10 p.m.

Sunday July 13, 2003

Breakfast *on your own*

- 8:30 – 12:00 Hands-on Usage of Hardware Laboratories
Electrical Engineering 2-270

Tutorials

- All participants are encouraged to bring their Laptop PCs. PSpice (Evaluation version) and Simulink (full version with limited-time license) will be loaded on participants' PCs.

Remember to periodically check the workshop website for further updates: at
<http://www.ece.umn.edu/groups/workshop2003/>. If you have any questions or need further assistance, please contact me.

Brooke Reseland, Program Coordinator
Continuing Professional Education
University of Minnesota
352 Classroom Office Building
1994 Buford Avenue
St. Paul, MN 55108 USA
Telephone: 612-625-4265
Fax: 612-624-6225
E-mail: breselan@cce.umn.edu

Wind Workshop 2004

(Utility Integration of Wind Power)

University of Minnesota
September 30 - October 1, 2004

Sponsored by:

XcelEnergy

National Science Foundation

Department of Electrical Engineering and the Center for Electric Energy, University of Minnesota

Objective: To bring together the developers, vendors, researchers and interested parties with the objective of discussing progress and technical challenges in harnessing wind energy at a large scale. The theme of this year's workshop is utility integration of wind power.

Who Should Attend: This workshop is open to anyone interested in technical issues related to wind energy, including power utilities, developers, educators, researchers, and vendors.

Optional Tutorial: Principles of Electric Drives for Harnessing Wind Energy

4:00-6:30 p.m., Wednesday Sept 29, 2004 (Room 2-122 Molecular and Cellular Biology)

Based on NSF-sponsored developments at the University of Minnesota, in this tutorial we will examine in simple terms the basic concepts of electro-mechanical energy conversion, and then discuss how ac machines operating at variable speed can be used as generators to feed power into the utility grid through power electronics. Prerequisite: Basic electrical engineering background. Reference textbook: Electrical Drives: An Integrative Approach, by Ned Mohan (see www.mnpere.com for details). **Instructor:** Prof. Ned Mohan, University of Minnesota

Program:

Thursday Sept 30, 2004

8:30-10:00	Opening Session - Welcoming Remarks – Michelle Swanson (XcelEnergy) - Agenda – Ned Mohan (University of Minnesota) - Potential and Challenges – John Dunlop (American Wind Energy Association) - National Renewable Energy Lab's Perspective–Brian Parsons (NREL))
10:30-12:00	Large-Scale Integration of Wind into Utility Systems and Stability Studies - Robert Zavadil (EnerNex) - System Developers' Perspective – Paul White (Project Resources Corp) - Terje Gjengedal – Grid Codes in Europe (VP – Statkraft, Norway) - Perspectives from Denmark: Prof. Frede Blaabjerg (U of Aalborg, Denmark)
1:15-2:00	Harnessing of Wind Energy from Manufacturers' Perspective - GE Wind – Mark Eilers - Vestas America– Jesper Michaelsen
2:00-2:45	Wind Forecasting and State Efforts - Mark Ahlstrom (WindLogics) - Jeff Haase (MN Dept of Commerce)
3:15- 5:30	Brainstorming Session: Possibilities and Challenges Panelists: Beth Soholt - Chair (Wind on the Wires), Mark McGree (Xcel), Tim Rogelstad (Otter Tail Power), Bill Grant (Izaak Walton League), David Duebner (MISO), Mark Rathbun (GRE), Frank Greb (Alliant Energy WindConnect)

Friday Oct 1, 2004

8:30-9:30	Wind-Related Research at the University of Minnesota <ul style="list-style-type: none">- Minimizing Torque Pulsation under Utility Unbalance and Providing Voltage Support- Inertial Energy Storage Research to make Wind Power Dispatchable
10:00-12:00	Poster Session <ul style="list-style-type: none">- Invited Papers on Relevant Developments, Specifications, Standards, and Research. This session will be very informative, providing a chance for in-depth interaction with the presenters.

Deadline: None, but please register as soon as possible for our planning purposes.

Poster Exhibits:

We invite individuals and companies to exhibit poster materials relevant to this audience. The posters will be on display on Friday, October 1 from 10:00 a.m. to noon. If you have questions about posters or would like to exhibit, contact Ned Mohan, 612-625-3362, mohan@ece.umn.edu.

CEUs:

Participants attending the tutorial will receive 0.25 CEUs. Participants attending the workshop will receive 0.9 CEUs. One CEU (1.0) is defined as 10 contact hours of participation in an organized continuing education experience under responsible sponsorship, capable direction and qualified instruction.

Location & Accommodations:

Both the tutorial and workshop will be held on the Minneapolis campus of the University of Minnesota.

The optional tutorial, September 29, 2004 will be held in room 2-122 Molecular Cellular Biology.

The workshop, September 30 – October 1 will be held in the Coffman Memorial Union Theater and Great Hall. Coffman Memorial Union is located at 300 Washington Avenue SE on the Minneapolis Campus of the University of Minnesota.

Hotel accommodations are available by contacting one of the hotels listed below. Mention you are attending a University of Minnesota workshop to receive their University rate.

Radisson Hotel Metrodome: 612-379-8888

615 Washington Avenue SE, Minneapolis

Approximate one block from campus

Days Inn: 612-623-3999

2407 University Avenue SE, Minneapolis

Approximately 3 blocks from campus

Econo Lodge: 612-331-6000

2500 University Avenue SE, Minneapolis

Approximately 4 blocks from campus

Contact:

For registration questions, contact: Kay Syme, 612-624-4938, conferences4@cce.umn.edu

For technical questions, contact: Ned Mohan, 612-625-3362, mohan@ece.umn.edu

Sponsored by Xcel Energy, National Science Foundation and University of Minnesota Department of Electrical and Computer Engineering and the Center for Electric Energy, and IEEE Twin Cities Power Engineering Society (PES)

Workshop on Renewable Energy for Minnesota

McNamara Alumni Center, University of Minnesota, Minneapolis

Friday December 9, 2005

Objectives:

- Discuss renewable energy prospects in Minnesota
- Bring renewable energy curriculum into K-12
- Describe the research being conducted in this field in the Department of Electrical and Computer Engineering (funded by Xcel Energy and the National Science Foundation) and also at the University of Minnesota.

Who should Attend: Everyone concerned with energy, particularly the technical issues, and its impact on the environment and society.

Tentative Schedule:

7:30-8:00	Registration, Coffee and Rolls
8:00-8:30	Welcome and Introduction <ul style="list-style-type: none">• Workshop Objectives and Agenda: <i>Prof. Ned Mohan</i>, ElectE, U of M• Welcoming Remarks: <i>Prof. Steven Crouch</i>, Dean – Institute of Technology, U of M• Renewable Energy Development Fund: <i>Michelle Swanson</i>, Xcel Energy
8:30-10:20	Renewable Energy Overview <ul style="list-style-type: none">• National Perspective: <i>Susan Hock</i>, Director National Renewable Energy Lab (NREL) Center for Electric & Hydrogen Technologies & Systems, Golden, Colorado• Lessons From Norway: <i>Dr. Terje Gjengedal</i>, VP- STATKRAFT, in-charge of renewable energy projects• What is Happening in Minnesota?: <i>Michael Bull</i>, Assistant Commissioner, Minnesota Department of Commerce
10:20-10:50	Coffee Break
10:50-11:50	Wind Energy <ul style="list-style-type: none">• Present Projects and Potential in Minnesota: <i>John Dunlop</i>, American Wind Energy Association• Transmission Planning in Minnesota – CapX 2020: <i>Gordon Pietsch</i>, Great River Energy
11:50-1:00	Lunch (buffet lunch provided)
1:00-2:30	Hydrogen and Wind <ul style="list-style-type: none">• “The Potential and Challenge of a Hydrogen-Electric Economy”: <i>Rolf Nordstrom</i>, Director - Upper Midwest Hydrogen Initiative, Great Plains Institute• Hydrogen From Wind: <i>Prof. Lanny Schmidt</i>, Regents Professor, ChemE, U of M• Research in Fuel Cells: <i>Brad Palmer</i>, Cummins Power Generation, Fridley, Minnesota
2:30-2:45	Break
2:45 - 3:45	Biomass <ul style="list-style-type: none">• Present Status and Potential Resources: <i>Prof. Robert Elde</i>, Dean-College of Biological Sci, UMN• Bio-Diesel Engines: <i>Prof. David Kittelson</i>, MechE, U of M
3:45-4:45	Bringing Renewable Energy Curriculum into K-12 Courses <ul style="list-style-type: none">• California Experience: <i>Karen Farrell</i>, Irvine, CA• Group Discussion led by: <i>Steven Pullar</i>, Woodbury Math and Science Academy, MN and <i>Michael Maas</i>, Eden Prairie High School, MN
4:45-5:00	Suggestions for Next Year's Workshop and Adjournment

Posters on Display: Research being conducted in this field in the Department of Electrical and Computer Engineering, funded by Xcel Energy and the National Science Foundation.

Registration Fee: \$45**University of Minnesota Faculty: No Fee (Registration includes free Lunch, No parking)****Student Fee: No Fee (Registration includes free Box Lunch, No parking)**

The registration fee of \$45 includes sessions, materials, lunch, breaks and parking. Park in the University Avenue Ramp (adjacent to the McNamara Alumni Center) and bring your ticket to the registration desk for validation. Students and the University of Minnesota faculty may attend the workshop for free but must provide for their own parking. No refunds are available. You may register by mail, fax, or online using the enclosed registration form. If you are a University of Minnesota faculty member, please indicate so in the box for the Registration Fee.

Location

The McNamara Alumni Center is located at 200 Oak Street SE in Minneapolis, Minnesota (on the Minneapolis campus of the University of Minnesota). For directions visit, www.alumnicenter.umn.edu. Convenient lodging is available at the Radisson University Hotel. Call 612-379-8888 for rates and to make a reservation.

Continuing Education Units (CEUs)

Attendees will earn 7 hours of Continuing Education Units through the College of Continuing Education at the University of Minnesota.

Contact

For registration questions, contact Katie Kjeseth, 612-624-3708, or conferences5@cce.umn.edu

For technical questions, contact Ned Mohan, 612-625-3362, mohan@ece.umn.edu

Web Site: www.ece.umn.edu/groups/wind

URL for online registration: http://register.cce.umn.edu/Course.pl?sect_key=178522

Sponsored by:

XcelEnergy
National Science Foundation
University of Minnesota Department of Electrical and Computer Engineering
University of Minnesota Center for Electric Energy
IEEE Twin Cities Power Engineering Society (PES)

Workshop on Renewable Energy for Minnesota

McNamara Alumni Center, University of Minnesota, Minneapolis

Thursday October 12, 2006

Objectives:

- Discuss renewable energy prospects in Minnesota
- Bring renewable energy curriculum into K-12
- Describe the research being conducted in this field in the Department of Electrical and Computer Engineering (funded by XcelEnergy, National Science Foundation and ONR)

Who should Attend: Everyone concerned with energy, particularly the technical issues, and its impact on the environment and society.

Agenda:

7:30-8:00	Registration, Coffee and Rolls
8:00-8:30	Welcome and Introduction <ul style="list-style-type: none">• Welcoming Remarks: Steven Crouch, Dean – Institute of Technology, U of M• Workshop Objectives and Agenda: Ned Mohan, ElectE, U of M• Renewable Energy Development Fund: Michelle Swanson, XcelEnergy
8:30-10:00	Renewable Energy Overview <ul style="list-style-type: none">• A Power Grid for the Hydrogen Economy: Thomas Overbye, Professor, University of Illinois• Lessons From Norway: Terje Gjengedal, Vice President - STATKRAFT, NORWAY, in charge of renewable energy projects• Planning for Renewable Energy at a Minnesota Utility?: Glen Skarbakka, Manager of Resource Planning, Great River Energy
10:00-10:30	Coffee Break
10:30-11:30	Wind Energy <ul style="list-style-type: none">• Present Projects and Potential in Minnesota: John Dunlop, American Wind Energy Association• Transmission Planning in Minnesota – CapX 2020 – Group I project implementation & future planning: Terry Grove, GRE
11:30-12:00	Research in Renewable Energy at the ECE Dept, University of Minnesota <ul style="list-style-type: none">• Results of Research funded by NSF, XcelEnergy and ONR: Ned Mohan, ElectE, UofM
12:00-1:00	Lunch (buffet lunch provided)
1:00-2:00	Hydrogen and Fuel Cells: Making the Connection <ul style="list-style-type: none">• Hydrogen From Wind: Lanny Schmidt, Regents Professor, ChemE, U of M• Research in Fuel Cells: Brad Palmer, Cummins Power Generation, Fridley, Minnesota
2:00-3:00	Bringing Renewable Energy and Conservation Curriculum into K-12 Courses <ul style="list-style-type: none">• Sustainable Architecture: Virajita Singh and John Carmody, U of M• Group Discussion led by: Steven Pullar, Woodbury Math and Science Academy, MN and Michael Maas, Eden Prairie High School, MN

Posters on Display: Research being conducted in this field in the Department of Electrical and Computer Engineering, funded by XcelEnergy, National Science Foundation and ONR.

Registration and Fees

Full Registration Fee: **\$45**

Faculty/Educator/Student Fee: **\$10 (parking not included)**

The registration fee includes sessions, materials, lunch, breaks and parking. Park in the University Avenue Ramp (adjacent to the McNamara Alumni Center) and bring your ticket to the registration desk for validation. Educators, Faculty and Students must provide for their own parking. No refunds are available. You may register by mail or fax using the PDF of the registration form (can also be downloaded from www.ece.umn.edu/groups/wind), or by "Online Registration":

http://register.cce.umn.edu/Course.pl?sect_key=179531

Location

The McNamara Alumni Center is located at 200 Oak Street SE in Minneapolis, Minnesota (on the Minneapolis campus of the University of Minnesota). For directions, visit www.alumnicenter.umn.edu. Convenient lodging is available at the Radisson University Hotel. Call 612-379-8888 for rates and to make a reservation.

Continuing Education Units (CEUs)

Attendees will earn 5.5 hours of Continuing Education through the College of Continuing Education at the University of Minnesota.

Contact

For registration questions, contact Electra Sylva, 612-624-3708, or conferences5@cce.umn.edu

For technical questions, contact Ned Mohan, 612-625-3362, mohan@umn.edu

Web Site: www.ece.umn.edu/groups/wind

Group Photo: Renewable Energy Workshop 2005 in McNamara Center (www.alumnicenter.umn.edu)



About The University of Minnesota – Minneapolis Campus:

Arguably the most vibrant and beautiful campus that spans both sides of the Mississippi as it begins its 2,000 mile journey towards the Gulf of Mexico, it is also the second largest with the Fall 2005 enrollment of 51,175 (only ASU-Tempe was larger with 51,712). How many universities can boast 665 registered student organizations?



*Attribution ShareAlike License v. 2.5
Photo taken by [Bobak Ha'Eri](#). Oct. 21, 2003.*

Appendix B

A Highly Simplified Control of Matrix Converters

(Description of this is taken from the following Reference: First Book on Power Electronics by Ned Mohan, year 2005 edition, ISBN 0-9715292-4-8)

12-9 MATRIX CONVERTERS (DIRECT LINK SYSTEM) [7]

To review once again, power electronics systems are categorized as Voltage-Link systems described so far where a capacitor is used in parallel with two converters as an energy storage element, and Current-Link systems described in Chapters 14 and 15 in very high power applications where an inductor is used in series with the two converters for energy storage. There is another structure called the matrix converters which provide a direct link between the input and the output, without any intermediate energy-storage element. There is a great deal of research interest at present in these converters because they avoid the intermediate energy storage element.

Such a system for a three-phase to three-phase conversion is shown in Fig. 12-31a, where there is a bi-directional switch from each input port to each output port. Such a bi-directional switch must be capable of blocking voltages of either polarity, and conduct current in either direction. Such a bi-directional switch can be realized, for example, by two IGBTs and two diodes, as connected in Fig. 12-31b. When the two transistors are gated on, the current can flow in either direction, effectively representing the closed position of the bi-directional switch. When both the transistors are gated off, current can not flow in either direction, effectively representing the closed position of the bi-directional switch.

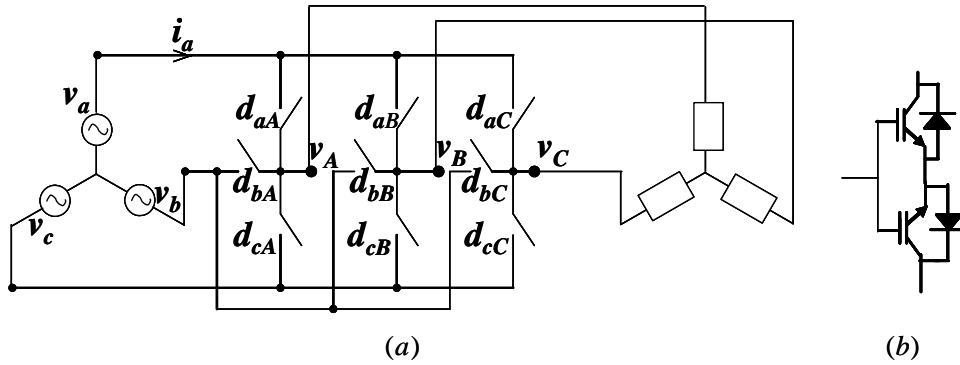


Figure 12-31 Matrix Converter.

For explanation purposes, we will assume the left-side in Fig. 12-31a to be a utility system and the right-side to be supplying a load, for example an ac machine. The utility-side (a, b, c) is made to behave like a voltage-port by connecting a three-phase capacitor bank across it. The load-side, due to the series inductance inherent in any load, behaves as a current-port. The matrix converter in Fig. 12-31a is purposely drawn to look like a three-level converter, where the voltage at the output port A, for example, is synthesized by time-weighted averaging within a switching cycle of the input voltage of a, b and c. In the discussion to follow, for the ease of writing, we will *not* use bars on top of the switching-cycle averaged variables however they are understood to be such.

Therefore the output port voltages, with respect to the input neutral, can be written as the sum of the sum of the input voltage multiplied by their respective duty-ratios shown in Fig. 12-31a:

$$\begin{bmatrix} v_A \\ v_B \\ v_C \end{bmatrix} = \begin{bmatrix} d_{aA} & d_{bA} & d_{cA} \\ d_{aB} & d_{bB} & d_{cB} \\ d_{aC} & d_{bC} & d_{cC} \end{bmatrix} \begin{bmatrix} v_a \\ v_b \\ v_c \end{bmatrix} \quad (12-57)$$

Similarly, the currents drawn from the input port depend on the sum of the three load current multiplied by their respective duty-ratios:

$$\begin{bmatrix} i_a \\ i_b \\ i_c \end{bmatrix} = \begin{bmatrix} d_{aA} & d_{aB} & d_{aC} \\ d_{bA} & d_{bB} & d_{bC} \\ d_{cA} & d_{cB} & d_{cC} \end{bmatrix} \begin{bmatrix} i_A \\ i_B \\ i_C \end{bmatrix} \quad (12-58)$$

The voltage and current relationships between the input and the output ports can be simultaneously represented on the switching-cycle averaged basis by ideal transformers as shown in Fig. 12-32. In Fig. 12-32, each output voltage is series connection of three secondary-winding voltages, consistent with Eq. 12-57. Similarly in Fig. 12-32, the current at each input port is the parallel combination of the three currents flowing into the primary windings, consistent with Eq. 12-58.

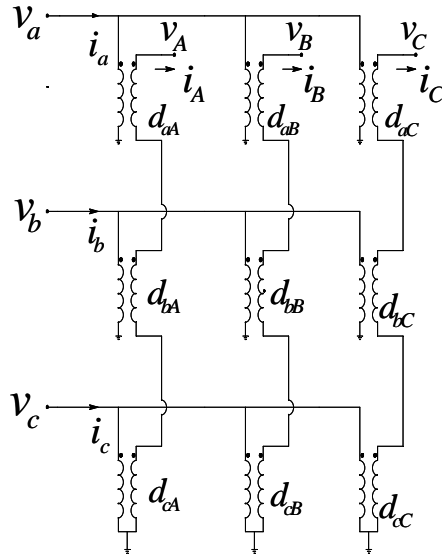


Figure 12-32 Matrix Converter switching-cycled averaged representation.

With respect to the input neural, the input voltages are given as

$$v_a = \hat{V}_i \cos(\omega_i t) \quad v_b = \hat{V}_i \cos(\omega_i t - \frac{2\pi}{3}) \quad v_c = \hat{V}_i \cos(\omega_i t - \frac{4\pi}{3}) \quad (12-59)$$

12-9-1 Elimination of the Input Frequency from the Output

Since the output frequency is completely independent of the input frequency (it can be higher or lower than the input frequency), the first order of business is to eliminate the input frequency from the conversion. This can be illustrated for phase-A, for example, where the corresponding

duty-ratios in Eq. 12-57 are made to vary co-sinusoidally at the same frequency as the input frequency

$$d_{aA} = k_A \cos(\omega_i t) \quad d_{bA} = k_A \cos(\omega_i t - \frac{2\pi}{3}) \quad d_{cA} = k_A \cos(\omega_i t - \frac{4\pi}{3}) \quad (12-60)$$

The duty-ratios in Eq. 12-60 are in phase with their respective input voltages to yield a unity power factor of operation at the input. It is possible to introduce a phase-shift in the duty-ratios given in Eq. 12-60 to obtain the input power factor to be lagging or leading.

Using the duty-ratios of Eq. 12-60 for phase-A in Eq. 12-57,

$$v_A = d_{aA}v_a + d_{bA}v_b + d_{cA}v_c = \frac{3}{2}\hat{V}_i k_A \quad (12-61)$$

where the amplitudes, k_A , of the duty-ratios contains the amplitude and the frequency information of the output to be synthesized, where for the three output phases

$$k_A = k \cos \omega_o t \quad k_B = k \cos(\omega_o t - \frac{2\pi}{3}) \quad k_C = k \cos(\omega_o t - \frac{4\pi}{3}) \quad (12-62a)$$

and from the above two equations, for a given input voltage \hat{V}_i and the desired output voltage \hat{V}_o

$$k = \left(\frac{2}{3\hat{V}_i} \right) \hat{V}_o \quad (12-62b)$$

12-9-2 Introducing Common-Mode Offsets

The duty ratios, as defined by Eq. 12-60, being co-sinusoidal functions of time, become negative.

For example, $d_{aA} = \underbrace{(k \cos \omega_o t)}_{k_A} \cos(\omega_i t)$.

A negative duty-ratio cannot be realized physically. In fact each duty-ratio must be constrained between 0 and 1:

$$0 \leq d \leq 1 \quad (12-63)$$

To meet these limits, we will introduce offsets which are common in each output phase, and therefore get cancelled in the output. With these common-mode offsets, the duty ratios of switches get modified as shown in Fig. 12-33, where the absolute value of each duty-ratio is added to the respective duty-ratios in Eq. 12-60, for example,

$$d_{aA} \rightarrow d_{aA} + |d_{aA}| \quad (12-64)$$

It is clear that the combined duty-ratios modified in Eq. 12-64 cannot become negative and hence the lower limit of 0 in Eq. 12-63 is satisfied. In order to meet the upper limit of 1 on the duty-ratio in Eq. 12-64, the maximum amplitude of k_A etc is limited to 0.5:

$$k(\max) = 0.5 \quad (12-65)$$

and therefore, in the output phase-A

$$\begin{aligned}
 d_{aA} &\rightarrow d_{aA} + \underbrace{|0.5 \cos \omega_i t|}_{D_a} \\
 d_{bA} &\rightarrow d_{bA} + \underbrace{|0.5 \cos(\omega_i t - 2\pi/3)|}_{D_b} \\
 d_{cA} &\rightarrow d_{cA} + \underbrace{|0.5 \cos(\omega_i t - 4\pi/3)|}_{D_c}
 \end{aligned} \tag{12-65}$$

where d_{aA} etc are as given by Eq. 12-60.

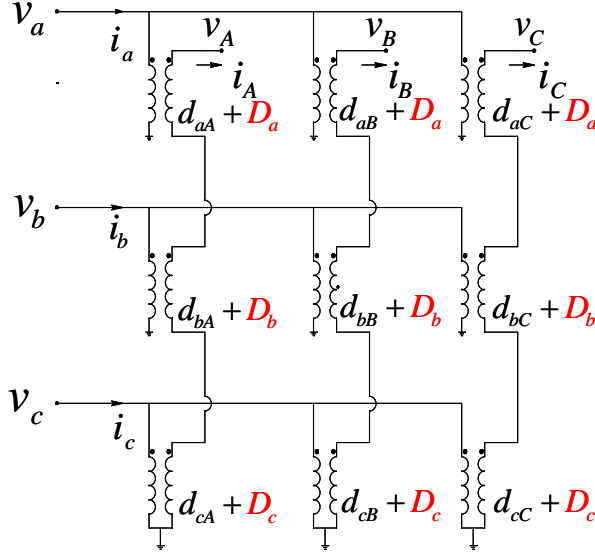


Figure 12-33 Common-mode offsets to ensure the realizable range of duty-ratios.

Next, we will make use of the property in synthesizing three-phase outputs, as in SV-PWM discussed earlier to raise the limit on k from 0.5 to a higher value. The three duty-ratios associated with the input phase-a in Fig. 12-33 are

$$\begin{aligned}
 d_{aA} &\rightarrow \underbrace{k_A \cos \omega_i t}_{d_{aA}} + \underbrace{|0.5 \cos \omega_i t|}_{D_a} \\
 d_{aB} &\rightarrow \underbrace{k_B \cos \omega_i t}_{d_{aB}} + \underbrace{|0.5 \cos \omega_i t|}_{D_a} \\
 d_{aC} &\rightarrow \underbrace{k_C \cos \omega_i t}_{d_{aC}} + \underbrace{|0.5 \cos \omega_i t|}_{D_a}
 \end{aligned} \tag{12-66}$$

In the worst-case when D_a is at its peak and equals 0.5, as discussed in SV-PWM, a higher value of the output voltage can be obtained if

$$\begin{aligned}
d_{aA} &\rightarrow \left(k_A - \frac{\max(k_A, k_B, k_C) + \min(k_A, k_B, k_C)}{2} \right) \cos \omega_i t + \underbrace{|0.5 \cos \omega_i t|}_{D_a} \\
d_{aB} &\rightarrow \left(k_B - \frac{\max(k_A, k_B, k_C) + \min(k_A, k_B, k_C)}{2} \right) \cos \omega_i t + \underbrace{|0.5 \cos \omega_i t|}_{D_a} \\
d_{aC} &\rightarrow \left(k_C - \frac{\max(k_A, k_B, k_C) + \min(k_A, k_B, k_C)}{2} \right) \cos \omega_i t + \underbrace{|0.5 \cos \omega_i t|}_{D_a}
\end{aligned} \quad (12-67)$$

An identical change in duty-ratios associated with input phases b and c is made in Fig. 12-33. Using Eq. 12-67 for duty-ratios, the maximum value of k in Eq. 12-62, similar to that in SV-PWM, is as follows

$$k(\max) = 0.5 \times \frac{2}{\sqrt{3}} \approx 0.57 \quad (12-68)$$

Using this maximum value of k from Eq. 12-68 into Eq. 12-61, the maximum output voltage amplitude is related to the input voltage amplitude as

$$\hat{V}_o(\max) = \frac{3}{2} \left(0.5 \times \frac{2}{\sqrt{3}} \right) \hat{V}_i = \frac{\sqrt{3}}{2} \hat{V}_i \approx 0.867 \hat{V}_i \quad (12-69)$$

which points to one of the drawbacks of the matrix converters, that is, the maximum output magnitude is limited to 0.867 times the input voltage magnitude.

Next, to make this converter realizable, note that each output current in Fig. 12-33, for example i_A , must always have a path to flow, that is the sum of the duty-ratios associated with i_A must sum to 1 at all instants. The sum of these duty-ratios is

$$(d_{aA} + D_a) + (d_{bA} + D_b) + (d_{cA} + D_c) = \underbrace{(d_{aA} + d_{bA} + d_{cA})}_{=0} + (D_a + D_b + D_c) \quad (12-70)$$

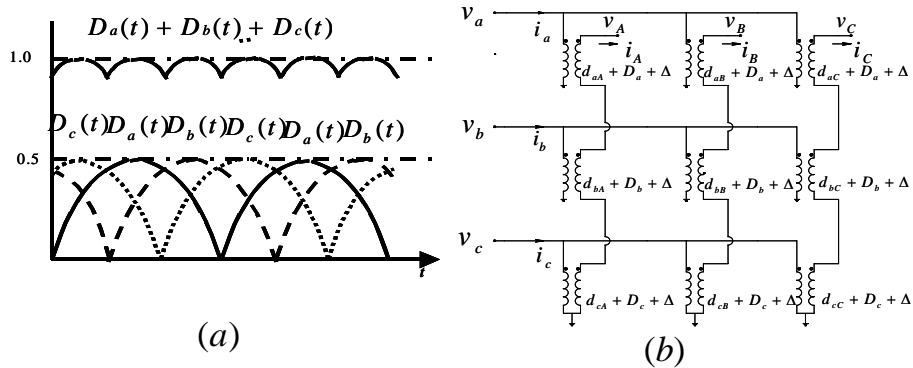


Figure 12-34 Modification of common-mode offsets to provide current path.

In Eq. 12-70, the offsets do not sum to 1 at all times, as illustrated in Fig. 12-34a, and therefore the difference between 1 and the sum of all three duty ratios is divided equally in three parts and Δ is added to each duty-ratio, as shown in Fig. 12-34b, where

$$\Delta = \frac{1 - (D_a + D_b + D_c)}{3} \quad (12-71)$$

12-9-3 Generation of Switching Signals

Once we will focusing on phase-A, since similar can be done for the other two output phases. The duty-ratios numerically equal the control voltages if we assume the switching-frequency triangular carrier signal in Fig. 12-35 to be unity. In such a case, comparing d_{aA} , $(d_{aA} + d_{bA})$, and $(d_{aA} + d_{bA} + d_{cA})$ generates the switching functions q_{aA} , q_{bA} , and q_{cA} as shown in Fig. 12-36.

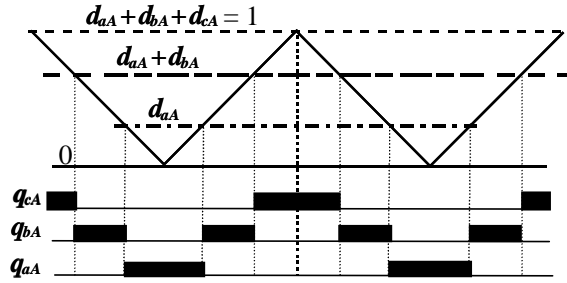


Figure 12-35 Generation of switching signals.

12-9-4 Calculating the Input Currents

Next we will calculate the input currents such as i_a , given that the output currents are lagging behind the output voltages by an angle ϕ as follows:

$$i_A = \hat{I}_0 \cos(\omega_o t - \phi_0) \quad i_B = \hat{I}_0 \cos(\omega_o t - \frac{2\pi}{3} - \phi_0) \quad i_C = \hat{I}_0 \cos(\omega_o t - \frac{4\pi}{3} - \phi_0) \quad (12-72)$$

From Fig. 12-35, since, by Kirchhoff's current law $i_A + i_B + i_C = 0$,

$$i_a = d_{aA}i_A + d_{aB}i_B + d_{aC}i_C \quad (12-73)$$

where d_{aA} , d_{aB} , and d_{aC} are given the quantities in brackets in Eq. 12-67

$$d_{aA} = \left(k_A - \frac{\max(k_A, k_B, k_C) + \min(k_A, k_B, k_C)}{2} \right) \cos \omega_i t$$

$$d_{aB} = \left(k_B - \frac{\max(k_A, k_B, k_C) + \min(k_A, k_B, k_C)}{2} \right) \cos \omega_i t \quad (12-74)$$

$$d_{aC} = \left(k_C - \frac{\max(k_A, k_B, k_C) + \min(k_A, k_B, k_C)}{2} \right) \cos \omega_i t$$

where,

$$k_A = k \cos \omega_o t \quad k_B = k \cos(\omega_o t - \frac{2\pi}{3}) \quad k_C = k \cos(\omega_o t - \frac{2\pi}{4}) \quad (12-75)$$

Substituting Eqs. 12-74 and 12-75 into Eq. 12-73 and making use of $i_A + i_B + i_C = 0$,

$$i_a = \hat{I}_i \cos \omega_i t \quad (12-77)$$

where,

$$\hat{I}_i = \left(\frac{3}{2} k \right) \hat{I}_o \cos \phi_o \quad (12-78)$$

12-9-5 Input Power Factors other than Unity

The analysis above is shown for the input power factor of unity. For any other power factor, a similar analysis can be carried out. It shows another drawback of Matrix converters, that is the output voltage available goes down as the input power factor.